ULTRASHORT LASER PULSE SHAPING FOR NOVEL LIGHT FIELDS AND EXPERIMENTAL BIOPHYSICS

Andrew Peter Rudhall

A Thesis Submitted for the Degree of PhD
at the
University of St Andrews

2013

Abstract

Broadband spectral content is required to support ultrashort pulses. However this broadband content is subject to dispersion and hence the pulse duration of corresponding ultrashort pulses may be stretched accordingly. I used a commercially-available adaptive ultrashort pulse shaper featuring multiphoton intrapulse interference phase scan technology to characterise and compensate for the dispersion of the optical system *in situ* and conducted experimental and theoretical studies in various inter-linked topics relating to the light-matter interaction.

Firstly, I examined the role of broadband ultrashort pulses in novel light-matter interacting systems involving optically co-trapped particle systems in which inter-particle light scattering occurs between optically-bound particles. Secondly, I delivered dispersion-compensated broadband ultrashort pulses in a dispersive microscope system to investigate the role of pulse duration in a biological light-matter interaction involving laser-induced cell membrane permeabilisation through linear and nonlinear optical absorption. Finally, I examined some of the propagation characteristics of broadband ultrashort pulse propagation using a computer-controlled spatial light modulator. The propagation characteristics of ultrashort pulses is of paramount importance for defining the light-matter interaction in systems. The ability to control ultrashort pulse propagation by using adaptive dispersion compensation enables chirp-free ultrashort pulses to be used in experiments requiring the shortest possible pulses for a specified spectral bandwidth. Ultrashort pulsed beams may be configured to provide high peak intensities over long propagation lengths, for example, using novel beam shapes such as Bessel-type beams, which has applications in biological light-matter interactions including phototransfection based on laser-induced cell membrane permeabilisation. The need for precise positioning of the beam focus on the cell membrane becomes less strenuous by virtue of the spatial properties of the Bessel beam. Dispersion compensation can be used to control the temporal properties of ultrashort pulses thus permitting, for example, a high peak intensity to be maintained along the length of a Bessel beam, thereby reducing the pulse energy required to permeabilise the cell membrane and potentially reduce damage therein.

Contents

List of publications

Here, the publications obtained throughout the course of the PhD work are listed:

Peer-reviewed publications

(i) 'Exploring the ultrashort pulse laser parameter space for membrane permeabilisation in mammalian cells', Andrew P. Rudhall, Maciej Antkowiak, Xanthi Tsampoula, Michael Mazilu, Nikolaus K. Metzger, Frank Gunn-Moore and Kishan Dholakia, Nat. Sci. Rep., **2**, 858, 2012.
(ii) 'An interacting dipole model to explore broadband transverse optical binding', M. Mazilu, A. Rudhall, E. M. Wright, and K. Dholakia, J. Phys.: Condens. Matter, **24**, 464117, 2012.

Conference publications

(iii) 'Revisiting transverse optical binding,' Jörg Baumgartl, Andrew P. Rudhall, Michael Mazilu, Ewan Wright and Kishan Dholakia, Proc. SPIE, **7400**, 2009.
(iv) 'The role of spectral bandwidth in transverse optical binding', Michael Mazilu, Andrew P. Rudhall, Ewan Wright and Kishan Dholakia, Proc. SPIE, **8458**, 2012.

Posters

(v) 'Measuring the transversal optical binding interaction between dielectric Particles', A.P. Rudhall, J. Baumgartl, M. Mazilu, E.M. Wright and K. Dholakia, COST meeting, Aberfoyle, 2009.
(vi) 'Ultrashort pulse dispersion compensation for transfection by photoporation using multiphoton intrapulse interference phase scan', A.P. Rudhall, X. Tsampoula and K. Dholakia, Biophotonics Summer School, Ven, Sweden, 2009.
(vii) 'The role of pulse duration in the laser-induced membrane permeabilization of mammalian cells', Andrew P. Rudhall, Maciej Antkowiak, Xanthi Tsampoula, Michael Mazilu, Nikolaus K. Metzger, Frank Gunn-Moore and Kishan Dholakia, SUPA/SU2P meeting, University of St Andrews, 2011.

Chapter 1

Introduction

In this thesis dispersion measurement and compensation of broadband ultrashort pulses is investigated. Ultrashort pulses have found a vast array of applications in the natural sciences. From a historical perspective, the term *ultrashort pulse* generally referred to pulse durations in the range from picosecond to around a hundred femtoseconds. Technological progress yielded shorter duration pulses which were more greatly affected by chromatic dispersion than typical 100 fs ultrashort pulses and were hence termed broadband ultrashort pulses. These broadband ultrashort pulses are subject to more severe dispersion and change their duration after passing through dispersive optical elements such as lenses, chirped mirrors, Gires-Tournois interferometers [1] and the like. However, provided the bandwidth is sufficiently narrow the pulse duration will not significantly increase. Broadband ultrashort pulses are generally associated with ultrashort pulses which become significantly stretched in dispersive optical systems. Depending upon the optical system, a broadband ultrashort pulse may experience significant dispersion which has the potential to increase its overall pulse duration, potentially by many orders of magnitude. For this reason broadband ultrashort pulses have not been routinely used in practical settings, for example, in biophotonics. However, this situation is rapidly changing with commercially viable systems. With the advent of flexible commercial compensation systems such as those utilising multiphoton intrapulse interference phase scan (MIIPS), which fully compensate for dispersion and associated pulse broadening, there has been increasing interest in using broadband ultrashort pulses across a wider research base, and in particular, biophotonics.

Along with some theoretical work, this thesis reports our experimental results conducted using the MIIPS commercial pulse shaper by Biophotonic Solutions, Inc. The thesis is organised as follows.

(i) The introduction begins with a discussion of ultrashort pulses, their properties and generation. This chapter is designed to point out the advantages and disadvantages of broadband ultrashort pulses along with concepts essential for introducing the pulse shaping chapter.

(ii) The pulse shaping chapter examines the role of dispersion and discusses in detail the experimental arrangement and method used to compensate for dispersion, which is relevant for subsequent chapters.

(iii) This chapter contains new experimental work and concerns the optically binding interaction between trapped colloids. Experiments were performed with a continous wave beam to establish the monochromatic binding interaction between two co-trapped particles. Furthermore, the chapter theoretically investigates the prospect of using broadband ultrashort pulses for optical binding and the resulting inter-particle interaction.

(iv) Next, this chapter consider the light-biological-matter interaction using broadband ultrashort pulses. In the first of these chapters I present a study of the parameter space required for laser-induced membrane permeabilsation using the technique known as optoinjection to characterise the probability of mammalian cell dye uptake caused by membrane permeabilisation. In the second part of this chapter the technique of phototransfection is discussed under the context of broadband ultrashort pulses.

(v) Finally, the propagation of broadband ultrashort pulses is investigated using a spatial light modulator to create novel beam shapes and to impart additional phase onto spatial components of the beam. This is potentially useful for optics having a spatially-dependent dispersion profile which cannot ordinarily be compensated for using a time-domain pulse shaper. In this chapter I demonstrate that a radial-dispersion dependence exists in lenses which cannot be compensated for using the MIIPS system alone. Therefore, use of a spatial light modulator operating in the spatial domain can be useful for measurement of spatial dispersion, and in future work, compensation of said dispersion could be achieved using the same spatial light modulator. This would have implications for practical applications such as in biophotonics involving ultrashort pulses a dispersion compensation scheme such as this could help ensure the shortest possible pulse was obtained and that the pulse was spatially adapted to the application, for example, by use of a Bessel beam.

Parameter	CW	Narrowband ultrashort pulse	Broadband ultrashort pulse
Average power (W)	1.0	1.0	1.0
FWHM pulse duration (fs)	∞	100	10
Pulse shape	N/A	Gaussian	Gaussian
Repetition rate (MHz)	N/A	80	80
Peak power (W)	1.0	1.2×10^5	1.2×10^6

Table 1.1: Peak powers calculated for a CW laser, Gaussian 100 fs pulsed laser and Gaussian 10 fs pulsed laser.

1.1 Introduction to ultrashort pulses

1.1.1 Peak power of ultrashort pulsed lasers

The laser has had a profound impact on scientific research in all aspects of the natural sciences. Consequently, advancement in laser technology has been driven by the desire to facilitate new scientific discovery and understanding. Many different laser types have been invented with advancements made in output power, wavelength, beam quality and laser pulse duration. Of these parameters, this chapter considers the pulse duration, which is inherently connected with the spectral content. Monochromatic lightmust be mathematically defined from minus to plus infinity in space or time [2]. Lasers which produce monochromatic light are generally associated with being continuous wave (CW) light sources due to their constant production of laser light. CW lasers are constrained by having a constant output power over time, which is a very useful property for many applications. Up to many tens of kilo-Watts of optical output power can be generated by certain types of CW laser, such as the increasingly important fibre laser [3]. An alternative way to increase the optical power is by pulsing the output, such that the laser continually generates optical pulses that exist for short periods of time, thus enabling the optical power to be concentrated in time with the laser output being essentially switched off otherwise. Pulsed lasers thus have a higher-than-CW peak power for the same amount of optical energy per unit time. Fig. 1.1 depicts the difference in peak power between a CW laser, narrowband ultrashort pulse laser of 100 fs full-width half-maximum (FWHM) pulse duration and a broadband ultrashort pulse laser of 10 fs FWHM pulse duration, with the parameters used listed in Table 1.1.

Fig. 1.1 shows that a dramatic increase in peak power can be obtained by decreasing

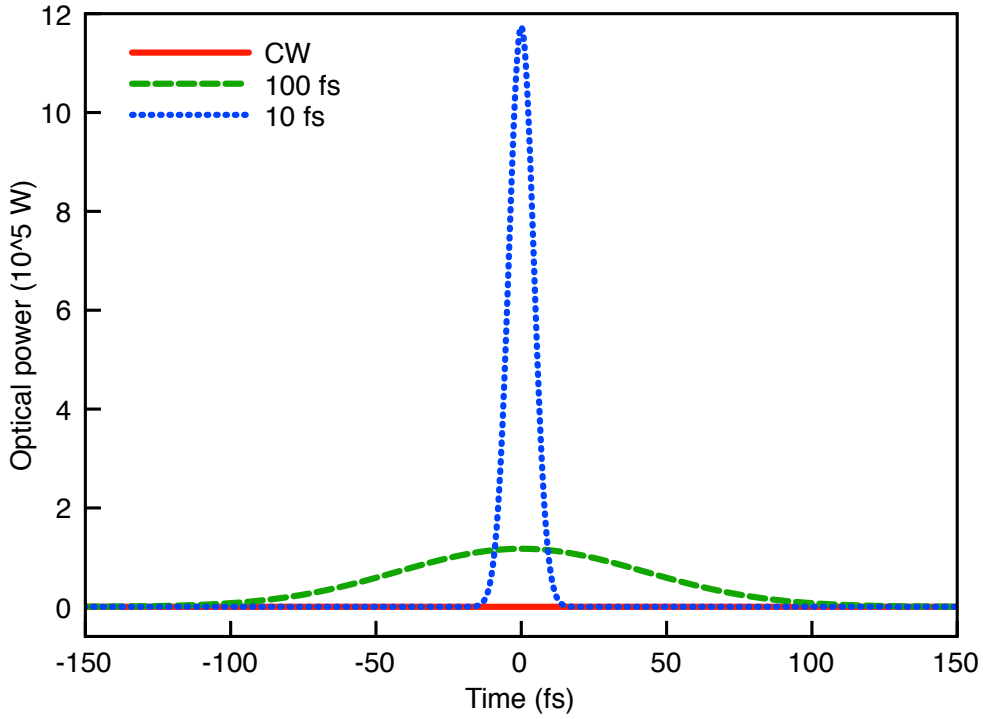

Figure 1.1: Comparison of the optical power associated with CW, ultrashort (usually referring to the range from sub-100 fs to sub-ps pulses) and broadband ultrashort pulses (conventionally, these are usually defined as sub-30 fs pulses, as is discussed below). Parameters used to produce this figure are provided in Table 1.1. Hereafter, pulse durations are defined according to their FWHM.

the pulse duration. The increase in peak power P_{peak} varies inversely with pulse duration τ_{s} according to

$$P_{\mathrm{peak}} = k_{\mathrm{s}} \frac{W_{\mathrm{p}}}{\tau_{\mathrm{s}}}, \tag{1.1}$$

where W_{p} is the pulse energy and k_{s} is a constant depending on the pulse shape [4]. Values for k_{s} for commonly used pulse shapes along with normalised expressions for the peak power for these pulse shapes are shown in Table 1.2 [5]. Fig. 1.2 illustrates the pulse profiles for the pulse shapes listed in Table 1.2. Although the pulse shapes appear similar, the peak power differs slightly in each case. Although this difference is small, this can make a big difference experimentally, particularly in the realm of nonlinear optics in which nonlinear effects are peak-intensity (peak-power per unit area) dependent [6]. It should be emphasised that the triangular pulse is intended as an approximate pulse shape

Pulse shape	Expression for $P_{\mathrm{peak}}(t)$	$k_{\mathrm{s}}(t=0)$
Triangular	$W_{\mathrm{p}}/\tau_{\mathrm{s}}\left((\tau_{\mathrm{s}}+t)/\tau_{\mathrm{s}}\right)$ for $-\tau_{\mathrm{s}} < t \leq 0$, $W_{\mathrm{p}}/\tau_{\mathrm{s}}\left((\tau_{\mathrm{s}}-t)/\tau_{\mathrm{s}}\right)$ for $0 < t < \tau_{\mathrm{s}}$, 0 otherwise	1.0
Gaussian	$W_{\mathrm{p}}/\tau_{\mathrm{s}}\sqrt{4\ln(2)/\pi}\exp(-4\ln(2)t^2/\tau_{\mathrm{s}}^2)$	0.94
Sech squared	$W_{\mathrm{p}}/\tau_{\mathrm{s}}\cosh^{-1}(\sqrt{2})\,\mathrm{sech}^2(2\cosh^{-1}(\sqrt{2})t/\tau_{\mathrm{s}})$	0.88

Table 1.2: Peak power expressions as function of time (t) for various pulse shapes with k_{s} values representing the relative difference in peak power for the listed pulse shapes. Appendix 7.1 discusses the calculations required to obtain the expressions and values for Gaussian and Sech-squared pulses.

and does not correspond to a physically realisable ultrashort pulse shape.

1.2 The relationship between spectral intensity and pulse duration

1.2.1 Interference of multiple waves

The laser pulse shape (and hence pulse duration) depends upon the generated spectrum associated with the laser pulses and as such, the laser spectrum defines the minimum possible pulse duration obtainable [4]. The minimum possible pulse duration is constrained by the spectral frequency width of the laser for a given spectral shape. The product of spectral bandwidth and minimum pulse duration is commonly known as the time-bandwidth product and has a value which depends upon the assumed pulse shape [4]. The resulting product obtained from measurement of the pulse duration and spectral width defines whether the pulse is transform-limited (minimum pulse duration) or not transform-limited (chirped pulse). By considering the coherent interference of multiple waves of different frequencies and examining the time domain the temporal shape of the pulse is obtained. The time-averaged intensity for multiple waves, E_{j} of different frequencies is given by [7]

$$I = \frac{1}{2}n(\omega)c\epsilon_0\left\langle \sum_{j=1}^{N} E_{\mathrm{j}} \sum_{j=1}^{N} E_{\mathrm{j}}^{*} \right\rangle. \tag{1.2}$$

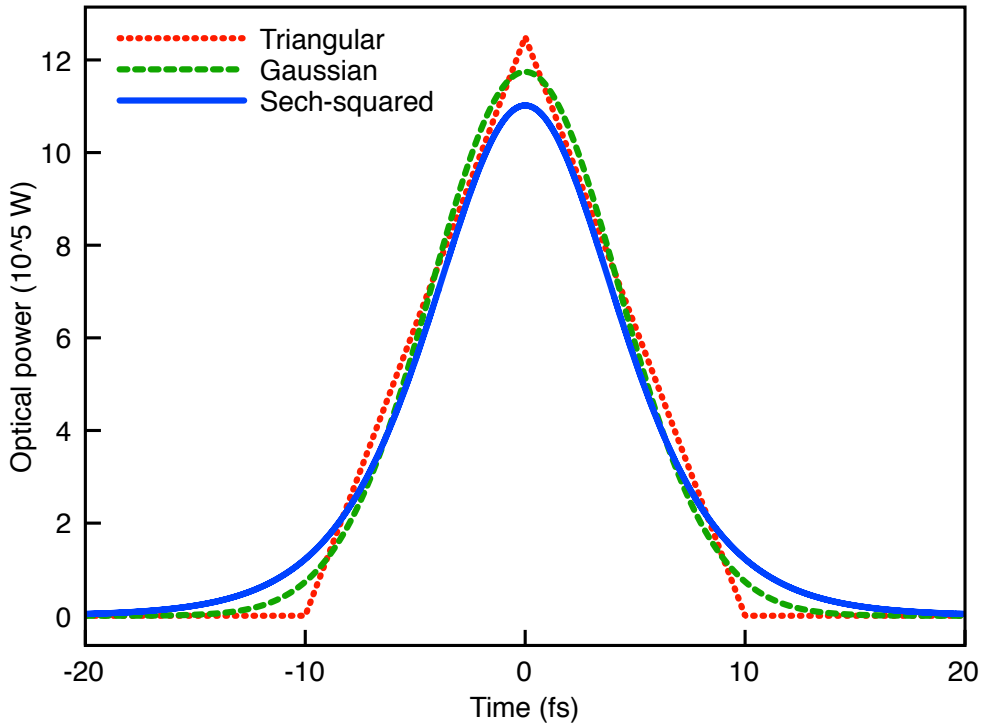

Figure 1.2: Profiles for Triangular, Gaussian and Sech-squared pulses, each with identical pulse energy W_{p}, as defined in Table 1.1. Note, this graph is intended for comparison purposes only. The triangular pulse defines a pulse shape for which the maximum possible peak power is defined by a k_s value of 1.0. However, although a triangular pulse is not physically realisable, it is valuable for making approximate calculations of peak power without the need for performing an integration procedure, as demonstrated in the Appendix for Gaussian and Sech-squared pulses.

where $n(\omega)$, c and ϵ_0 are the frequency-dependent refractive index, speed of light and vacuum permittivity respectively. The electric field (in the frequency domain) is given by

$$E(\omega) = E_0 \exp\left(-2\ln 2\left(\frac{\omega-\omega_0}{\Omega}\right)^2\right)\exp\left(i(\omega t+\phi(\omega))\right), \tag{1.3}$$

where E_0 is the peak electric field, which also has a spatial dependence (in Cartesian space), ω_0 is the centre frequency and $\phi(\omega)$ is the phase of the frequency ω. The constants $2\ln 2$ and Ω define the FWHM frequency bandwidth for a Gaussian-shaped spectrum. In this description, multiple waves of different amplitudes and frequencies are added together and multiplied by their complex conjugate. The interference of these multiple waves results

in a time-dependent intensity profile. Providing the phase $\phi(\omega)$ is zero, the interference of multiple waves defines the minimum possible duration of the resulting pulse. The intensity of the interference pattern is maximised when the waves are exactly in phase.

The more frequencies present within the spectrum (wider bandwidth) then the resulting interference pattern will be constrained to a narrower frame of time. Figs. 1.3 and 1.4 show the intensity-time profiles and the electric field amplitudes for two bandwidths typically available in Titanium-Sapphire ultrashort pulsed lasers (10 nm and 100 nm respectively, both centred at 800 nm). Comparing Figs. 1.3 and 1.4, shorter pulses are obtained in the broadband case due to the broader spectral content providing a range of frequencies which can only constructively interfere over a narrower time range by virtue of the substantially different frequencies within the pulse itself. In Fig. 1.4 this is illustrated by frequencies which go out of phase rapidly outside of t = 0 due to the difference in time period of each oscillation, for example, the red coloured frequency has a time period of approximately 3 fs and the violet-coloured frequency has a time period of 2.4 fs. Hence after several cycles the frequencies will become substantially out of phase. In both figures a time width of 40 fs has been selected to illustrate the overlapping of different spectral frequencies over that time width. For the narrowband case the different spectral frequencies remain mostly overlapped, and hence interfere (mostly) constructively within the 40 fs range. Whereas for the broadband case the different spectral frequencies rapidly go out of phase relative to each other by virtue of their substantially different cycle periods and hence destructive interference contributes to the shorter pulse duration shown. Both figures were generated using MATLAB code provided in the supplementary CD accompanying this thesis (see Appendix 7.5 for acknowledgements).

1.2.2 Fourier transform approach

This conceptual model vividly illustrates the relationship between electric field amplitude, frequency and phase in order to support ultrashort pulses. However, a more convenient method for calculating pulse shapes involves a mathematical approach for simultaneously dealing with multiple frequencies. In this approach the Fourier transform can be used to switch between time and frequency domain descriptions of a signal in terms of a time-varying function, $f(t)$ and a corresponding frequency function $f(\omega)$ [8]. The inverse Fourier transform converts a frequency signal, $f(\omega)$ to a time signal $f(t)$ and isgiven by

$$f(t) = \frac{1}{\sqrt{2\pi}} \int_{-\infty}^{\infty} f(\omega) \exp(i\omega t) d\omega = \mathcal{F}^{-1} \{f(\omega)\} . \tag{1.4}$$

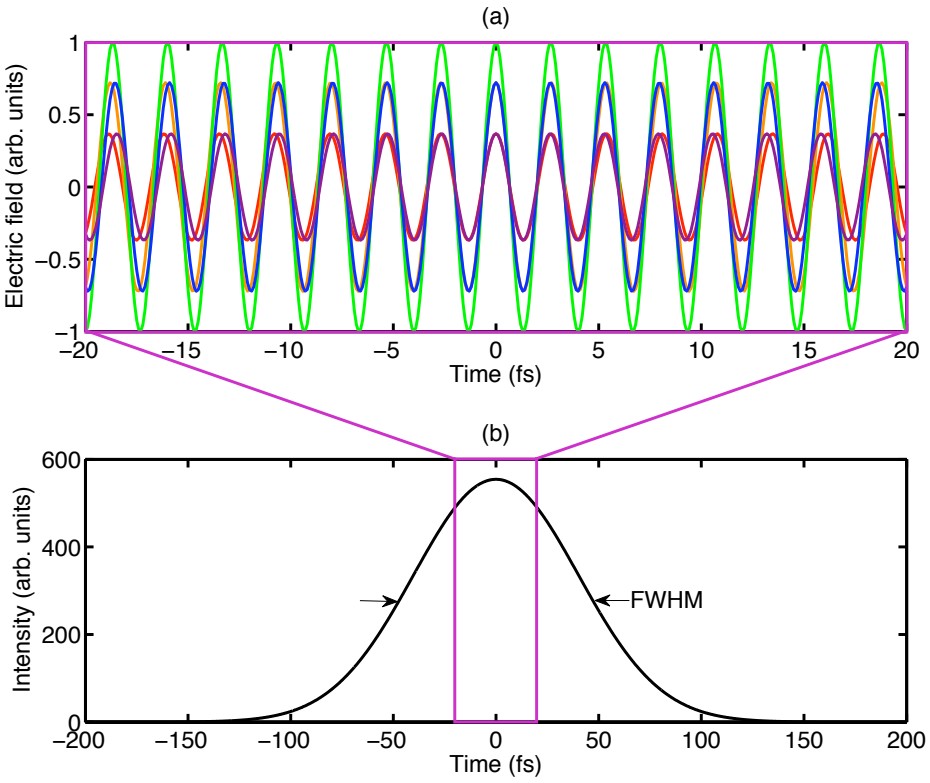

Figure 1.3: Interference of frequencies within a Gaussian narrowband (10 nm) spectrum, centred at 800 nm. Fig. (a) shows the electric field of several different frequencies contained within the spectrum. Different electric field amplitude contributions have been plotted; the colours refer to whether the wave is lower (red) or higher (violet) frequency. Fig. (b) shows the resulting pulse from the interference of all waves contained within the spectrum, with a FWHM duration of 94 fs. In order to retain clarity, the violet box indicates the time width correspondence between (a) and (b) as both are on different scales.

To convert from a time-domain signal to a frequency-domain function is provided by the complementary Fourier transform,

$$f(\omega) = \frac{1}{\sqrt{2\pi}} \int_{-\infty}^{\infty} f(t) \exp(-i\omega t) dt = \mathcal{F}\left\{f(t)\right\}. \tag{1.5}$$

This provides a suitable way for describing electric fields and for switching between their associated time and frequency domain descriptions. In equation 1.2 the interference of

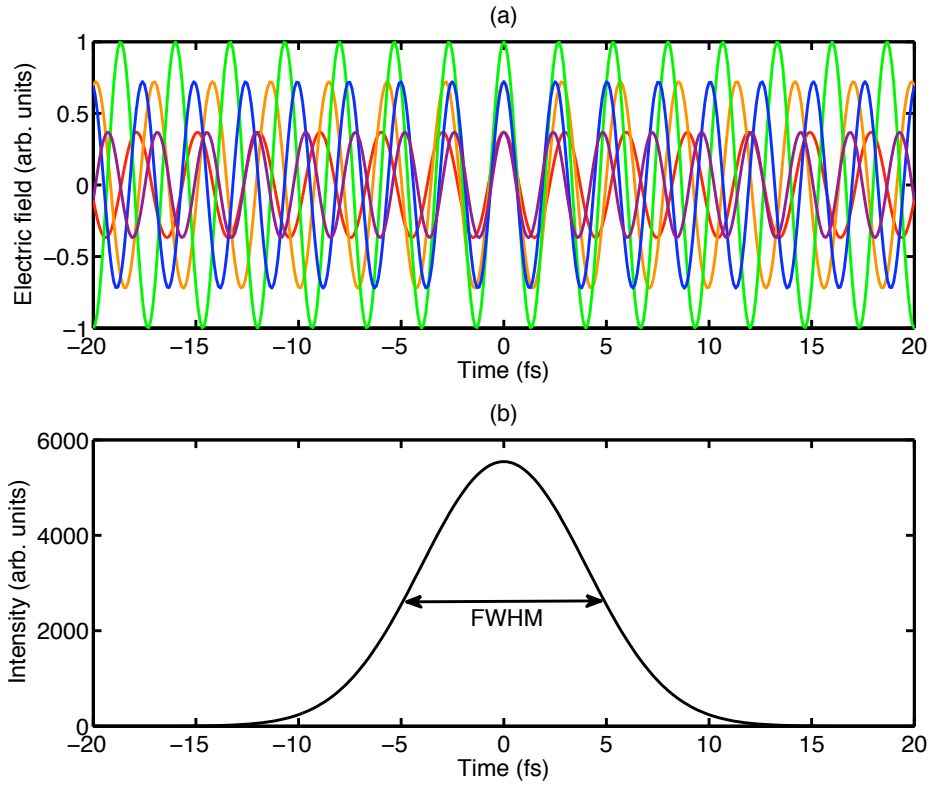

Figure 1.4: Interference of frequencies within a Gaussian broadband (100 nm) spectrum, centred at 800 nm. Fig. (a) shows the electric field of several different frequencies contained within the spectrum. Different electric field amplitude contributions have been plotted; the colours refer to whether the wave is lower (red) or higher (violet) frequency. Fig. (b) shows the resulting pulse from the interference of all waves contained within the spectrum, with a FWHM duration of 9.4 fs, a factor of ten shorter than in Fig. 1.3.

waves are described in terms of a sum of discretely-separated waves

$$E_{\text{total}} = \sum_{i=1}^{N} E_{\text{i}}(\omega, t) = \sum_{i=1}^{N} E_{\text{i}}(\omega - \omega_0) \exp(i\omega t + i\phi(\omega)), \tag{1.6}$$

where $E_{\text{i}}(\omega - \omega_0)$ describes the amplitude of the i^{th} electric field, $E_i(\omega, t)$ and the term, $\exp(i\omega t + i\phi(\omega))$ describes the oscillatory nature of the wave at a frequency ω, time t and spectral phase $\phi(\omega)$. Mapping the frequency domain from $-\infty$ to 0 is clearly not possible since there is no physical meaning to negative frequencies, however the choice of

function (such as a Gaussian centred at ω_0), which is zero in the region $-\infty$ to 0 solves this issue. In the limit of $\omega_{i+1} - \omega_{\mathrm{i}} \to 0$ the electric field function E_{i} may be represented by an integral across the frequency domain, with the possibility of the amplitude being represented by a continuous function, therefore with an existent integral within defined limits. Representing the electric field by

$$E(t) = \lim_{\delta\omega \to 0} \sum_{i=1}^{N} E_{\mathrm{i}}(\omega - \omega_0) \exp(i\omega t + i\phi(\omega)) \tag{1.7}$$

$$= \int_{-\infty}^{\infty} E(\omega - \omega_0) \exp(-i\omega t - i\phi(\omega)) d\omega, \tag{1.8}$$

which has the same form as the inverse Fourier transform of equation 1.4 (the factor of $1/\sqrt{2\pi}$ is an arbitrary part of the Fourier transform definition, but needs to be included in any calculation, where the product of the constants in equations 1.4 and 1.5 should equal $1/2\pi$). Therefore the Fourier transform integral can be used to represent the coherent sum of multiple electric field waves of different frequencies, and be converted to a time-domain description of the electric field, and vice versa, through calculation of the Fourier transform integrals. Hence, equation 1.2 can be re-written in terms of Fourier transform integrals as

$$I(t) = \frac{n(\omega) c \epsilon_0}{4\pi} \int_{-\infty}^{\infty} E(\omega - \omega_0) \exp(i\omega t + i\phi(\omega)) d\omega \int_{-\infty}^{\infty} E^*(\omega - \omega_0) \exp(i\omega t + i\phi(\omega)) d\omega \tag{1.9}$$

$$I(t) = \frac{1}{2} n(\omega) c \epsilon_0 \mathcal{F}^{-1}\{E\} \mathcal{F}^{-1}\{E^*\} \tag{1.10}$$

The Fourier transform approach is an alternative (and more common) method for calculating the pulse shape that results from a user-defined spectrum. In the following example, an experimental spectrum is used, rather than a theoretical spectrum, however the approach detailed previously is also applicable. There are two ways to calculate the Fourier transform integrals in equation 1.9; analytical or computational. Experimental narrow-band spectra can usually be fitted with either a Gaussian or Sech-squared profile, and therefore their associated Fourier transforms can be obtained analytically. For broadband spectra, this becomes more tricky due to the increasing complexity of spectral shapes with increasing spectral width, therefore a computational approach is required. The fast Fourier transform algorithm [9] allows for efficient computation of pulse duration from user-defined spectra and phase. Laser spectra are usually experimentally measured in the wavelength domain, therefore it is necessary to convert any experimentally measured

spectrum to the frequency domain,

$$\omega = \frac{2\pi c}{\lambda}, \tag{1.11}$$

where λ is the wavelength. The width of spectrum in the frequency domain, $\delta\omega$ is connected to the wavelength domain through differentiation of equation 1.11

$$\Delta\omega = \left| -\frac{2\pi c \Delta\lambda}{\lambda^2} \right| \tag{1.12}$$

Given the need to calculate the Fourier transform of the electric field amplitude from the spectral intensity, the wavelength-to-frequency converted spectrum is obtained and the square root of the measured spectrum is taken, $I(\omega)$ to obtain the electric field amplitude

$$E(\omega) = k_{\mathrm{ft}} \sqrt{I(\omega)}, \tag{1.13}$$

where k_{ft} is a constant which relates the intensity (frequency) to the electric field amplitude (frequency). The relationship between intensity (time domain) and electric field (time domain) is well established from Poynting's theorem [10]

$$I(t) = \frac{1}{2} n(\omega) c \epsilon_0 E(t) E^*(t), \tag{1.14}$$

where $n(\omega)$ is the frequency-dependent refractive index. The factor k_{ft} can be calculated by considering the experimental measurable quantities, pulse energy W_{p}, detector area and efficiency according to

$$W_p = \int_{-\infty}^{\infty} \int_{-\infty}^{\infty} \int_{-\infty}^{\infty} I(t) dx dy dt, \tag{1.15}$$

with $I(t)$ and $I(\omega)$ related by the Fourier transform. Starting from equation 1.13 we note that the phase requires the form $\exp(i\phi)$ and should be incorporated as follows

$$E(\omega) = k_{\mathrm{ft}} \exp\left(\frac{\ln(I(\omega)) + 2i\phi(\omega)}{2} \right). \tag{1.16}$$

For convenience the spectrum is then centred about zero and the fast Fourier transform is then applied to obtain $E(t)$ for any required phase $\phi(\omega)$, and thus the pulse shape can be calculated from equation 1.14. Fig. 1.5 shows the ultrashort pulse time profile calculated from the shown spectrum with zero dispersion to give the FWHM pulse duration of 13.6 fs. This minimum pulse duration is commonly referred to as being *transform limited*. The MATLAB code used to calculate the pulse shape and FWHM pulse duration in Fig. 1.5

is given in the supplementary CD accompanying this thesis (acknowledgements discussed in Appendix 7.5).

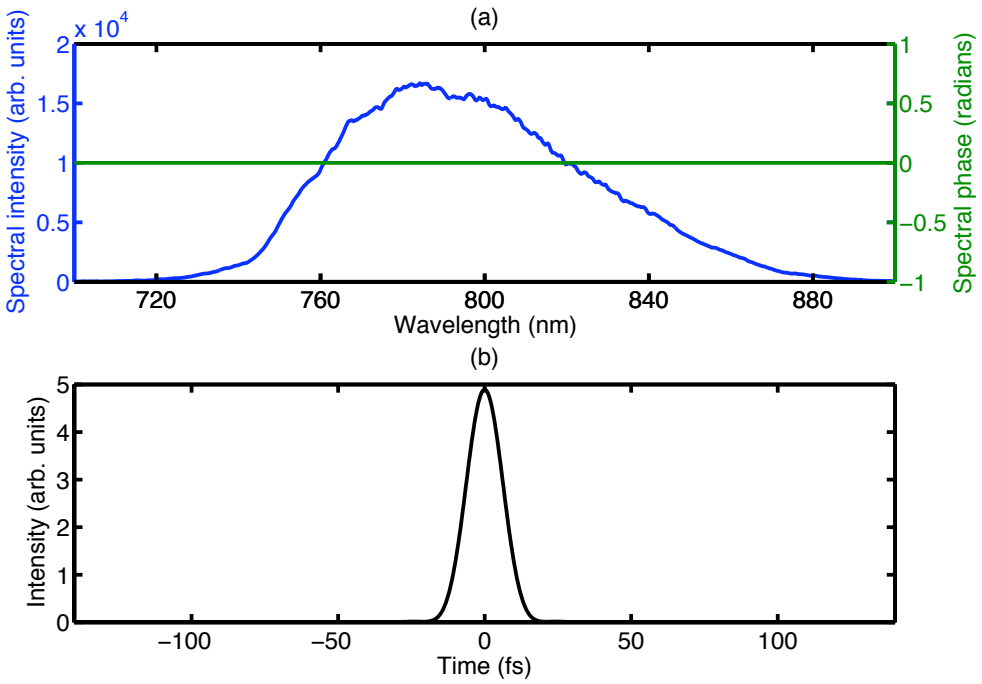

Figure 1.5: (a) An example of the experimentally measured spectrum from the KM Labs Swift 10 laser with zero spectral phase, and (b) the ultrashort pulse time profile, as calculated by the fast Fourier transform algorithm. This yields the minimum achievable (transform-limited) FWHM pulse duration of 13.6 fs.

1.2.3 Dispersion

When considering the propagation of ultrashort pulses in optical media dispersion becomes important. The velocity of propagation of an electromagnetic wave is frequency dependent, except in vacuo, where all electromagnetic waves travel at the same phase velocity (the vacuum speed of light), as can be demonstrated through solving Maxwell's equations [10]. This frequency dependent velocity is best observed in the natural world through the observation of the rainbow, in which white light from the Sun is refracted through water droplets at different angles, resulting in the well-known arc of spatially distinct colours in the rainbow.

Propagating electromagnetic waves have an electric field whose oscillatory space and

time dependence can be given by [7]

$$E = E_0 \exp\left(i(\mathbf{k}\cdot\mathbf{r} - \omega t + \phi(\omega))\right), \tag{1.17}$$

where $\mathbf{r}$ is a vector describing the position in space, and $\mathbf{k}$ is the wave vector, which defines the frequency dependence of the refractive index in any propagation direction in space. In any particular direction $\mathbf{k}$ provides the wave number,

$$k = n(\omega)\frac{\omega}{c}. \tag{1.18}$$

where $n(\omega)$ is the (frequency dependent) refractive index. The velocity of a set of propagating waves is given by the rate of change of frequency with respect to wave number, and is known as the group velocity,

$$\nu_g = \frac{\delta\omega}{\delta k}. \tag{1.19}$$

The quantity ν_g describes the propagation of a wave packet, and is dependent upon the optical properties of the propagation medium. For a particular wave, the phase velocity describes the velocity of propagation of an individual wave according to

$$\nu_p = \frac{\omega}{k}. \tag{1.20}$$

The quantities ν_g and ν_s are identical in a non-dispersive medium, where the refractive index is not a function of frequency. In this case

$$\nu_g = \nu_p = \frac{c}{n(\omega)}, \tag{1.21}$$

which is equal to c in vacuo, where $n(\omega) = 1$. In general, this is not the case. Even in air, where the refractive index is very close to unity, there exists a frequency dependent refractive index that is important, in particular for ultrashort pulses [11]. The physical origin of dispersion can be accounted for by considering the propagation of an electromagnetic wave through an atomic or molecular medium. This propagation occurs due to the atoms becoming polarised by the passing oscillatory electromagnetic field, and providing there is no absorption, the wave propagates through the medium unattenuated by virtue of the quasi-elastic restoring force acting on the electrons that have been polarised within the atomic or molecular medium [7]. However at frequencies where there is absorption, energy is transferred from the wave into the medium, with the energy dissipated either in the form of subsequent atomic emissions or heat [12]. The polarisability of a medium there-

fore defines the propagation of electromagnetic waves which pass through the medium, and features complex features such as resonances around given frequencies. This polarisability is therefore a complex function which depends upon the exact response of the atoms or molecules to a propagating electromagnetic wave. The linear polarisation induced by an electric field is proportional to the electric field amplitude and is given by

$$P = \epsilon_0 \chi^{(1)}(\omega) E, \tag{1.22}$$

where, E is the electric field and $\chi^{(1)}(\omega)$ is the susceptibility of the medium [6]. The susceptibility indicates the strength of the induced polarisation and can be described by [13]

$$\chi^{(1)}(\omega) = \frac{Ne^2}{m} \cdot \frac{1}{(\omega_0^2 - \omega^2) + i\omega\Lambda}, \tag{1.23}$$

where N is the density of polarisable atoms, e is the electron charge, m is the mass of the electron, ω_0 is the resonance frequency and Λ is a damping constant resulting from resonant energy transfer from the optical field to the medium, e.g. in the form of phonons. In the visible optical region, there are usually no resonances for typical optical materials such as glass [7]. By considering the typical resonances in the ultraviolet region the frequency-dependent refractive index is expressed in terms of a set of coefficients for increasing orders of frequencies, which is known as the Sellmeier equation [7]

$$n(\omega)^2 - 1 = A + B\nu^2 + C\nu^4 + \cdots - \frac{B'}{\nu^2} - \frac{C'}{\nu^4} - \cdots, \tag{1.24}$$

where ν is the optical frequency, as given by $2\pi\nu = \omega$. The Sellmeier equation can also be in terms of wavelength λ as

$$n(\omega)^2 - 1 = A + \frac{Bc^2}{\lambda^2} + \frac{Cc^4}{\lambda^4} + \cdots - \frac{B'\lambda^2}{c^2} - \frac{C'\lambda^4}{c^4} - \cdots, \tag{1.25}$$

where the coefficients A, B, B', C and C' are the Sellmeier coefficients, and are determined experimentally. With these coefficients established, the frequency dependent refractive index can be calculated for any given material for the visible region. Outside this region, resonances may have a significant effect.

Dispersion has serious consequences for ultrashort pulses resulting in pulses stretching in time when passing through optical media [13]. The frequency-dependent refractive index results in the phase of spectral components of an ultrashort pulse being shifted relative to each other. The most common way to express this mathematically is a Taylor

expansion about the centre frequency [14]

$$\begin{aligned}\phi(\omega) &= \phi(\omega_0) + \phi^{(1)}(\omega_0)(\omega-\omega_0) + \frac{1}{2}\phi^{(2)}(\omega_0)(\omega-\omega_0)^2 + \frac{1}{6}\phi^{(3)}(\omega_0)(\omega-\omega_0)^3 \\ &+ \frac{1}{24}\phi^{(4)}(\omega_0)(\omega-\omega_0)^4 + \cdots + \frac{1}{n!}\phi^{(n)}(\omega_0)(\omega-\omega_0)^n, \end{aligned} \tag{1.26}$$

where $\phi^{(n)}(\omega_0)$ is the nth derivative of the phase function with respect to frequency about ω_0. The derivatives of the phase, $\phi^{(1)}$, $\phi^{(2)}$, $\phi^{(3)}$ and $\phi^{(4)}$ are known as the group delay (GD), second order (group velocity) dispersion (GVD), third order dispersion (TOD) and fourth order dispersion (FOD) [14]. Each of these types of dispersion have a distinctive effect upon the initial pulse shape. GD results in a time delay of the group, shifting the pulse in time. GVD causes a smooth symmetrical stretching in time with no other distortion. This type of dispersion is very helpful for maintaining a well-defined and easily-calculated relationship between pulse duration and peak power. TOD results in a set of sub pulses which accompany the main pulse. The sign of the TOD defines whether the sub pulses precede or succeed the main pulse. FOD results in a symmetrical stretching in time with a more complex shape than for GVD and TOD. A combination of GD, GVD, TOD and FOD (and higher orders) results in very complex pulse shapes. Generally, optical systems have multiple contributions of different dispersion orders, hence pulse shapes tend to be complex. The MATLAB code included in the supplementary CD (acknowledgements in Appendix 7.5) explores how these types of dispersion influence the relative phase of different spectral components of the electric field and hence influencing the pulse shape.

Fig. 1.6 illustrates the effect of TOD in (b), FOD in (c) and GD, GVD, TOD and FOD combined in (d) upon the pulse in (a) with 100 nm bandwidth centred at 800 nm. Note the substantial decrease in intensity when additional dispersion is added.

In Fig. 1.6 an ideal Gaussian spectra was considered, however the true spectral shape of a typical ultrashort pulse is not well approximated by an analytic function. By using the Fourier transform method, the resulting pulse after GVD is shown to be inherently connected to the shape of the spectrum and therefore this method is very useful for calculating the pulse duration for a user-defined spectrum. Fig. 1.7 shows the same spectrum as in Fig. 1.5 but with 400 fs^2 of GVD applied (as might be obtained experimentally for typical optical systems with no higher order dispersion compensations) to give a FWHM pulse duration of 76.5 fs. Note how the shape of the spectrum affects the shape of the ultrashort pulse time profile.

A given amount of dispersion results in the increase in pulse duration. Therefore in certain situations it may be preferable to start off with a longer pulse duration so that

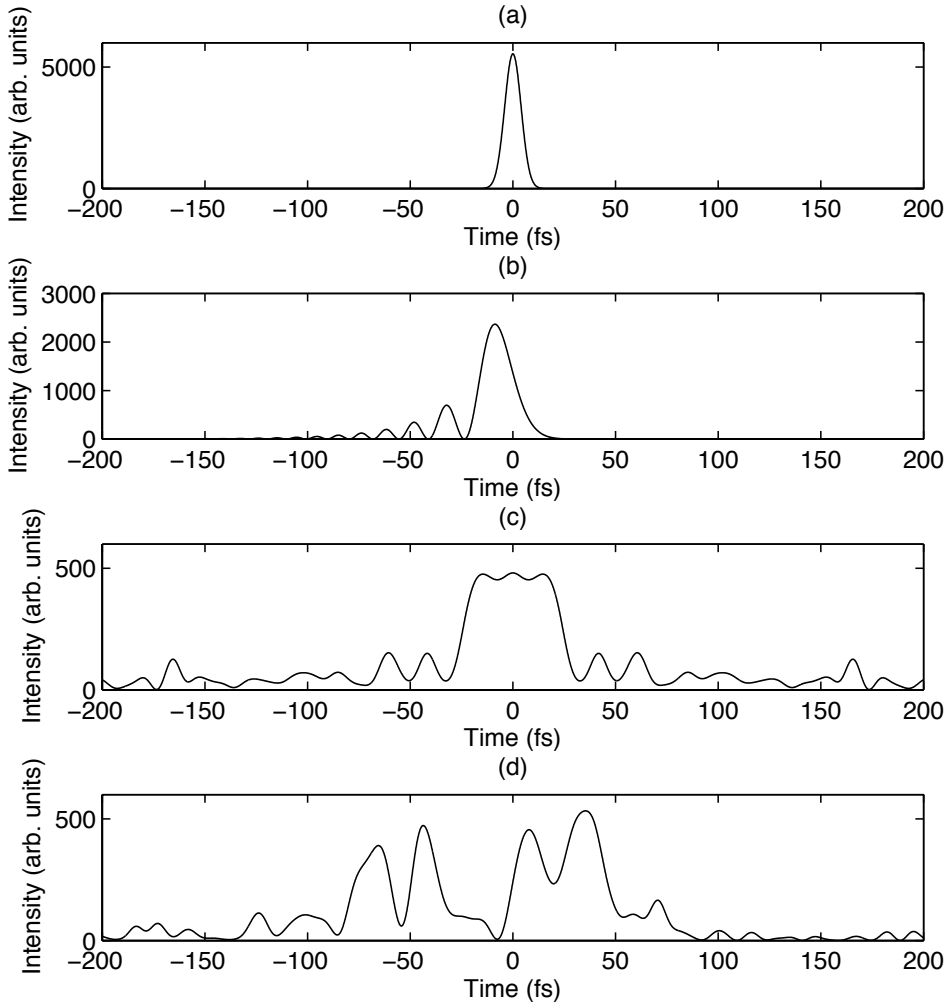

Figure 1.6: (a) A transform-limited pulse generated by 100 nm bandwidth centred at 800 nm; (b) the same pulse as (a) with 2000 fs^3 of TOD added resulting in decaying pulse shape oscillations; (c) the same pulse as (a) with 670000 fs^4 of FOD added resulting in a symmetrical complex pulse shape; (d) the same pulse as (a) but with -50 fs of GD, 300 fs^2 of GVD, 35000 fs^3 of TOD and -550000 fs^4 of FOD added resulting in an asymmetrical complex pulse shape.

the pulses are not necessarily increased in duration, thereby decreasing peak power. An estimate of the final pulse duration (τ_{final}) for a given initial pulse duration (τ_{initial}) for a

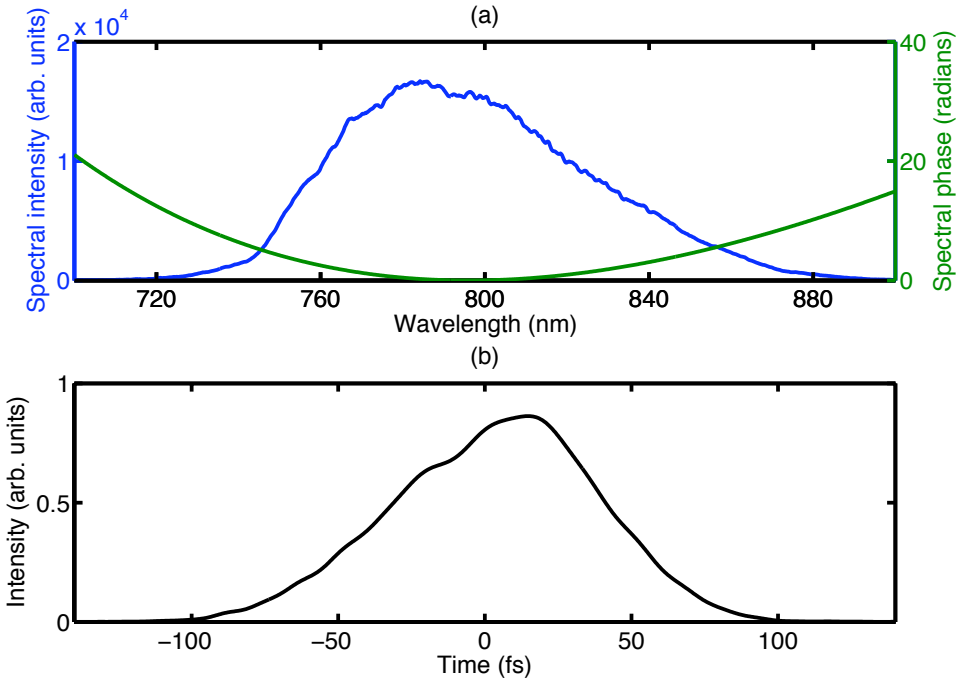

Figure 1.7: (a) An example of the experimentally measured spectrum from the KM Labs Swift 10 laser with theoretical phase function of the second order applied (400 fs^2), and (b) the ultrashort pulse time profile, as calculated by the fast Fourier transform algorithm. This yields the (non transform-limited) FWHM pulse duration of 76.5 fs.

Gaussian pulse is provided by [15]

$$\tau_{\text{final}} = \tau_{\text{initial}} \sqrt{1 + \frac{16 \ln^2(2) \phi_2^2}{\tau_{\text{initial}}^2}}, \tag{1.27}$$

where ϕ_2 is the GVD. Equation 1.27 is found by obtaining the inverse Fourier transform of the square root of the spectral intensity and including the second order dispersion term in the calculations. Squaring the result provides the temporal pulse shape and the FWHM time can be obtained from this and the ratio of final to initial durations calculated accordingly. Fig. 1.8 illustrates the increase in pulse duration for femtosecond systems covering the range from 5 fs up to 100 fs with 10000 fs^2 of GVD dispersion. A starting pulse duration of 10 fs results in a final pulse duration of 2.8 ps, whereas starting at 100 fs results in a pulse duration of 280 fs.

Optimum delivery of transform-limited ultrashort pulses can only be achieved through

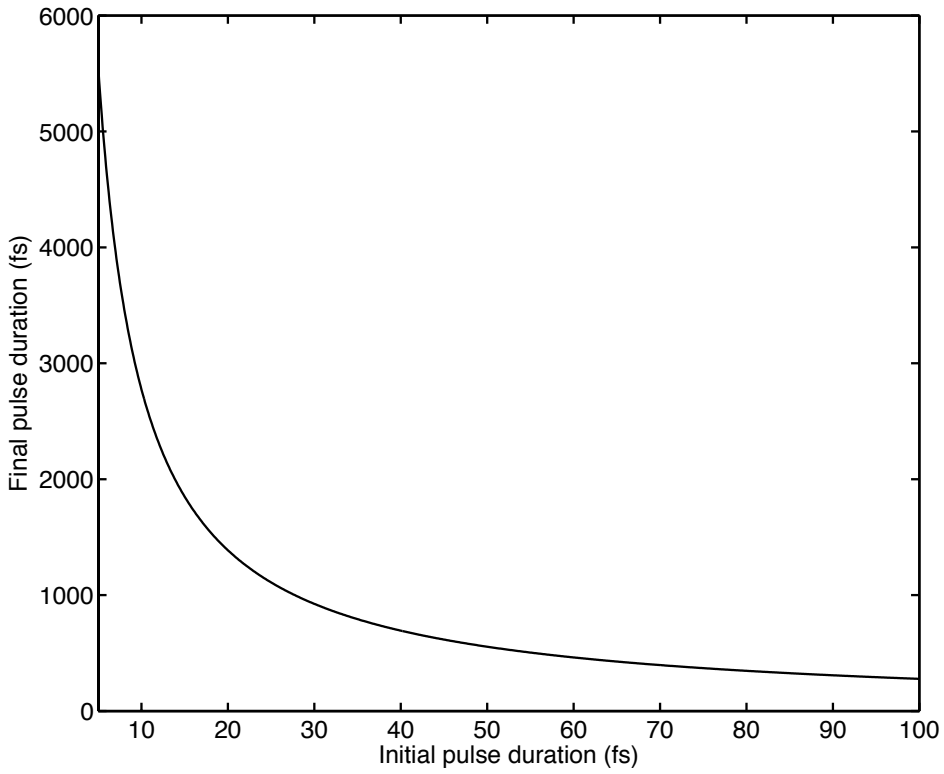

Figure 1.8: Graph illustrating stretching of pulse from initial to final durations using 10000 fs^2 of GVD dispersion, i.e. starting from transform limited pulse durations where the shortest initial pulse durations have the widest bandwidth, and conversely the longest initial pulse durations have the narrowest bandwidths.

dispersion compensation means. In an experimental setting the dispersion of an optical system should be at least calculated theoretically based on the choice of optics and the thickness of glass through which the ultrashort pulses pass. However, this is non-ideal as other environmental factors may influence results including temperature, pressure and humidity, which is especially true for broadband ultrashort pulses. Therefore, it would be preferable to measure the dispersion at a preferred point in the optical system and if possible, corrected or taken into account in any experiments performed. However in any application which may benefit from use of transform-limited pulses it would be necessary to perform at least some kind of dispersion compensation, for example, using prisms [16]. Prisms are relatively inflexible, however they do offer a relatively low-cost solution to the

problem. Many fields may stand to benefit from use of transform-limited ultrashort pulses, not least in biophotonics, where ultrashort pulses are regularly used for nonlinear imaging [17] and manipulation [18]. Biophotonics applications invariably involve a microscope objective for imaging purposes and delivery of laser. Microscope objectives suffer from significant dispersion owing to the contained glass [19] and have the potential to significantly temporally distort the ultrashort pulses. In this thesis, dispersion-compensated ultrashort pulses are applied through a microscope objective, in which the objective would otherwise stretch the pulses by many orders of magnitude. It is possible that through use of a reflective setup as well as a reflective microscope objective the optical system dispersion could be minimised. However, system dispersion may not be completely removed through use of this method and in the case of highly broadband sources, the pulse duration could still be stretched.

1.3 Nonlinear optics

A key aspect of this thesis is in the implementation of nonlinear generation of light and spectral measurements for dispersion measurement. A short review of the most relevant features of nonlinear optics is provided for reference purposes. In particular, the role of dispersion of ultrashort pulses in nonlinear crystals is discussed.

In linear optics the polarisation induced by a propagating electromagnetic wave is proportional to the strength of the electric field according to equation 1.22. However, in nonlinear optics the induced polarisation cannot be described by equation 1.22 as the polarisation no longer follows this simple relationship. This behaviour is most pronounced when using high intensity lasers, particularly when operating in pulsed mode. As such, it becomes necessary to employ a series expansion of powers to describe the polarisation (per unit volume) by

$$P(t) = \epsilon_0 \left[\chi^{(1)} E(t) + \chi^{(2)} E^2(t) + \chi^{(3)} E^3(t) + \cdots \right], \tag{1.28}$$

where $\chi^{(n)}$ is the n-th order nonlinear optical susceptibility, which is dependent upon the frequency, material type and propagation direction [6]. In equation 1.28 the higher order terms become relevant when the electric field amplitude is sufficiently large to initiate a nonlinear optical effect. The discovery of second harmonic generation (SHG) by Franken *et al.* in 1961 [20] is regarded as the beginning of the field of nonlinear optics [6]. SHG is one of many types of nonlinear optical interactions, and is of particular importance to the measurement and characterisation of ultrashort pulses. In this section, the nonlinear

optical interactions of greatest relevance to this thesis are described.

1.3.1 Second harmonic generation

A number of nonlinear optical processes can be described using a harmonic wave and inserted into the individual terms equation 1.28. In particular, by taking two different frequencies ω_1 and ω_2 with corresponding time-varying electric fields

$$E(t) = E_1 \exp(-i\omega_1 t) + E_2 \exp(-i\omega_2 t) + c.c. \tag{1.29}$$

and substituting into the second order nonlinear optical polarisation

$$P^{(2)}(t) = \epsilon_0 \chi^{(2)} E^2(t), \tag{1.30}$$

thus obtaining

$$\begin{aligned} P^{(2)}(t) &= \epsilon_0 \chi^{(2)} \left[E_1^2 \exp(-2i\omega_1 t) + E_2^2 \exp(-2i\omega_2 t) + 2E_1 E_2 \exp(-i(\omega_1 + \omega_2)t) \right. \\ &\quad \left. + 2E_1 E_2^* \exp(-i(\omega_1 - \omega_2)t + c.c.] + 2\epsilon_0 \chi^{(2)} \left[E_1 E_1^* + E_2 E_2^* \right], \right. \end{aligned} \tag{1.31}$$

where *c.c.* and * denote the complex conjugate of the previous sequence and of the field component, respectively. The efficiency of nonlinear optical processes depends on the material type, propagation direction and incident field strength. Second harmonic generated (SHG) light can be generated through a special case of sum-frequency generation and can be used to tunably generate higher frequencies. In summary, the ability to generate new frequencies using nonlinear optics is extremely useful when a desired frequency cannot be generated directly.

The characteristics of a material define the efficiency of SHG. SHG generally requires a material which has a non-centrosymmetric structure, that is, a material whose electrons sit within a potential energy function that is not symmetric about the centre [6]. Many materials have been produced which possess a non-centrosymmetric structure, and are typically in the form of a crystal [21]. A centrosymmetric material, which has a molecular structure leading to a symmetric potential energy functions will not allow SHG in its bulk [22]. SHG is allowable for a centrosymmetric material under specific situations, such as at the surface of the material [23], or when the centrosymmetric molecules collect in non-centrosymmetric aggregates [24].

In the context of this thesis, SHG refers to sum-frequency generation as broadband pulses permit intrapulse interference in SHG nonlinear crystals in which different frequency

components interfere. The nonlinear field intensity for sum-frequency generated waves having two different frequencies is given by

$$I_3 \propto I_1 I_2 \,\mathrm{sinc}^2\left(\frac{\Delta k L}{2}\right), \tag{1.32}$$

where I_1 and I_2 are the incident field intensities and Δk is the phase-matching term, as discussed below. When the incident fields have identical frequencies (ω) the nonlinear field (2ω) produced has an intensity dependence according to

$$I_{2\omega} \propto I_{\omega}^2, \tag{1.33}$$

where the subscript numbers have been replaced by the relevant frequency. Therefore SHG, and indeed any two-photon process has an intensity dependence which is quadratic with the incident intensity, and therefore SHG efficiency can be increased significantly by increasing the incident intensity, either through increasing the pulse energy, decreasing the pulse duration or through beam focussing [25].

1.3.2 Phase-matching

Phase-matching is essential in nonlinear optics as it describes the condition for conservation of photon momentum (k-vector) within a nonlinear crystal. Equation 1.32 is maximised when the phase-matching term Δk is zero

$$\Delta k = k_1 + k_2 - k_3 = 0, \tag{1.34}$$

where k_i is the i-th wavenumber. In general the phase-matching term is not equal to zero because the refractive index experienced by the field differs between the involved frequencies. In order to ensure phase-matching is optimised, the following is required

$$\frac{n_1\omega_1}{c} + \frac{n_2\omega_2}{c} = \frac{n_3\omega_3}{c}. \tag{1.35}$$

For SHG where $\omega_1 = \omega_2 = \omega_3/2$, equation 1.35 simplifies to

$$n_1(\omega) = n_3(2\omega). \tag{1.36}$$

This condition is difficult to satisfy due to dispersion and therefore SHG is normally phase-mismatched with the incident field. The standard strategy to deal with phase-mismatch is by employing a nonlinear material of polarisation-dependent refractive index. An example

of such a material is a anisotropic, or birefringent crystal [26]. The phase matching condition can then be satisfied by arranging the crystal such that over the interaction length of the crystal the effective path length of the different frequencies is the same. This can be achieved primarily by altering incident direction of the field (through angle tuning). In experiments involving SHG it was crucial to ensure correct crystal orientation to obtain maximum SHG spectral signal.

Ultrashort pulse SHG

Ultrashort pulses are associated with a range of frequencies and therefore any second-order nonlinear interaction will involve the combined effect of these frequencies, sum-frequency generation being the most relevant interaction. For convenience in this section, sum-frequency generation is referred to as SHG, in line with how ultrashort pulse SHG is normally referred to in the literature on the topic. Ultrashort pulse duration measurement techniques often require the use of SHG. Therefore the SHG produced by ultrashort pulses is of significant importance to pulse measurement, however ultrashort pulse SHG is significantly more complicated than CW SHG [27, 28].

In SHG involving ultrashort pulses the phase-matching conditions become more difficult to adhere to due to the large bandwidths involved. However phase-matching can be aided through the use of high numerical aperture objectives, in which the light is focussed into a tight cone, with the beam propagating at high angles into the nonlinear material, simultaneously satisfying the phase-matching conditions to some degree for all the contained frequencies [29]. In competition with phase-matching, spatial walk-off between the incident and generated beams due to material birefringence reduces the nonlinear conversion efficiency [30]. Phase-matching is of critical importance to the SHG process for any pulse duration, but the shorter the pulses are, then higher-order phase distortions come into effect. Second order dispersion brings about two effects. Firstly, a group-velocity mismatch (GVM) arises between the ultrashort (fundamental) pulse and the resulting SHG pulse [27]. GVM increases the duration of SHG pulses such that they become longer than that of the fundamental pulse and the nonlinear conversion efficiency is decreased [31]. However the effect is most pronounced for broadband ultrashort pulses, and type II SHG is more strongly affected than type I SHG, which has significant implications for autocorrelation experiments [32]. GVM can be minimised by decreasing the interaction length between fundamental and SHG pulses by decreasing the thickness of the nonlinear material [33]. The GVM manifests itself in terms of a temporal walk-off between the fundamental and SHG pulses [30]. The SHG efficiency can be affected by

the interplay between focussing strength and GVM [34], and SHG efficiency can be duly maximised by adjusting the GVM via a pre-dispersive method such as prisms [35]. In addition to GVM, intrapulse group-velocity dispersion (IGVD) introduces distortions to ultrashort pulses that are non-negligible for durations of less than 50 fs, and indeed become significant below the 10 fs regime [27]. IGVD is the group-velocity dispersion within the bandwidth of the fundamental and SHG pulses [27]. GVM and IGVD act together to affect the pulse characteristics of the fundamental and SHG pulses, and this phenomenon is further complicated by chirped fundamental pulses [28]. Higher order effects such as TOD and FOD will also complicate ultrashort pulse SHG [28]. It should be noted that in addition to SHG, third harmonic generation (THG) can be used for pulse measurement purposes, and as such, the phase-matching and spatial walk-off issues can be bypassed by using isotropic materials such as glass [36]. The disadvantage of THG is the generally lower nonlinear conversion efficiency compared with SHG and the higher generated frequencies are subject to greater scattering and absorption in optical materials.

1.3.3 Further considerations for ultrashort pulse SHG

In addition to the aforementioned there are further considerations in relation to ultrashort pulse SHG. Equation 1.32 shows the intensity of the phase-matching process, but this is defined for a set of three wavelengths (the pump, signal and idler). In broadband ultrashort pulse SHG the so-called signal and idler wavelengths (contained within the fundamental spectrum) combine to provide the so-called pump wavelength (SHG). Therefore the efficiency of the SHG process will vary according to the phase-matching relation between the range of wavelengths within the spectrum [6]. This results in a spectral acceptance bandwidth (also called phase-matching bandwidth) associated with a nonlinear crystal which defines a range over which SHG (or in relation to any other nonlinear process) can occur [37]. However, GVM between the fundamental pulse and SHG pulse limits the crystal interaction length, thereby decreasing the phase-matching bandwidth [37]. This means that shorter length crystals are required for broadband ultrashort pulse SHG in order to make use of broad spectral bandwidth. The spectral acceptance bandwidth (SAB) for type I phase-matching is provided by [37]

$$\Delta\lambda_{\mathrm{SAB}} = \frac{0.886\lambda_{\mathrm{f}}^2}{(n_{\mathrm{SHG}} - n_{\mathrm{f}})L_{\mathrm{cryst}}}, \tag{1.37}$$

where λ_{f} is the fundamental (centre) wavelength, n_{SHG} and n_{f} are the refractive indices of the fundamental and SHG (centre) wavelengths, respectively. The crystal length, L_{cryst}

can be varied to change the spectral acceptance bandwidth. Using equation 1.37 and 800 nm as the centre fundamental wavelength in Beta Barium Borate (BBO) for example, the spectral acceptance bandwidth of a crystal of length 1 cm is 1.1 nm, while for a 100 μm crystal it is 110 nm [21,38]. For the aforementioned ultrashort pulses, associated spectral bandwidths in excess of 1 nm will only be frequency doubled across the full fundamental spectral range, crystals thinner than 1 cm are required. Broadband ultrashort pulses such as those supporting 10 fs pulses or less require crystals of order 100 μm or less in order for efficient conversion of the full fundamental bandwidth for frequency doubling. While broad bandwidth acceptance is desirable for ultrashort pulsed SHG, the disadvantage of using thin crystals is that the overall conversion efficiency is decreased by virtue of the crystal thickness.

The phase-matching condition leading to a spectral acceptance bandwidth is closely associated with a so-called angular acceptance bandwidth. An expression can be found accordingly for the angular acceptance bandwidth [37]. Again, the angular acceptance bandwidth is similarly increased for shorter crystal lengths. For the aforementioned example of a BBO crystal, the angular acceptance bandwidth is 0.04 degrees for 1 cm crystal, whereas for a 100 μm crystal it is 4 degrees. Clearly these are much less than the angles obtained with high numerical aperture lenses but nevertheless, the increased intensity obtained by such lenses provides more efficient SHG by virtue of the intensity condition of equation 1.32 [21, 38]. As a phase-matching condition is defined for a single incident angle only, multiple phase-matching conditions are made possible by changing the angle of incidence. Therefore focussing on a nonlinear crystal invokes multiple phase-matching conditions simultaneously. This is useful for broadband ultrashort pulsed SHG as phase-matching is simultaneously achieved for a broader spectral range. However, the total conversion efficiency will be decreased as waves of given frequencies propagating at angles will not always follow the phase-matching condition appropriate for that frequency/angle combination. Although, schemes have been proposed in which different frequencies propagate at different angles, each of which are phase-matched appropriately [39, 40].

Further to the aforementioned effects, the temperature acceptance bandwidth defines a range of temperatures over which the phase-matching condition remains appropriate. However, in later experiments the temperature is held constant and therefore temperature fluctuations are not relevant. However a typical temperature acceptance bandwidth of 20 degrees Kelvin is obtainable with a BBO crystal.

All of the considerations above are important in decided how to select a nonlinear crystal for ultrashort pulsed SHG. In this regard, nonlinear crystals should ideally be as thin enough to overcome GVM and IGVD and permit sufficiently broad acceptance band-

widths. However, too thin and the overall conversion efficiency will mean the SHG signal will be decreased. Therefore, the crystal parameters should be appropriately calculated.

1.4 Generation of ultrashort pulses

Due to the significant relevance of ultrashort pulses for this thesis, it is appropriate to briefly discuss some of the theoretical and practical aspects of ultrashort pulse generation. However in the interest of brevity, the scope of this discussion is restricted to the key points of ultrashort pulse generation.

Nonlinear optical methods have led to significant developments in ultrashort pulse lasers, and in turn these ultrashort pulse lasers allow precise control over nonlinear optical processes [41]. A number of phenomena in a laser are required to act cooperatively in order to generate ultrashort pulses. The shortest pulses require the broadest bandwidth, and as such a gain medium is required that has a broad gain bandwidth. The most relevant example of a broadband gain medium is Titanium-doped Sapphire (Ti-Sapphire), which exhibits broad gain (fluorescence spectrum) [42] and can generate wavelengths ranging from 600 nm to 1200 nm, for example, supporting a 5 fs pulse [43]. Ti-Sapphire lasers primarily exhibit homogenous broadening, that is, the atomic dipole oscillators collectively experience the same energy-decay and de-phasing characteristics [44]. In particular, the (vibronic) broadening mechanism arises from heat energy (temperature) transfers acting upon the Titanium centres from the Sapphire lattice, thus creating the continuously varying fluorescence spectrum essential for broadband pulsed laser action [45]. The length of the laser cavity defines the frequency-mode structure of the fields which circulate in the cavity according to [44]

$$\nu_m = \frac{mc}{2n_{\mathrm{av}}L}, \tag{1.38}$$

where ν_m is the frequency of the m-th mode of a laser cavity of length L having an average refractive index n_{av}. For any mode to oscillate within a laser cavity equation 1.38 must hold and as such the modes are equally separated according to

$$\Delta\nu = \nu_{m+1} - \nu_m = \frac{c}{2n_{\mathrm{av}}L}. \tag{1.39}$$

The modes which experience gain greater than loss will oscillate within the laser cavity and contribute to the laser output; as such the broadening mechanism defines the number of modes which may oscillate [44]. Laser oscillators prefer to oscillate over a small number of modes, hence the gain tends to saturate over a limited spectral bandwidth [46], thus limiting the bandwidth potential of the laser oscillator. Since a broad bandwidth is required

to sustain ultrashort pulses, a gain modulation mechanism is required to de-saturate the gain and repopulate the gain bandwidth with more oscillating modes which retain a fixed phase relationship relative to each other. However the mode spacing is not in general equal, given the refractive index term n_{av} is frequency dependent. These modes therefore initially have a random phase relationship relative to each other and must be locked together (modelocking) in equal spacing in order to produce the wider bandwidth [13]. If the phase relationship between these modes becomes unlocked, the gain will re-saturate at limited preferential frequencies for the cavity configuration and the laser will no longer operate in pulsed mode, instead switching to CW mode.

The discovery of Kerr-lens modelocking (KLM) in 1991 heralded a new dawn of ultrashort pulse laser research [47]. The KLM scheme offered a convenient way to generate ultrashort pulses (initially as short as 60 fs [47]). Later, systems involving KLM incorporated significant developments in terms of dispersion compensation to provide substantially shorter pulses [48–50].

1.4.1 Dispersion management in femtosecond laser oscillators

There are two main methods used to compensate for dispersion inside femtosecond laser oscillators (intra-cavity dispersion compensation), these being prisms [16] and chirped mirrors [49]. The choice between prisms and chirped mirrors in laser oscillator depends on the user requirements. Dispersion-compensating prisms are associated with having lower cost with the ability to tune the dispersion and hence the centre wavelength and bandwidth, depending on the gain medium. However prisms cannot fully compensate for TOD and FOD while simultaneously compensating for GVD, and hence this leads to asymmetrical spectrum generation and hence pulse shape distortion [48]. Chirped mirrors can be designed to deal with the higher orders of dispersion inside the cavity and can readily generate cleaner sub-10 fs pulses [50]. Chirped mirrors are difficult and expensive to design and make and do not offer any spectral tuning ability, unless used in conjunction with prisms [51]. These dispersion compensation methods are later discussed in more detail under the context of extra-cavity dispersion compensation. In the work outlined in this thesis both methods of dispersion compensation are used in different commerical laser systems.

Firstly, a Femtolaser Scientific Pro Titanium-Sapphire laser was used to generate 12 fs pulses. The pump power was 5 W at 532 nm to provide an output modelocked power of 550 mW at around 800 nm (weighted centre wavelength). The stated M^2 value was $<$ 1.3. The dispersion compensation method used involved chirped mirrors designed to shift

the relative spectral phase of generated bandwidth so as to support the shortest possible pulses. This laser was used in the preliminary optoinjection and transfection experiments in chapter 4.

Secondly, a KM Labs Swift 10 was used to generate sub-12 fs pulses with the ability to change the spectral bandwidth to support longer pulse durations of around 35 fs. The average pump power was varied between 6-8 W depending on whether shorter pulses were preferred (lower average power) or longer pulses were preferred (higher average power). The pump wavelength was 532 nm. It was possible to tune the central wavelength of the optical pulses and associated spectral bandwidth. The tuning ability was provided by motorised prisms mounted to movably traverse the beam path to vary cavity dispersion, hence changing the resulting pulse duration. The stated M^2 value was < 1.1. The KM Labs Swift laser was used for all experiments outlined in this thesis other than those mentioned for the Femtolaser system outlined previously.

1.5 Applications of broadband ultrashort pulses

In this thesis several aspects of broadband ultrashort pulses were investigated. The term broadband is generally used to refer to pulses which have sufficient bandwidth that after travelling through dispersive optics, dispersion causes pulses to be shaped temporally; substantially so and enough to appreciably stretch (or compress) the pulses accordingly. Naturally this depends upon what kind of optics are used but typically for Ti-Sapphire wavelengths (around 800 nm) the threshold transform-limited pulse duration below which dispersion becomes significant is 30 fs [52]. Measurement and control of chromatic dispersion is key to applying broadband ultrashort pulses in a variety of situations. In this thesis several distinctly different situations involving broadband ultrashort pulses are considered. Firstly, chapter 2 introduces dispersion compensation methods and experiments, in particular focussing on the apparatus used in experiments to measure and deal with dispersion, referred to as multiphoton intrapulse interference phase scan (MIIPS). The MIIPS method was essential for many of our experiments as without it the dispersion caused significant pulse stretching. Chapter 3 further examines the light-matter interaction, but instead in dielectric colloidal systems in which focussed laser light can trap colloids in such a manner that the colloids and light self-consistently interact in what is known as optical binding. In this chapter experimental studies demonstrate the optical binding effect in the CW regime and theoretical studies investigate the optical binding phenomenon when subjected to broadband ultrashort pulses. Chapter 4 concerns the interaction between broadband ultrashort pulses and biological matter. These chapters discuss laser-induced

membrane permeabilisation for introduction of dye and genetic material. In particular, experiments are introduced which, to-date, cover the widest parameter space relevant for membrane permeabilisation. Finally, chapter 5 begins to examine the nature of broadband ultrashort pulse beam propagation. This chapter builds upon the pulse shaping chapter by introducing the concept of spatial pulse shaping, in which spatial modulations reveal temporal changes in the beam. Through use of a spatial light modulator I performed experimental studies concerned the propagation of broadband ultrashort pulse Gaussian and Bessel beams.

1.6 Conclusions

This chapter is intended as an introduction to ultrashort pulses and highlights some of the key issues in the present context. In particular, the pulse shape is considered to be critical for defining the peak intensity, and hence the strength of any nonlinear interaction. An increase in peak power can be achieved by increasing pulse energy or decreasing pulse duration. Decreasing the pulse duration is a way of increasing the peak power without increasing the total energy delivered by any sequence of pulses. However, a decrease of pulse duration can only be sustained through an increase in spectral bandwidth. This is a particular issue for the shortest of ultrashort pulses, whereby dispersive effects cause the relative spectral phase to be distorted, hence increasing the pulse duration and decreasing the peak intensity. Dispersion compensation is therefore required to deal with these dispersive effects for optimum delivery of transform-limited ultrashort pulses. Ultrashort pulses are becoming increasingly important in many fields, particularly in biophotonics, wherein ultrashort pulses are used for imaging and manipulation purposes. It is particularly crucial that dispersion is dealt with in systems requiring the shortest available pulse duration in order to take maximum advantage of the peak intensity available. A key topic of the following chapter on pulse shaping addresses some of these issues and investigates a commercially-available solution to the dispersion problem for the experimentalist. In particular, I demonstrate a commercial pulse shaper referred to as multiphoton intrapulse interference phase scan, which is used in combination with SHG spectral measurements for dispersion measurement and compensation. The pulse shaping chapter builds upon the foundations provided by this chapter and leads on to subsequent chapters in which dispersion-compensated ultrashort pulses are delivered for several applications concerning the light-matter interaction in terms of (i) optical trapping and binding; (ii) manipulation of biological matter through nonlinear-initiated processes and (iii) propagation of novel beam shapes which are affected by spatio-temporal distortions, whereby spectral

and spatial phase can affect the outputted beam profile and hence peak intensity, thereby linking back to optical trapping and binding, and biological manipulation in that the peak intensity is extremely important for defining nonlinear processes therein.

1.7 Chapter acknowledgements

The author designed all models used in this chapter to generate figures.

Chapter 2

Control of broadband ultrashort pulses

2.1 Introduction

The previous chapter introduced ultrashort pulses along with their respective advantages and disadavantages. Principally, ultrashort pulses have the advantage that they may offer enhanced peak intensity for any given pulse energy. However, this advantage can be nullified, and in fact made worse by dispersion. The purpose of this chapter is to follow on from the discussion of the previous chapter and introduce pulse shaping and measurement techniques for (i) measuring and (ii) dealing with dispersion. The ability to accurately measure and control the spectral phase, or dispersion allows complete control over the temporal features of an ultrashort pulse. Established methods of controlling dispersion are discussed and a detailed description of the dispersion control method used in our experiments, known as MIIPS is presented. Finally, we discuss experiments performed using our laser and dispersion control system and relate the results to future chapters in this thesis. The purpose of this chapter is therefore to explain in detail the control of ultrashort pulses in our experiments so that future chapters can focus on the experiment concerned while referring back to this chapter if necessary. This chapter also critically discusses features of the MIIPS system along with known issues and strategies for optimising performance.

2.2 Management of dispersion in optical setups

One of the main barriers to the use of broadband ultrashort pulses is that the dispersion introduced by optical elements is significant and can result in pulse distortions (temporally

and spatially) which increase the pulse duration and decrease the peak optical power. Fig. 1.8 illustrated how an ultrashort pulse can become significantly increased in duration if the initial duration is too short. In reality this means that it is better to start off with an ultrashort pulse that is initially longer and hence not-broadband so that dispersion is no longer such a significant issue, rather than waste effort on intra-cavity and extra-cavity dispersion compensation. However if broadband ultrashort pulses are required, then some means of dispersion management is required in most setups. There are two aspects to dispersion management: measurement and compensation. Accurate measurement of dispersion is critical, particularly for the shortest pulse durations, however in-situ dispersion measurement is non-trivial and the following sections discuss dispersion measurement in detail. Once the dispersion has been measured dispersion compensation methods can be designed and controllably utilised to deal with the dispersion in the setup.

2.3 Established methods of dispersion compensation

In this subsection the current technologies used for dispersion compensation for both intra-cavity and extra-cavity purposes are discussed.

2.3.1 Prisms

Prisms are dispersive optical elements that introduce a form of geometrical dispersion resulting in an angular spread of spectral components (angular dispersion) within a beam [13]. Fig. 2.1 illustrates a two-prism arrangement in which prism (a) introduces an angular spread that results in the lower optical frequencies exiting the prism at a different angle to the higher optical frequencies. This angularly spread beam is introduced into prism (b), at which point the beam frequency components have become spatially distinct, propagating at different angles. After propagation through prism (b) the beam contains the spatially distinct frequency components propagating parallel to each other. Prisms (c) and (d) mirror prisms formation (a) and (b) and return the beam to its original shape, with spatially recombined spectral components that have been dispersed according to the prism configurations and materials. The angular spread introduced by prisms is due to the frequency-dependent refractive index experienced by the input beam resulting in an angular deviation according to Snell's law [2]. For positive dispersion the lower frequencies experience a lower refractive index than higher frequencies, so the higher frequencies become phase-delayed with respect to the lower frequencies. The spatially distinct frequency spread is referred to as angular dispersion and is a special case of spatial chirp [13].

Adjusting the separation between (a) and (b) (and (c) and (d)) in Fig. 2.1 results in a course GVD tuning, while lateral insertion of prisms (b) and (c) provides fine-tuning of the GVD [15]. This prism arrangement provides negative GVD tuning by delaying shorter frequencies by effectively passing them through more prism material, thus compensating for positive GVD [16]. However prisms do not readily compensate for higher order dispersive effects and as a result they cannot generally create sub-10 fs pulses [48]. In general

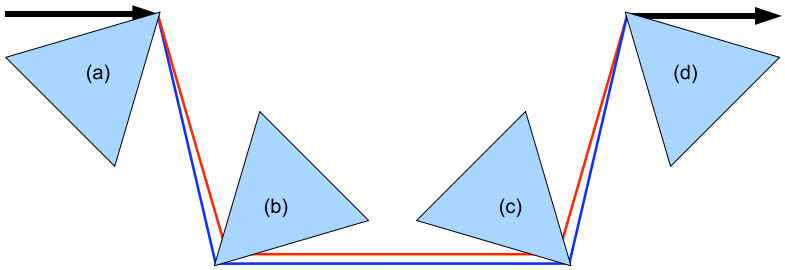

Figure 2.1: The four-prism sequence which allows GVD compensation whilst simultaneously dealing with the spatial chirp introduced by prism (a) and (b). One or two prism arrangements can be used, however these introduce unwanted spatial chirp that must otherwise be corrected for.

prisms offer good negative GVD compensation and have low insertion losses at Brewster's angle [2]. However their lack of higher order dispersion compensating ability limits their application in the formation and control of the shortest of ultrashort pulses. They also require careful alignment and can take up significant space in an optical setup unless novel arrangements are considered such as the single prism 4-pass compressor [53].

2.3.2 Diffraction gratings

Diffraction gratings also introduce angular dispersion to a beam [54]. Like prisms, diffraction grating pairs can be utilised to shift the phase of spectral components of a pulse and provide another route for pulse compression [55]. Fig. 2.2 shows a diffraction grating configuration involving a reflecting mirror which can be used to control the dispersion and remove spatial chirp [14]. By varying the distance between the second grating (G2) and the image of grating (G1), the dispersion is altered. A large variety of grating configurations have been demonstrated and implemented in ultrashort pulse dispersion compensation schemes. In particular, rather than using lenses (which introduce dispersion and chromatic aberrations) as in Fig. 2.2, it is possible to implement an all-reflective scheme that

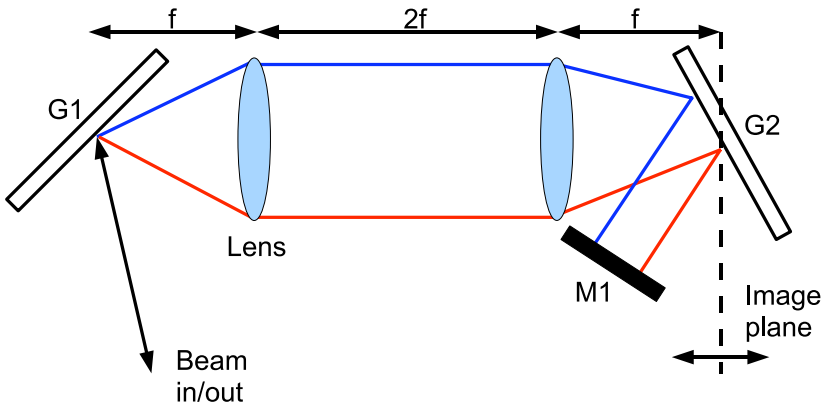

Figure 2.2: A telescope arrangement between a grating pair in the so-called 4-f arrangement [56] provides a means for dispersion compensation. The 4-f arrangement is discussed in more detail in the spatial light modulator section. Note, the angular displacement is exaggerated in this example, wherein the image plane defines the image of grating G1 through the telescope arrangement.

eliminates these issues [57]. Furthermore, sets of 4-prism and 4-grating arrangements have been used to compress chirped pulses to six femtoseconds [58]. A more compact arrangement has been achieved through novel arrangements of prisms and gratings to achieve GVD and TOD compensation [59].

Unlike prisms, gratings are not (in general) used inside laser cavities for dispersion compensation due to the higher losses introduced by the grating, especially into the higher diffraction orders. Gratings are however successfully implemented in high energy ultrashort pulse systems such as in chirped pulse amplification (CPA) whereby grating pairs disperse a pre-generated ultrashort pulse to lower its peak power to prevent damage to the enclosed gain medium, with the second grating subsequently re-compressing the pulse [14, 57].

2.3.3 Chirped mirrors

Chirped mirrors, consisting of multiple layers of high and low refractive index dielectric coatings have been successfully implemented to compensate for dispersion in optical setups with pre-calculated or pre-measured dispersion [50]. Chirped mirrors are often used in Ti-Sapphire oscillators to generate ultra-broaband bandwidth which, when compressed, yields sub-5 fs pulses [60, 61]. However they can also be used for extra-cavity

dispersion compensation [62]. The design of chirped mirrors differs from that of standard Bragg mirrors in that the layer-to-layer thickness varies. Accordingly, as the periodicity of the grating increases, so does the reflected wavelength. Therefore, by depositing the longer wavelength layers deeper than shorter wavelength layers, the longer wavelengths are delayed with respect to the shorter wavelengths, thereby contributing to a negative GVD [63]. In this way, the dispersion can be pre-tuned according to the required dispersion configuration by layering different index layers of different thicknesses. Generally this results in an extended reflectivity range and allows the incorporation of a frequency-dependent group delay dispersion and if no glass or prisms are used in the setup the higher order dispersive effects are minimised [63]. An extension of the chirped mirror design is the double-chirped mirror, which utilises an impedance matching section, which aims to minimise the interference between small reflections from the front portion of the mirror, and the more-substantial reflections from the rear part of the mirror [63]. This type of interference results in oscillations in the frequency-dependent group delay, as seen in Gire-Tournois interferometers, in which higher-order dispersion control is limited [63–65]. Chirped mirrors need to incorporate a highly reflective (low loss) broadband design with well engineered multi-layer coatings for accurate dispersion control [66]. They are used in multiple beam reflection configurations for maximising the introduced dispersion [50].

2.3.4 Spatial light modulators

A spatial light modulator (SLM) is a device which modulates amplitude or phase of light which pass through spatial positions within the modulator. They are best utilised in the Fourier plane in a 4-f configuration as per Fig. 2.3, which is a small modification of the apparatus in Fig. 2.2. Spatial light modulators (SLMs) offer a convenient way to control dispersion and they come in a number of formats. SLMs can be operated in many different configurations and have the potential for near-unlimited control over ultrashort pulses. This level of control differs to prisms, where the control is limited, and chirped mirrors, which offer no adjustability. SLMs have the disadvantage that they require careful calibration and computer control if they are to be adapted actively. Originally, SLMs were not actively adaptable and employed a pre-designed phase mask to control dispersion [56]. In these pre-designed masks, phase and amplitude features were imprinted upon a transparent substrate to effect changes in the properties of the pulses. In its simplest example, amplitude-only modulation can be implemented by physically blocking some of the spatially separated frequencies, thus lengthening the pulse duration. Phase-only modulation can be used to synthesize any required dispersive characteristics and does not imply any

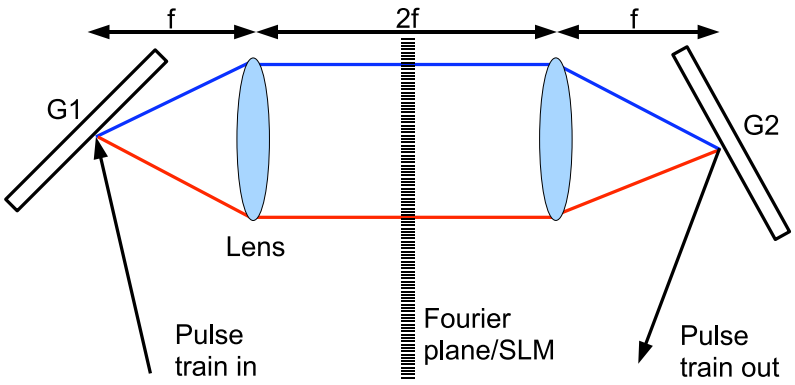

Figure 2.3: An example pulse shaper featuring 4-f arrangement with a spatial light modulator located in the Fourier plane, which can be utilised in either amplitude-only, phase-only, and dual amplitude and phase operation.

spectral loss.

The manner of actively modifying an SLM can take several forms. Acousto-optic modulation (AOM), in which a crystal is driven with a radio-frequency voltage signal and a traveling wave is formed which modifies the refractive index according to its position in the crystal [67,68]. Therefore AOM requires constant updating from the signal generator or computer and is unsuitable for use with MHz repetition rate lasers [69]. Deformable mirror (DM) technology includes an array of electrically-addressed actuators under a mirrored membrane which effectively create an position dependent phase modulation line, which can be utilised either in extra-cavity pulse shaping [70] or intra-cavity pulse control [71]. Liquid crystal spatial light modulators (LC SLMs) are very commonly used for pulse shaping purposes [69]. The most common type of LC SLM make use of the electro-optic effect to effect a refractive index and/or birefringence change upon light passing through the cell [69]. Less commonly used are optically addressed LC SLMs which make use of the photo-conductive effect to continuously vary the conductivity between electrodes to eliminate pixelation effects [72].

The most relevant type of SLM for this thesis is the electrically-addressed LC SLM and is discussed in more detail here. LC SLMs consist of an array of windows, or pixels containing a liquid crystal (LC) whose properties are adjusted according to the voltage applied by an individual electrode. The LC consists of a set of molecules (usually nematic, wherein the long axis of the crystals are arranged in parallel lines) that are elongated

and align according to the applied electric field [73]. The alignment of these molecules within the electric field effects either a refractive index or polarisation change. Depending on the application the array of pixels may be enclosed within half-waveplates and/or polarisers. In the case of half-waveplates, the LC cells require the correct input polarisation so waveplates are used to appropriately adjust the input polarisation. Twin polarisers are used (either in crossed or uncrossed configuration depending on LC configuration) to allow pixel-amplitude control by rotating the polarisation by 0-90 degrees to continuously vary the transmission from 0 to 1. To obtain dual phase and amplitude control, two separate electrically-addressed pixel arrays are required; these arrays can be positioned together at the Fourier plane within the shaper [74]. In this dual arrangement type the phase and amplitude LC arrays are accurately bonded together, one array with molecules aligned at -45 degrees, the other array with molecules aligned at +45 degrees, that is, within the plane perpendicular to the beam propagation direction with respect to the defined polarisation axis. The LC arrays are sandwiched between polarisers in the uncrossed formation. The pixels are operated such that they cooperatively modulate the amplitude and phase. With no voltage applied to the LC cell the molecules are aligned with their long axis parallel to the plane previously defined, and upon application of the voltage the molecules orient themselves towards the propagation direction. This alters the refractive index of the pixel concerned. Since each pixel in the first array is co-aligned with its corresponding pixel in the second array and the refractive index is modified independently in orthogonal directions (-45 and +45 degrees) it is possible to change the phase according to the average refractive index imparted upon the beam [75]

$$\phi_{\text{phase}} = L\omega \frac{n_1(V_1) + n_2(V_1)}{2c}, \tag{2.1}$$

where L is the pixel length (along the propagation axis), n_1, n_2 are the refractive indices of the pixel concerned in the two pixel arrays at the specified voltages V_1 and V_2, respectively. For the amplitude change the difference in orthogonal refractive indices defines the birefringence, and hence changes the phase difference and is given by

$$\phi_{\text{amplitude}} = L\omega \frac{n_1(V_1) - n_2(V_1)}{c}. \tag{2.2}$$

The second polariser then allows or rejects portions of light through given pixel pairs. Through careful calibration this allows complete, independent control of phase and amplitude of spectral components of the pulse.Figure 2.4 shows a simplified diagrammatic illustration of elements of the previously described spatial light modulator. In the illus-

tration pixel arrays 1 and 2 are shown with liquid crystal directions indicated by diagonal lines oriented at 45 degrees to the left and right, respectively. Only 16 pixels are shown in these arrays for simplicity. In the SLM these pixel arrays would be affixed adjacent each other to achieve the aforementioned control of phase and amplitude. Diagrams (a) and (b) show the orientation of the liquid crystals in a cross-section of a pixel unit. The liquid crystals are positioned between electrodes which apply the voltage signal in the direction shown. In (a) the voltage is 0, however in (b) the voltage is turned on, which results in the liquid crystals being aligned in the electric field as shown. This described arrange-

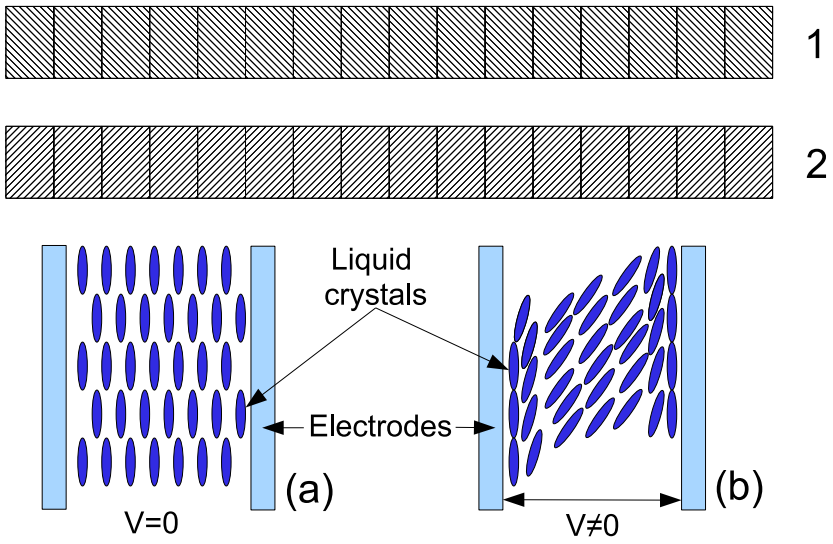

Figure 2.4: Diagrammatic illustration of SLM components, including 16 pixel arrays 1 and 2, each of which is shown with liquid crystals oriented at 45 degrees left and right. The pixel arrays are configured to be sandwiched together such that independent control of each pair of corresponding pixel pair permits phase and/or amplitude control. In (a) and (b) a pixel cross-section is shown with liquid crystals (a) oriented perpendicular to the applied voltage (V) direction $V = 0$ and (b) oriented towards the applied voltage direction with $V \neq 0$.

ment is utilised in the LC SLM in the pulse shaper described later in this thesis.. The response of the LC to the applied voltage and temperature defines the optical properties of the SLM. Therefore careful calibration at constant temperature is required for both phase and amplitude control. Furthermore, as the pixels have a finite size with a small

gap between each pixel, the SLM does not offer truly continuous phase and amplitude control over the entire spectral content of the pulse. Therefore diffractive effects from sudden phase-jumps in the pixel-pixel transitions within the arrays result in dips in spectral power at the spectral pixel locations. As such, these features cannot be removed without infinite pixel resolution and they are inherent to pulse shaping systems [75]. This is not a significant problem unless there is a significant amount of dispersion,for GVD alone this is typically around 45000 fs^2 [11].

LC SLMs are very convenient as they allow full electrical control over spectral phase and amplitude content. The SLM is stable and can be held in a constant state and does not require continual signal updates, apart from being driven at a constant-amplitude alternating current voltage signal (the molecular orientation is voltage sign invariant) to prevent migration effects within the LC [69]. The SLMs described in this section are one-dimensional arrays and are frequently used for pulse shaping purposes. LC SLMs are also available as two-dimensional arrays and can also be used for pulse shaping purposes, however this is discussed in more detail in chapter 5.

2.4 Measurement of pulse duration and dispersion: established methods

Since any pulse duration measurement requires use of optics, a method for completely characterising an optical pulse is required wherein those optics are taken into account during that measurement. The dispersion introduced by optical elements is well established theoretically [13]. However experimentally it is necessary to measure the dispersion in an optical setup as it is usually impractical to theoretically calculate dispersion in a given setup. This is especially important as some optical elements such as microscope objectives do not have manufacturer data included and so a theoretical calculation is unavailable. Complete pulse characterisation is a non-trivial problem owing to the fact that optical events are among the shortest known processes. Therefore to characterise an event in time, one requires a shorter event in time, however there are no known controllable events which are shorter than the typical times for ultrashort pulses (sub-picosecond). Electronics cannot be used to characterise sub-picosecond pulses, therefore we have to resort to using the pulses themselves to characterise themselves [46]. For brevity, more detailed discussions of the techniques of autocorrelation, FROG and SPIDER are presented in the appendix of this thesis.

2.5 Multiphoton intrapulse interference phase scan (MIIPS)

So far the mainstream methods of dispersion measurement have been considered. This section concerns the measurement and compensation system which was used in experiments requiring dispersion compensation. This system is a commercial product produced by Biophotonic Solutions Inc. and used multiphoton intrapulse interference phase scan technology, otherwise known as MIIPS^{TM}. There are two aspects to the MIIPS technology. Firstly, the dispersion of an optical system is measured using multiphoton intrapulse interference (MII) in SHG spectral measurements (i.e. with a spectrometer), while the phase scan operates in conjunction with a liquid crystal based SLM, which modulates amplitude and/or phase of the spectral components of the beam to effect a change in the MII. Once the dispersion has been measured, the SLM appropriately modulates the spectral components according to the iterative solution provided by the software, thereby removing the spectral phase introduced by the optics [76]. MIIPS is a single-beam method which makes it ideally suited to applications where the phase may need to be found for different experiments such as in microscopy [76]. The phase is inferred from the scanned phase modulation applied on the pulse which directly affects the probability of SHG at specific frequencies [77].

MIIPS Procedure

MIIPS takes some known reference function $f(\omega)$ and uses this function to cancel the unknown spectral phase of the pulse, $\varphi(\omega)$ [78]. The total phase for the pulse is then given by $\varphi(\omega) = f(\omega) + \phi(\omega)$. The second harmonic spectrum is then used to calculate the form of the unknown phase function, $\varphi(\omega)$. The generated second harmonic intensity can be written as a function of phase and spectral electric field amplitude [78]

$$S^{(2)}(2\omega) \propto \left| \int |E(\omega+\Omega)||E(\omega-\Omega)| \exp\left(i[\varphi(\omega+\Omega)+\varphi(\omega-\Omega)]\right) d\Omega \right|^2, \tag{2.3}$$

where $\varphi(\omega \pm \Omega)$ and $E(\omega \pm \Omega)$ describes the spectral phase and electric field at any frequency, respectively, and where Ω is any frequency used as a dummy variable during the integration procedure (Ω is hereafter referred to as the detuning frequency). Transform limited pulses have $\varphi = 0$ and thus generate the maximum second harmonic intensity. If the phase modulation produced by any physical process is continuous in nature, then we can expand the phase with a Taylor expansion about ω with the sum of the positive and

negative detuning frequencies being

$$\varphi(\omega+\Omega)+\varphi(\omega-\Omega)=2\varphi(\omega)+\varphi''(\omega)\Omega^2+\cdots+\frac{2}{(2n)!}\varphi^{2n'}(\omega)\Omega^{2n} \tag{2.4}$$

where $\varphi^{n'}\omega = d^n\varphi(\omega)/d\omega^n$. To the first order the SHG is maximised when $\varphi = 0$ and $\varphi''(\omega)$ is zero so that $\varphi(\omega) = f(\omega) + \phi(\omega) \to 0$. So as long as the second harmonic is maximised with the reference frequency $f''(\omega)$, then $\phi''(\omega)$ can be retrieved [78]. The MIIPS procedure is now discussed in more detail [78].

The MIIPS software performs a phase-sweep δ running from 0 to 4π and iteratively calculating the spectral phase accordingly. By measuring the SHG spectral signal as function of δ we obtain a function $f(\delta, 2\omega)$, with which a two-dimensional map of the spectral phase is obtained. Noting the sensitivity of SHG according to the spectral phase, the spectral signal provides information regarding the unknown spectral phase. The maximum intensity of the SHG spectrum is achieved when the second-order spectral phase term is given by

$$\phi''(\omega) = -f(\delta,\omega), \tag{2.5}$$

where $f(\delta,\omega)$ describes the two-dimensional map of the spectral SHG signal. The phase, $\phi(\omega)$ is obtained through direct double-integration of $\phi''(\omega)$. A starting point in MIIPS is obtained by using a known reference function, $f(\delta,\omega)$, with a double integration procedure. Typically a sine function is used,

$$f(\delta,\omega) = \alpha\sin(\gamma_\omega\omega-\delta), \tag{2.6}$$

where α and γ_ω are constants defining the amplitude and periodicity of the applied MIIPS function. During the MIIPS procedure the SHG plot, $f(\delta, 2\omega)$ is used to find $\delta(\omega)$ for each frequency. For each frequency, $\delta^0(\omega)$ is found through use of the analytic equation,

$$\phi''(\omega) = \alpha\gamma^2\sin\left[\gamma_\omega\omega-\delta^0(\omega)\right], \tag{2.7}$$

where γ_ω is a constant, generally being the inverse of the pulse duration. Once obtained after double-integration, the first phase term in the compensation is $-\phi_1(\omega)$, which is added to the phase in-use in the pulse shaper. Subsequent phase terms can be obtained thus, $\phi_{\text{total}} = \phi_1 + \phi_2 + \phi_3 + \cdots$. These additional phase terms decrease in magnitude with repeated iterations until a solution is converged towards. The obtained spectral phase is then implemented in the pulse shaper to obtain net zero spectral phase in the detection plane. Generally, six iterations are required for optimum phase minimisation.

Practical details about the MIIPS procedure for obtaining near transform-limited pulses are included in the experimental procedure section below.

Implementation of the MIIPS system

MIIPS has been implemented in several compensation schemes in addition to laser pulse compression with a high success rate. MIIPS lends itself for compensation schemes involving high dispersion optics, such as microscope objectives. So in principle any experiment which requires the passage of a single ultrashort pulse laser beam through an objective can benefit from the highest peak power transform limited pulses. Furthermore the pulse shaper can be made to fashion pulses which excite multiple chemical processes by selective excitation [79, 80]. Control of photo-sensitive chemical reactions [81, 82] can be achieved using femtosecond pulses using binary phase pulse shaping methods [83]. Binary phase modulation works on the principle that to maximise or minimise certain pathways we need only to adjust the phase between two values: 0 and π between each frequency component [84].

Much work has been done to identify chemicals accurately. Mass spectrometry is a well known technique for identifying chemicals but lacks the ability to differentiate between isomers, such as o-xylene and p-xylene [85]. Ultrashort laser pulses shaped using MIIPS have been used to control molecular fragmentation in combination with mass spectrometry to achieve high sensitive molecular identification [85,86]. The ultimate goal is to suppress a certain molecular fragmentation path while increasing the probability that the desired fragmentation type will occur; as yet this goal has not been achieved because coherence appears to play a limited role in defining fragmentation pathways [87]. Atomic emissions measured in laser induced breakdown spectroscopy were found to be more efficient using femtosecond pulses that have a very large bandwidth and with pulses exhibiting positive linear chirp, as can be achieved using MIIPS [88].

The MIIPS system has also been used for measuring the spectral phase of ultrabroadband ultrashort pulses, indeed such as that of a 2.12 GHz repetition rate Ti-Sapphire laser compressed using dispersion compensating mirrors and compensated for using MIIPS [89]. This same laser system was used to transmit encrypted information, but was limited by the slow response speed of the SLM [90]. An octave-spanning laser with ultrabroad bandwidth pulses (400nm) has been demonstrated with a grating based shaper in conjunction with MIIPS to generate a second harmonic spectrum spanning 200 nm [91]. Dispersion measurements of various media using a MIIPS-compensated laser is possible and relatively simple due to only needing a single-beam to take the measurements. Ex-

amples include group velocity dispersion measurements of water, seawater and ocular components [92]. Remote dispersion measurement has also proven possible at a distance of 28.9 m with amplified pulses [93] where the GVD of air at 800 nm was measured to be 20.1 ± 1.5 fs^2/m.

Applications of MIIPS also extend to Raman and coherent anti-Stokes Raman scattering (CARS) spectroscopy using the high peak power to enhance the signal strength. The amount of Raman scattered light is very low when using CW lasers, so signal-to-noise ratio is relatively poor, although methods using frequency modulation complement this method [94]. Higher intensity lasers will cause more Raman transitions to occur and hence more signal will be produced; providing the background signal can be suppressed then the Raman scattered light may be detected. Stand-off detection of several chemicals using CARS at a distance of 12 m has been demonstrated using MIIPS compensated pulses [95, 96]. A similar level of detection has been achieved using a pulse compressor but instead of suppressing the background as in the MIIPS system, the background is coherently interfered with the weak resonant signals [97]. Obvious applications include hazardous material detection such as biological and chemical agents and explosive detection. The ability to arbitrarily compensate for dispersion in optics using MIIPS allows microscope objectives to be incorporated into experiments involving ultrashort pulses. The biggest barrier to doing so is due to the dispersive optics that microscope objectives typically contain, particularly so for high numerical aperture objectives comprising substantial lengths of glass or other refractive materials. The development of dispersion compensation techniques maximises the benefits of using ultrashort pulses, in which the signal intensity can be order of magnitudes higher [98]. In systems using dispersion pre-compensation instead of active compensation is possible but require knowledge of the dispersion properties of the objective concerned [99]. The second order dispersion characteristics of various high-NA objectives were measured in [99] and were found to be in the range of 580 to 1100 fs^2. Other literature has pointed towards a second order dispersion range of 4600 to 5400 fs^2 for similar objective types [100]. Technical difficulties are presented in pre-compensation systems such as prism-based systems due to significant higher order dispersion, which means that the numerical aperture must be kept low for sub 10 fs pulses [78]. With the problem of dispersion all but eliminated, we can take advantage of the high peak powers afforded by ultrashort laser pulses and initiate nonlinear processes at the focus of the objective. Since the time-averaged efficiency of second harmonic generation is proportional to the peak intensity of the light, it makes sense to take advantage of such properties. Hence imaging using the second harmonic signal has been demonstrated along with selective fluorescent excitation using the MIIPS system [81, 98]. The advantages of using the second

harmonic signal are clear such as increased depth penetration, reduced photobleaching as lower average power is needed. Selective imaging is demonstrated using the same laser in which the excitation wavelength can be chosen by shaping the laser pulse such that the two-photon absorption at two different wavelengths can be achieved using the same pulse and thus observing the fluorescence signal from specifically marked structures inside cells [81]. Coherent control of the laser pulse can be used for functional imaging, in which selective two-photon excitation is achieved in a pH-sensitive chromophore, which is placed behind a highly scattering biological tissue [101]. This suggests that pulse shaping methods may have benefits for imaging and photo-dynamic therapy while minimising damage to healthy biological tissue.

It should be noted that while the MIIPS system can accurately measure and correct for dispersion in microscope-based systems, the choice of optics can have a profound effect on the operation of the MIIPS system. In particular, optical fibres introduce significant problems and may not be easily compensated using the MIIPS system. The MIIPS system permits pixel wrapping on the SLM to provide an appropriate phase relationship between neighbouring pixels. At the phase equals 2π boundary, the phase may be equivalently represent by 0 instead, and hence permits phase wrapping. Generally, a sequence of least four adjacent pixels is required to permit one phase wrap of 2π in order to prevent significant error in the applied spectral phase [78]. However, depending on the pixel resolution of the SLM, this condition may become further constrained and require additional pixels to maintain accurate phase wrapping.

2.6 Operation of MIIPS system

The MIIPS system requires careful alignment an operation to achieve the best results. The purpose of this section is to detail the manner in which to achieve the best results using the MIIPS system. In an inverted microscope arrangement a specially adapted (commercially-supplied) SHG detection module referred to as MIIPS detection unit (MDU, described below) was used. An alternative MDU is obtainable for an upright microscope. For each type the MDU is configured to be easily rotatable (for angular phase-matching) and optimised for overall stability in the desired microscope type. The MDU comprised a 100 μm thick Potassium Dihydrogen Phosphate (KDP) Type I crystal configured to be situated at the focus of a lens and optics for directing SHG signal down a fibre into a spectrometer (described below). The MIIPS system was also adapted for use in an upright microscope setup and also in free-space optics arrangement, but the MDU was not well suited to these applications. The MDU allowed for the most efficient collection of SHG

signal compared with other free-space optics detection configurations. It should be noted that a Beta Barium Borate (BBO) Type I crystal of similar thickness was used in the free-space optics experiments.

2.6.1 MIIPS experimental procedure

Here, the procedure for setting up the MIIPS system is detailed. It is perfectly reasonable to use either achromat or singlet lenses however achromats were found to offer optimal performance. Furthermore, dispersion-free focussing mirrors can be used in place of lenses, however this option is more expensive and the MIIPS system adequately deals with dispersion in the entire optical system.

(i) The femtosecond laser system was running stably and modelocked before being directed into the MIIPS pulse shaper. Spectral components were angularly dispersed within the pulse shaper and were focussed into the spatial light modulator (SLM) with the laser power distributed over a wide spatial region. If the laser was running in CW mode, the power would be focussed into a narrow spatial location on the SLM, potentially resulting in damage. If the laser switched to CW mode the beam was immediately blocked from entering the pulse shaper.

(ii) The beam was well collimated and expanded to around 3-5 mm in diameter using a telescope and directed into the pulse shaper in the horizontal polarisation for maximum pulse shaper transmission efficiency. The beam was aligned through two alignment apertures (the second aperture to be removed after alignment). If the beam is too small the grating will not be efficiently utilised and individual spectral components will disperse over a wider angular range resulting in spectral phase error, whereas if the beam is too large it will be blocked by pulse shaper components.

(iii) The beam was then aligned through the pulse shaper. In general if the pulse shaper is pre-aligned then not much work is required apart from adjusting the focussing mirror and the second mirror so that the two beams on grating are vertically displaced with respect to one another by approximately 5-6 mm, but with no horizontal displacement. The beam should then exit the final aperture with no evidence of any diffractive effects (generally) caused by the beam passing too near the first mirror. Figure 2.5 shows a simplified illustration of the MIIPS pulse shaper arrangement for reference purposes. The pulse shaper design can be adapted in a number of ways including changing the grating to accommodate different spectral bandwidths.

(iv) The beam which exits the pulse shaper was appropriately directed into the experimental setup (e.g. microscope). Spectral SHG measurements should be taken at the

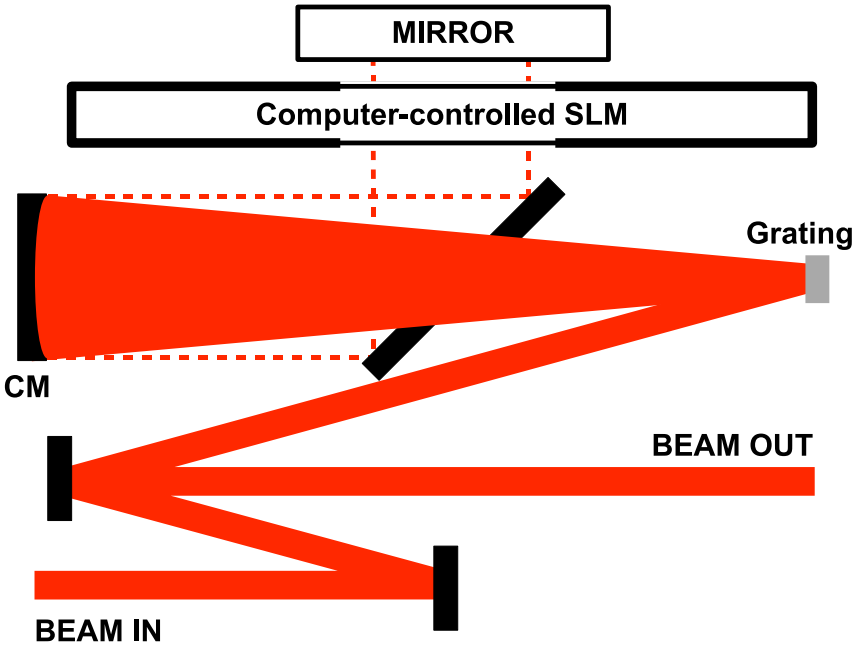

Figure 2.5: Simplified illustration of MIIPS pulse shaper setup depicting a typical arrangement. The arrangement may be adapted to accommodate laser parameter changes. CM is a concave mirror configured one focal length away from the grating and one focal length away from the mirror behind the SLM (hereafter referred to as the back mirror). The SLM admits the beam as shown through the SLM pixels (not shown directly, but indicated by the decreased line width of the SLM box). The concave mirror images the grating onto the back mirror and back again, thereby passing the beam through the SLM twice. The grating angularly spreads spectral components of the beam on the first beam pass and then recombines them on the second beam pass. The components of pulse shaper are angled such that the beam is displaced in terms of height so that the beam is directed towards an output upon return from the pulse shaper.

point at which transform-limited pulses are required. As SHG generally requires a certain amount of beam focussing to obtain high intensities, the MIIPS procedure cannot be performed directly on collimated beams. Instead, focussing mirrors can be used, although in practice this method is not ideal due to the aberrations introduced.

(v) The MDU (or other SHG collection optics) was placed appropriately at the beam focus and the SHG signal obtained. The MDU should then be rotated to obtain maximum SHG signal through optimal phase matching. In this part of the setup it was necessary

to block the fundamental beam using a UV-VIS short-pass filter to allow only the SHG signal through. The SHG signal was focussed into a fibre spectrometer (USB2000, Ocean Optics) for spectral measurements.

(vi) A scattering medium (white card) was placed inside the MDU, the short-pass filter was removed and the fundamental spectrum was measured. At this point the wavelength calibration was performed. To do this a transmission modulation was applied to individual pixels (typically pixel numbers 219, 269, 319, 369, 419 and 469). The centre pixel (319) was co-aligned with the centre wavelength of the spectrum by adjusting the grating (G1) to horizontally shift the spectrum relative to the pixels. The spectrum was vertically shifted to the central position within the SLM aperture, and finely adjusted to ensure that there was no amplitude modulation. The values of wavelengths were recorded for each of the pixel numbers and entered into the wavelength calibration of the MIIPS software.

(vii) The SLM operates by modulating the phase of each pixel within each array of the SLM by applying a voltage. Therefore it was necessary to calibrate the pixel phase voltage dependence. This was performed by running the SLM calibration software. It is highly important to accurately calibrate the phase as the MIIPS software relies upon accurate phase application to perform dispersion measurements. Importantly, the temperature should be held constant as the liquid crystal pixels are strongly affected by changes in environmental conditions. In all cases the room temperature was held constant at 23 Celsius.

(viii) To perform a MIIPS measurement and compensation, firstly the phase and transmission masks were cleared (phase = 0, transmission = 1). The fundamental spectrum was measured and recorded. Then the SHG signal was maximised and utilised by the MIIPS program while performing its iterations. This step was repeated until remaining spectral phase was ideally less than 0.5 radians across all wavelengths. The software automatically applied the negative values of the obtained spectral phase in order to deliver nearly transform-limited pulses in the focal plane. Once the SHG module was aligned the MIIPS measurement took 1 minute for a coarse measurement, or 6 minutes for a fine measurement. For all measurements the fine measurement was undertaken due to slightly less error being reporting during these measurements. However, in some measurements the using the coarse mode, the error was as small as when using the fine mode. In more up-to-date versions of the software quicker measurements are possible, however for system stability we chose not to upgrade.

(ix) Additional considerations include the need to optimise the SHG signal for any given situation. Firstly, the SHG signal should be adjusted to lie within the detection range of the spectrometer; specifically, when compensated the SHG signal should not

saturate the detector of the spectrometer. Secondly, the dispersion-compensated SHG spectrum should ideally be a smooth shape (Gaussian SHG spectrum if using a Gaussian fundamental spectrum). However, if the fundamental spectrum is asymmetric or has any uneven features, then these affect the SHG spectrum if residual chirp remains or is added to the optical system. For example, if compensating and subsequently stretching the pulse by adding dispersion then the SHG spectrum may no longer have smooth features.

2.6.2 Pulse stretching

Two methods were used to stretch the pulses. Firstly, the MIIPS software provided a platform to apply arbitrary phase and/or transmission functions on top of the obtained dispersion profile. Most relevantly the pulses were stretched by applying a second order polynomial function, with the resultant pulse duration calculated using the MATLAB program in the supplementary CD and acknowledged in Appendix 7.5. It should be noted that the fundamental spectrum is modified by the phase compensation function, especially when the applied function requires multiple phase wrapping. However, when adding additional (second order) phase functions this did not yield a substantial change in the fundamental spectrum. Secondly, anti-reflection coated optical flats made of BK7 glass were inserted into the setup. These were found to contribute mainly second order dispersion, with negligible third order dispersion and no measured loss in transmission, even when multiple flats were inserted. Fig. 2.6 shows the SHG spectra for several pulse durations obtained with the two methods. The overall shape of the spectra were comparable however the total signal differed slightly. This was due to the change in fundamental spectral intensity which occurs when an additional phase function was applied on top of the compensation function, in particular where the compensation function was negative in sign and the addition of positive GVD decreased phase wrapping and increased the fundamental intensity. For this reason optical flats were chosen for all experiments as they did not alter fundamental spectral intensity.

2.7 MIIPS results

2.7.1 SHG as function of pulse energy and duration

It is expected that the SHG intensity follows an exact relationship for any pulse energy and duration. In the case of the instantaneous SHG intensity this is given by

$$I_{\mathrm{SHG}} \propto I_{\mathrm{fund}}^2 \propto \left(\frac{W_{\mathrm{p}}}{\tau_p}\right)^2, \tag{2.8}$$

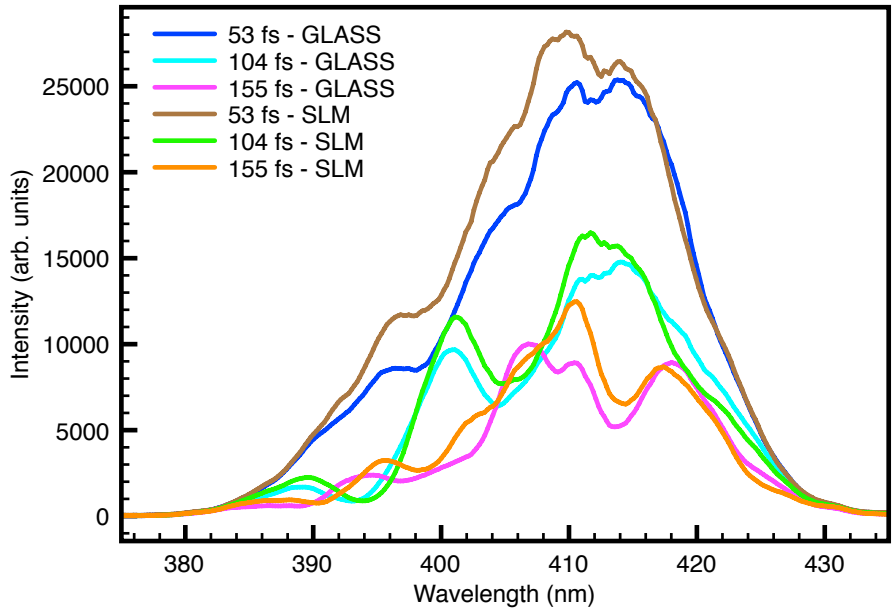

Figure 2.6: Comparison of SHG spectra from the two pulse stretching methods for several pulse durations. Note the trend of the SHG spectrum shifted towards longer wavelengths for greater chirp occurs due to the asymmetric fundamental pulse spectrum shape; it would not shift in this way for a symmetrical spectrum. The expected SHG shift can be calculated from equation 2.3

where I_{fund} is the fundamental intensity and W_{p} is the pulse energy. However, an instantaneous measurement of SHG intensity is not possible and therefore the signal is averaged out over a sequence of pulses of duration τ_p, with the following relationship

$$\langle I_{\text{SHG}} \rangle \propto \left(\frac{W_{\text{p}}^2}{\tau_p} \right), \tag{2.9}$$

where $\langle I_{\text{SHG}} \rangle$ denotes the time-averaged SHG intensity. Fig. 2.7 shows the total SHG signal for given pulse energies on a log-log scale. The obtained gradient was 1.89 ± 0.05 indicating $I_{\text{SHG}} \propto W_{\text{p}}^{1.89}$. This is reasonably close to the expected gradient of 2. Note that the error bars are provided but are insignificant in size. The spectral SHG intensity follows an inverse reciprocal relationship with pulse duration. Fig. 2.8 shows a log-log graph of the SHG data for a set of pulse durations with the fundamental spectrum from the Femtolaser oscillator. The gradient of the fit indicates that above 33 fs the $1/\tau_p$ relationship follows almost exactly with a small deviation of $1/\tau_p^{0.97}$. Clearly, below 33 fs the relationship

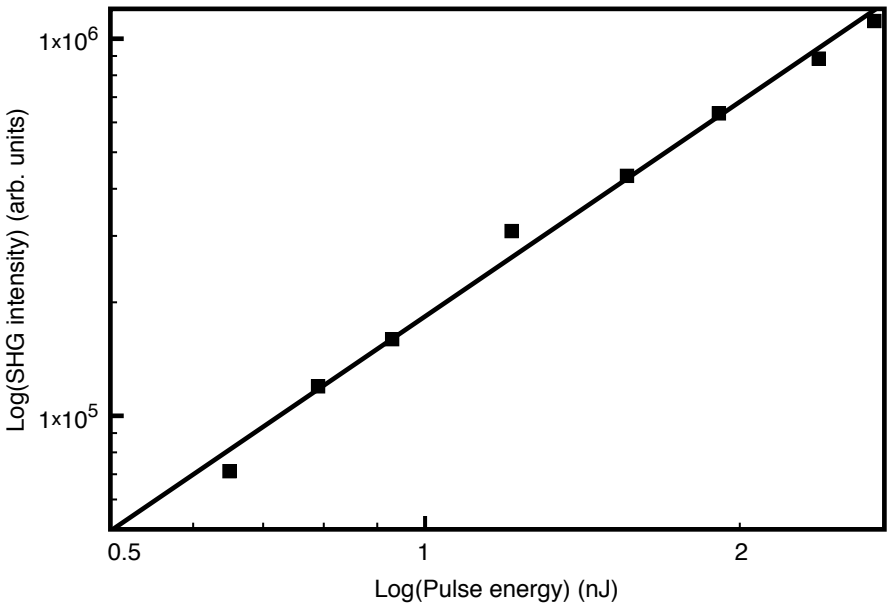

Figure 2.7: The integrated spectral SHG data for a set of pulse energies on a log-log scale.

breaks down with a linear fit over the entire pulse duration range corresponding to $1/\tau_p^{0.74}$. This deviation from theory was observed every time, and the behaviour was repeated when two different fs lasers were used. The KM Labs laser had a slightly narrower bandwidth with a minimum pulse duration of 16-17 fs. In an identical similar experiment with the KM Labs laser we found the relationship to follow $1/\tau_p^{0.91}$ indicating that at or near 12 fs there is a significant deviation from theory. Following on from this the spectral data accompanying this data is presented in the top panel in Fig. 2.9. The spectral SHG signal is strongly dependent upon the spectral phase relationship according to equation 2.3. The bottom panel of FIg. 2.9 shows the theoretical SHG spectral signal, as calculated through equation 2.3. The MATLAB code used to generate the data in the plot is provided in the supplementary CD and acknowledged in Appendix 7.5. The theoretical data sets have been normalised with respect to the 33 fs experimental data set so an easy comparison can be made. Fig. 2.8 demonstrated that above 33 fs the spectral signal closely followed theoretical predictions, hence the choice for normalising with respect to this data set. Clearly the 12 fs data set does not produce as much SHG signal as expected. However, above 33 fs the SHG signal more closely matches the theoretical values, and the spectral oscillations for longer pulse durations are also predicted by the model. Importantly, the SHG spectra are narrower than expected. There are a number of possible explanations,

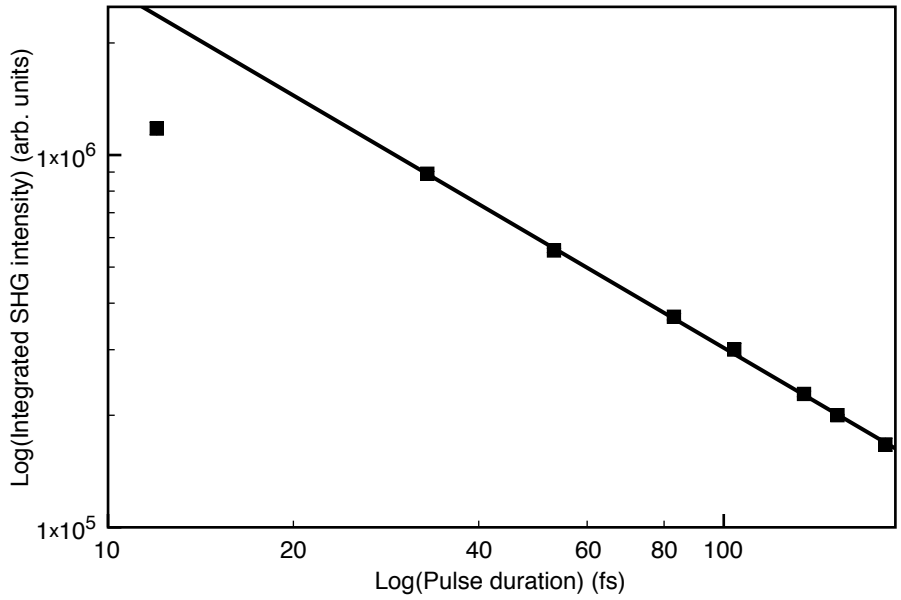

Figure 2.8: The integrated spectral SHG data for various pulse durations plotted on log-log scale. The linear fit shown was calculated for the data down to 33 fs. The deviation of the 12 fs data point from this fit indicates a discrepancy in the SHG model.

not limited to:

(i) The SHG crystal does not offer a uniform conversion efficiency across the spectral bandwidth. For example, this could be due to imperfect phase-matching. Despite our best efforts we could not obtain a broader SHG signal through changing crystal angles.

(ii) The focussing behaviour of the beam is strongly influenced by the spatial and spectral/temporal characteristics of the beam. There are a number of possibilities in this category. For example, chromatic aberrations lead to a non-uniform spatial spectral spread at the beam focus. Also, spectral phase can influence the spatial beam characteristics through spatio-temporal couplings [102]. Hence, the focal spot size (and peak intensity) could be influenced by the spectral phase.

(iii) The MIIPS method does not offer perfect spectral phase correction. In particular, the MIIPS system cannot deal with (transverse) spatially-dependent spectral phase. The MIIPS measurements provide a spectral phase correction error value. This aspect is discussed further in chapter 5. Furthermore, it was not possible to make an exact comparison between MIIPS-obtained spectral phase and other pulse measurement techniques, although MIIPS has been found to be comparable with other techniques such as FROG

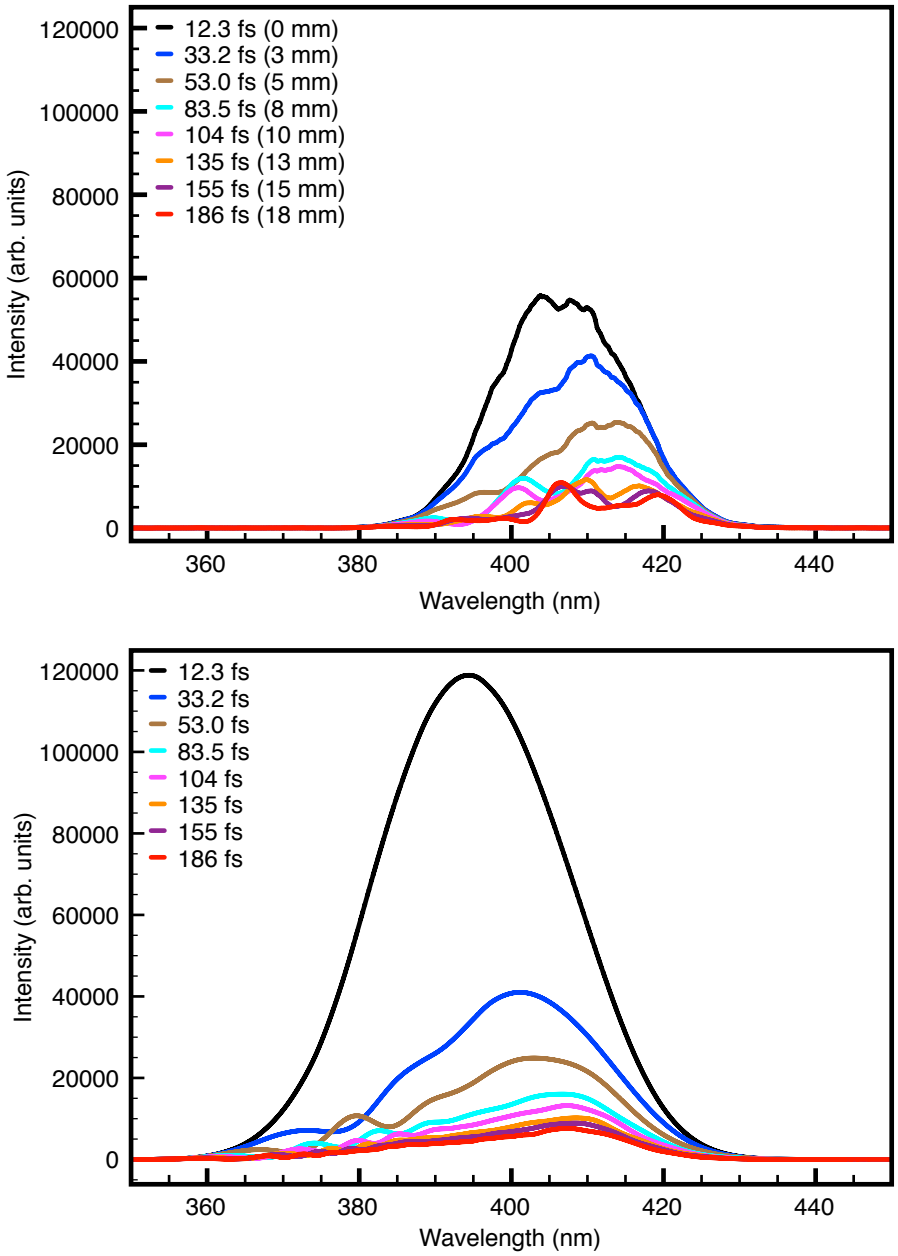

Figure 2.9: Top: Experimental spectral SHG data for different pulse durations obtained by inserting anti-reflection coated optical flats into the beam path. Bottom: Theoretical SHG spectra obtained for the same fundamental spectrum used in the experiments. The theoretical data was calculated using equation 2.3.

and SPIDER [78]. In particular, the spectral phase measurement of all three techniques were comparable in measuring the pulse duration, thereby establishing MIIPS within the field as a comparable dispersion compensation technique.

2.8 Conclusions

This chapter built upon some of the principles of ultrashort pulses outlined in chapter 1. In particular, dispersion is known to be of paramount importance in ultrashort pulse propagation through dispersive optical systems. This chapter discusses dispersion compensation in more detail and considers the well known dispersion compensation methods such as prisms and gratings. A further development in dispersion compensation came in the form of pulse shaping in so-called 4-f pulse shapers. Programmable pulse shapers provide the ability to controllably modulate spectral phase and amplitude, hence changing the time-domain characteristics of an ultrashort pulse. Pulse shaping provides suitable means for obtaining unlimited ultrashort pulse shapes. This ability to control pulse shape allows the user to adjust the pulse duration according to the experimental requirements. However, broadband ultrashort pulses suffer from significant dispersion and hence pulse shapers provide the opportunity for dispersion compensation to achieve pulse duration minimisation *in situ*. We used a commercially-available pulse shaping system known as MIIPS, in which spectral SHG measurements are taken in sequence according to the modulating phase function within the pulse shaper. The MIIPS algorithm retrieves the spectral phase and uses this function to compensate for the dispersion in the optical setup from laser output coupler to the SHG crystal. We characterised the performance of the MIIPS system, particularly concentrating on obtaining optimum performance through careful and repeated calibration procedures. We further investigated the performance of the pulse shaper and found that for the shortest pulse durations the SHG signal obtained did not correlate with theoretical expectations. This issue is investigated in the beam shaping chapter 5. The ability to provide dispersion-compensated ultrashort pulses *in situ* is particularly desirable since dispersion at the shortest pulse durations is known to significantly stretch the pulse duration. This chapter therefore serves as a pre-requisite for subsequent chapters concerning studies involving ultrashort pulses. In the optical binding chapter we consider the effect of ultrashort pulses on the light-matter interaction between co-trapped dielectric spheres within an ultrashort pulse light field. We further investigated optical binding within SHG ultrashort pulse light fields, wherein the SHG spectral signal is particularly sensitive to spectral phase. In the optoinjection chapter we examined the linear and nonlinear absorption processes initiated by ultrashort pulses in cell membrane perme-

abilisation. In particular we investigated the role of pulse duration in this light-biomatter interaction process which is relevant for all biophotonics applications involving ultrashort pulse lasers. Finally, in chapter 5 we further advanced this study of pulse shaping in the time-domain to pulse shaping in the space-domain, wherein spatio-temporal couplings play a key role in defining ultrashort pulse beam propagation. This is relevant for any application of ultrashort pulses as it is possible to tailor pulses effectively in four dimensions to provide multiple possibilities in biophotonics, spectroscopy, pulse compression and the like.

2.9 Chapter acknowledgements

The author designed the MATLAB models in this chapter and performed related experiments.

Chapter 3

Transverse optical binding

3.1 Introduction

An important aspect of the light-matter interaction concerns the ability for light to manipulate objects, for example dielectric particles using optical tweezers. In this chapter I further expand on the relevance of ultrashort pulses in the domain of so-called optical binding in which scattered light between particles is found to bring about sufficient force to effect movement or restriction of said particles within some trapping medium such as water. In particular, we consider the role of broadband ultrashort pulses in terms of the force dependence between particles as function of separation and spectral bandwidth. The relevance of pulse shaping is considered in the section concerning SHG optical binding whereby, the phase-dependent SHG spectral bandwidth is affected by dispersion and results in decreased optical binding strength where dispersion is not sufficiently compensated for.

Optical tweezers are extremely powerful tools in the colloidal and biological sciences [103–105]. The term optical tweezer was coined to describe the ability to hold microscopic particles in space in a laser-created potential well deep enough to prevent Brownian fluctuations from knocking the particle out of the trap. The optically induced forces that result from the light-matter interaction are sufficient enough to control and manipulate microscopic, and even nano-sized particles. This is due to the change in momentum as photons are scattered and refracted through a particle (or instead owing to the electromagnetic field flux density as modified by the particle involved). The invention of the laser has allowed considerable progress in creating high intensity, highly directional beams which are associated with high a flux of photons, each carrying momentum of $\hbar k$.

Optical tweezers are widely used tools in, for example, microfluidics [106], measurement

of Raman signatures in trapped particles [107] and measurement of torque forces in flagellar optical motors [108], to name but a few applications. The term optical tweezers describes an optical tool configured to hold microscopic particles in 2D, or 3D space in a laser-created potential well deep enough to prevent Brownian fluctuations from knocking the particle out of the trap. The optically induced forces that result from the light-matter interaction are sufficient enough to control and manipulate microscopic, and even nano-sized particles. The origin of optical trapping forces for dielectric micro-particles can initially be decomposed into two classes. In the first class the radiation pressure exerted by scattered fields on particles is sufficient to move the particle by a measurable amount. In the second class the laser spatial profile is typically Gaussian and the particle is forced towards the highest intensity part of the beam provided the refractive index is higher in the particle than in the host medium. The trapping strength is enhanced by focussing the beam, in particular with a microscope objective the gradient force becomes much larger and enables particle trapping in all three dimensions against the effect of gravity and light scattering forces.

Twenty years ago, Burns *et al.* demonstrated that systems of free-floating microscopic dielectric particles may become optically bound under intense laser light [109]. An optical line trap was created using two crossed cylindrical lenses. The high intensity gradient achieved perpendicular to the long trap axis strongly confines any trapped particles in this direction, however parallel to the long trap axis the particles are less strongly confined. Hence the trapped particles may float freely along this axis and hence the system is effectively one-dimensional. Fig. 3.1 illustrates the relative differences between optical trapping and optical binding. Firstly, independent traps refer to optically trapped particles held in position by an optical tweezers indicated by the green circles. In independent trap 2 the particle is non-central indicating how particles actually fluctuate positionally around the centre of an optical trap. In optical binding there exists two or more co-trapped particles which are subject to the same optical (elliptical) trap, but scattered light acting between the co-trapped particles results in binding forces acting therebetween. The general direction of force within the elliptical beam focus is indicated by the appropriate arrows along with the relative polarisation directions. The symmetry of this situation means that each particle is equally illuminated. The interesting point demonstrated in the paper was the oscillatory nature of the optical binding forces, which were periodic in the wavelength of illuminating light in the host medium, water. In a later paper, Burns et al. demonstrated that arrays of extended crystalline and non-crystalline structures could be fashioned with correctly applied interfering laser beams [110].

To summarise, optical trapping refers to the phenomenon of using focussed laser beams

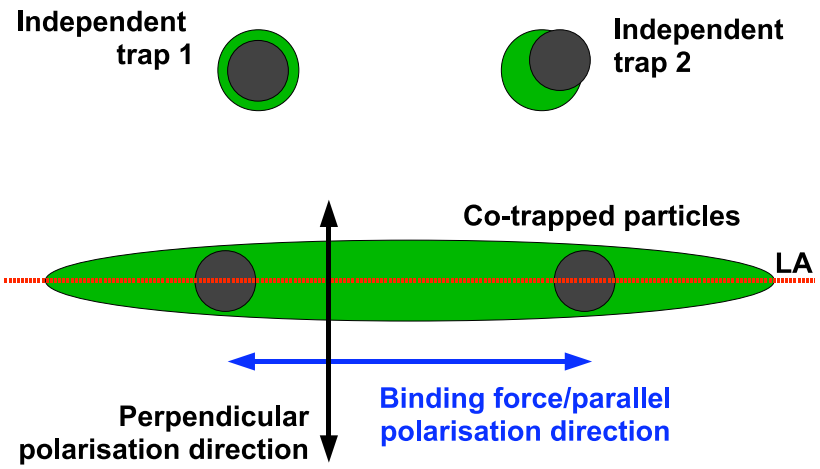

Figure 3.1: Illustration depicting the difference between independent trapping of two spheres using independent optical tweezers wherein independent trap 1 contains a particle that is centred with the highest intensity region of the trap; independent trap 2 contains a trapped particle that is oscillating about its centre position (due to Brownian motion). In the co-trapped particles example a line (elliptical) trap is formed such that two particles are confined within the same trap simultaneously while scattered light therebetween produces an additional *binding* force; the direction of said binding force within the focal plane defined by the (green) oval. LA represents the longitudinal axis of the beam focus. Importantly, the particles which are held in optical tweezers are subject to an equally-acting radial force due to symmetry considerations. The particles held in the elliptical trap are strongly confined in the vertical direction, but less strongly confined in the horizontal direction, along the longitudinal axis (LA).

to effect trapping of a particle through gradient and scatterring forces such that the particle will not readily escape. Optical binding refers to an inter-particle interaction between co-trapped particles.

3.2 Transversal Optical Binding

In transverse binding the scattered light from each co-trapped particle is mostly responsible for the inter-particle binding. External influences may further result in changes of the optical binding potential. For example, the substrate adjacent to the particles causes additional scattering and may result in modification of the optical trapping potential [111].

3.2.1 Rayleigh Regime

Optical binding between Rayleigh (particle diameter, d $\ll \lambda$) particles has been theoretically investigated [112] but experimentally this is difficult to execute because standard particle tracking methods are not possible for true Rayleigh particles due to low scattered signal intensity and most fundamentally, the limit imposed by optics principles that it is not possible to resolve the images of two objects separated by less than $0.61\lambda/\text{NA}$ [113]. The point-dipole model neatly explains the oscillatory nature of the force acting between the two particles. This approach is described in [109] whereby the interaction potential is given by

$$W = -\frac{1}{2}\alpha^2 E^2 k^2 \frac{cos(kr)}{r} \tag{3.1}$$

where α is the polarisability, E is the electric field amplitude and k is the wavevector of the light. An expression for the binding force can then found by differentiation of the potential energy with respect to r. This approach is inappropriate for Mie-sized particles, but does at least explain how the oscillations observed occur at integral values equal the illuminating wavelength in water. This model is discussed later in this chapter under the context of broadband ultrashort pulses.

3.2.2 Mie Regime

In the ray-optics regime (particle diameter, d $\gg \lambda$) we cannot accurately model particles in a tightly focussed beam but this approach has been attempted for single particle optical trapping [114]. Generally modelling the region between the ray-optics and Rayleigh regimes is difficult. The Mie regime is more difficult as approximations are usually unsuitable for the situation concerned. Many studies have been made into the Mie regime for single particles because analytical solutions exist and exact solutions can be found [113]. The situation with two Mie particles and a substrate is particularly difficult to analyse analytically because the substrate breaks any symmetry that one might consider. There has been some success for multiple Mie scatters, for example in calculating the Mie scattering for an arbitrary number of infinite length cylindrical particles of any diameter from an in-plane electromagnetic field [115] in which the force contributed by optical binding in a multiple particle system was found to depend on the number of particles involved. Owing to the lack of analytical solutions for multiple spherical particles adjacent to a flat substrate, a numerical computational method is required in order to converge towards a good solution and is discussed later in this report.

3.3 Longitudinal Optical Binding

In the transversal optical binding interaction the force acts between particles which are perpendicular to the propagation direction of the laser beam. This differs from longitudinal binding in which two counter-propagating laser beams bring about optical binding between the particles. Longitudinal binding has been demonstrated between two counter-opposing laser beams [116]. A first particle scatters the light, modifying the light field experienced by a second particle, and vice versa. A stable particle arrangement is obtained whereby the forces due to the incident laser light and the forces arising from the scattered light field balance equally. Any change in particle separation alters the force balance from the scattered light, which in turn changes the stable position of the particles.

Longitudinal binding appears similar to transverse binding but both are different in nature. In longitudinal binding the gradient force holds the particles in place along the beam axis, while the radiation pressure due to scattering determines the longitudinal position; the particles then refocus the light and along with the forward scattered light this allows stable longitudinal positions to be set up. Metzger *et al.* demonstrated a hysteresis effect when changing the separation of the fibres whereby the stable positions of the particles depending upon whether the fibres were approaching or retreating [116, 117]. This observation was due to the particles self-consistently modifying the scattered light fields, which in turn affected their position which they preferred to occupy. A femtosecond system has been developed for observing the binding process and scattered light intensity via two-photon fluorescence [118]. The longitudinal binding effect can be made to collapse under secondary illumination from two more counter-propagating laser beams [119].

3.4 Experimental procedure

Pilot experiments were carried out to establish the ideal protocol for performing the optical binding studies. Ideally, an optimum particle concentration in the host medium ensured sufficient particles were available for binding studies without potentially causing mechanical interference with particles of interest. The experiments were performed on an air-floated optical bench to minimise external vibrations. Sample preparation was conducted while underneath a protective hood with airflow designed to protect the sample from contaminants, for example, bacteria or dust. A solution of 1.8 micron diameter polystyrene particles were prepared with sterile water and sonicated to further clean the particles and to charge the particles up to prevent them sticking to the surface. The effect of charge on optical binding is negligible, see analysis below for more information. 20 μm

of the solution was extracted using a pipette and pipette tip sterilised by autoclaving and the solution placed inside a vinyl spacer placed on 22 by 50 mm BK7 glass substrate (0.15 $\pm$ 0.02 mm thick) and sealed with a cover slip of the same thickness and material but of dimensions 20 by 20 mm. The sample was then sealed using clear nail varnish. The glass substrates were previously cleaned by firstly applying a few drops of ethanol onto the surface and then dabbing clean using a lens tissue. Once dried the substrates were treated with a plasma cleaning gun to eliminate any remaining bacteria. Fresnel reflections within the optical setup were reduced using index-matching oil between the lower substrate surface and the objective. Anti-reflection coated slides were for the water-glass interface at 514 nm in order to reduce inner-sample reflections to prevent interference with the binding interaction. The slides were custom made by CVI-Melles Griot and had a reflectance of $<$0.25% on the water-glass side and $<$0.5% on the air-glass side of the slides.

The sample was placed into the experimental arrangement shown in Fig. 3.2 and irradiated with an Argon-ion laser (Spectra Physics) operating on the 514 nm spectral line as this provided the most power for a single wavelength. The microscope objective used was a Comar 60x/0.85NA achromat objective with a tube length of 150 mm and cover glass correction of 0.17 mm, which was appropriate for the cover glass thickness. Further, index-matching oil of refractive index 1.52 at 514 nm was used as this corresponded to the refractive index of the BK7 glass at this wavelength. .Two particles were located, irradiated and trapped by the elliptical laser beam and their positions directly tracked at 30 Hz scan rate using a program written in LABVIEW with an algorithm based on detection of the brightest spot across the particle cross-section [120]. In principle the particles could be scanned at a higher data rate but this is not necessary since the statistical variations do not largely manifest themselves for time intervals of less than 1/30 seconds. The statistical probability of the positions of the particles were used to calculate the binding potential based on the Boltzmann probability distribution $P(V_{\mathrm{tot}})$

$$P(V_{tot}) \propto \exp\left(-\frac{V_{tot}}{k_B T}\right) \tag{3.2}$$

The electrostatic interaction is zero in our experiments except for when the particles are nearly touching. The particles are confined in a one-dimensional system. If they are located at x_1 and x_2 then the system has a total potential energy given by

$$V_{tot} = V_{\text{line-trap}}(x_1) + V_{\text{line-trap}}(x_2) + V_{\text{el}}(|x_1 - x_2|) + V_{\text{opt-bind}}(|x_1 - x_2|) \tag{3.3}$$

where V_{el} is the electrostatic potential acting between the particles, $line - trap$ represents

the potential created by the line trap as seen by each particle located at x_1 and x_2, and opt-bind represents the optical binding interaction. $V_{\text{line-trap}}$ is correct near the centre of the line trap potential so is approximated by a parabola

$$V_{\text{line-trap}}(x) = bx^2, b > 0 \tag{3.4}$$

then the total potential energy separates in the centre-of-mass coordinates

$$V_{\text{total}} = V(R) + V(r) \tag{3.5}$$

using the expressions

$$R = \frac{1}{2}(x_1 + x_2), r = x_1 - x_2 \tag{3.6}$$

yields the following potentials in the separated coordinates

$$V(R) = 2bR^2 \tag{3.7}$$

and

$$V(r) = V_{el}(r) + V_{\text{opt-bind}}(r) + \frac{b}{2}r^2 \tag{3.8}$$

The data analysis is performed in ORIGIN. By calculating the value of $2b$ from evaluation of the centre-of-mass trajectory data using the above analysis, and using the fit parameter b in a plot of $-k_BT \ln P(V_{tot}) - (k_BTbr^2)/4$ versus r to find the form of the optical binding potential, $V_{\text{opt-bind}}$. Computation of the force requires a function to be fitted to the experimental data and differentiated with respect to r. In addition to the experiments with monochromatic laser beams we attempted to use a supercontinuum source Fianium: 4 ps pulse duration, 10 MHz repetition rate, 464-1750 nm spectral coverage, up to 6W average power, which has a broad bandwidth. Due to spatial overlap of spectral binding potentials we anticipated a lack of binding force oscillations. The powers required for oscillations to be observed were of the order of hundreds of mW for the monochromatic source. The supercontinuum source had a 6W output power, but only 1.3 W of this light was in the visible spectral region. After the required polarising beam splitters and optics, the power at the sample was not high enough for oscillations to be observed. Furthermore, particle tracking experiments were impossible to perform due to the requirement to image in transmission and simultaneously prevent laser power from saturating the camera. The solution of using a narrow bandwidth filter and corresponding illumination wavelength did not work. Furthermore, the sample was imaged in reflection, however the image was compromised by the presence of the cylindrical lens.

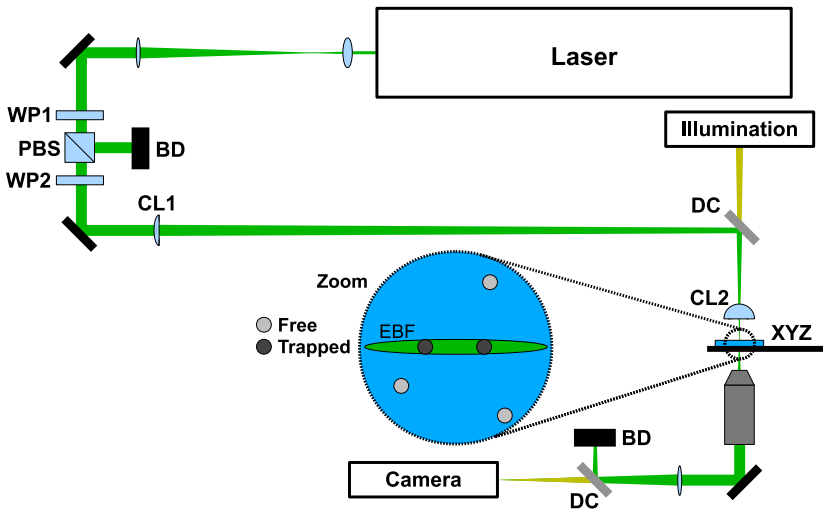

Figure 3.2: The experimental arrangement used for the optical binding setup, wherein particles trapped in the beam focus potentially undergo optical binding due to the inter-scattering fields subjecting mutual forces upon each trapped particle. The beam from an Argon-ion CW laser source operating on the 514 nm line was expanded and the power controlled using a rotatable half-waveplate (WP1) in conjunction with a polarising beam splitter (PBS) with remaining power dumped into a beam dump (BD). A second half-waveplate (WP2) was used to control the polarisation of the laser beam. A 50 cm cylindrical lens (CL1) focussed weakly in one direction and a 3 cm cylindrical lens (CL2) oriented perpendicular to the first lens focussed strongly in the perpendicular direction. The sample was held securely on an xyz stage (XYZ) and imaged using a Comar 60x/0.85NA objective and tube lens with index-matching oil (not shown) between the sample substrate and the objective. The beam power was attenuated by means of a dichroic mirror (DC), selective filter (not shown) and neutral density filters (not shown). Imaging was performed using a Basler Pilot PIA640-210GM camera and a 10 cm achromat lens for imaging thereon. The illumination was provided by a fibre linked to a halogen light bulb (Thorlabs high intensity fibre-coupled source).

3.5 Experimental results

Experiments were performed to examine the transverse optical binding interaction between two spherical particles having a diameter of 1.8 microns. A long-ranged interaction was observed for the perpendicular polarisation, with a comparatively short-ranged interaction for the parallel polarisation. The results from the optical binding experiments are shown below [121].

3.5.1 Experimental images

Figures 3.3 and 3.4 show intensity cross sections for the displayed particle separations with no external illumination (under laser illumination only). These images are provided to demonstrate the proximity of the particles and the relative separation under the microscope.

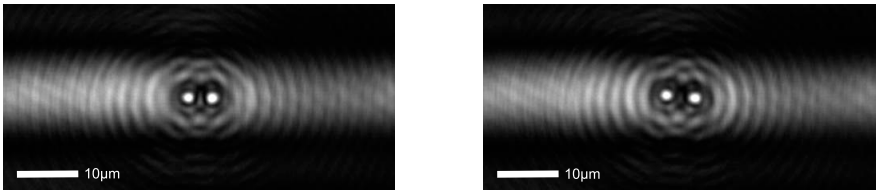

Figure 3.3: The panels show the field of view with the field intensity show for 5 λ (left panels) and 6 λ (right panels) separation.

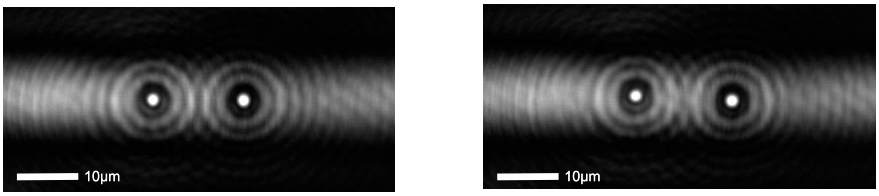

Figure 3.4: Top panels show the field of view with the field intensity show for 17 λ (left panels) and 18 λ (right panels) separation.

3.5.2 Optical binding potentials

The results of the optical binding potential are shown in figures 3.5 to 3.6 which show the potential well for the two particle system along with the centre-of-mass potential long axis of the beam trap. Note the distinct difference between the situation for the parallel polarisation and perpendicular polarisation. The optical binding interaction acts over a much longer range with light polarised perpendicular to the long trap axis. The periodic oscillations in wavelength are clearly visible in both cases and these oscillations continue for up to at least 15 wavelengths in the perpendicular case.

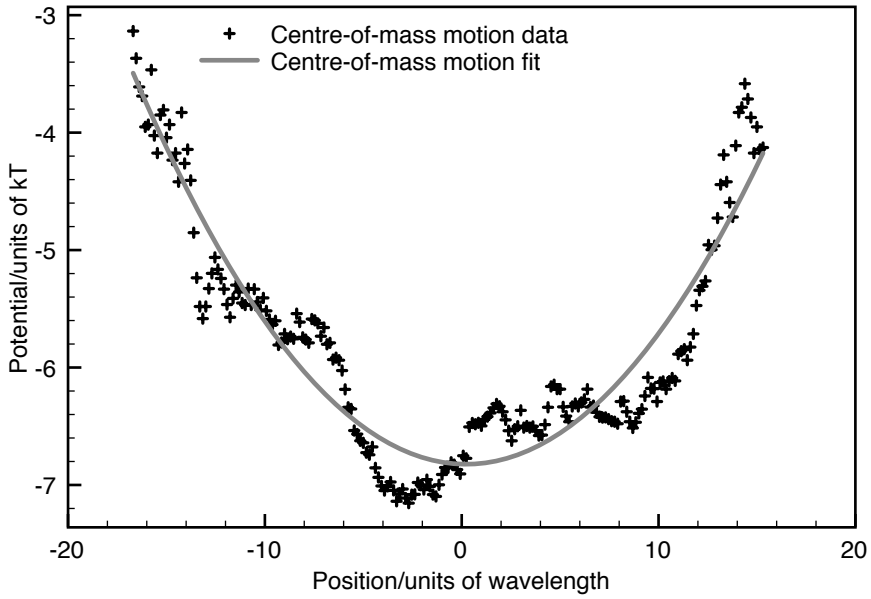

Figure 3.5: Example centre-of-mass potential for the perpendicular polarisation. Note the shape of the potential is quadratic bar some statistical fluctuations, which is ideal for the experiments as this suggests the particles are illuminated evenly. A similar potential was found for the parallel polarisation. It is expected that the centre-of-mass potentials would be identical as these relate to the incident field.

The binding potential differed for irradiation from perpendicular and parallel polarisations. For the case of the perpendicular polarisation the oscillations were extremely long ranged, and in fact increased in amplitude over increasing separation until about 10 λ, after which the oscillations decreased slightly. This demonstrates the long range nature of the forces arising from the scattered fields. The range of the optical binding for the parallel polarisation was smaller, and decreased in amplitude at greater rate. The binding force from the different polarisation had the oscillation peaks and troughs located at slightly different locations.

We have demonstrated the transversal optical binding when two polystyrene 1.8 micron diameter particles are irradiated by monochromatic light at 514 nm. Experimental results show that for the polarisation set perpendicular to the long axis of the trap the binding oscillations are extremely long ranged, indeed up to about 15 wavelengths, or about 5.8 microns. For the parallel polarisation the oscillations last for about 8 wavelengths, or about 3.1 microns.

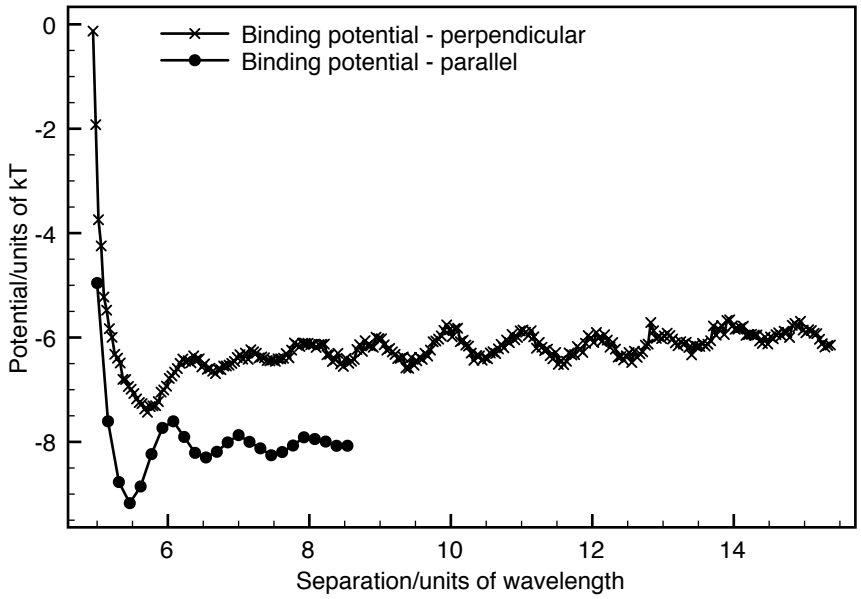

Figure 3.6: Optical binding potential as function of particle separation for the perpendicular and parallel polarisations. Note the long range of the binding potential for the perpendicular polarisation relative to the parallel polarisation. Data ended at 8.5 wavelengths for parallel example due to no further data collected

3.6 Computational study: finite element method

For the computational studies two different approaches were considered. Firstly, the finite element method was utilised to characterise the force acting between two co-particles of the same geometry of the aforementioned experiment. It was not possible to resolve aspects relating to the resolution of the individual elements in the model however indicative results of these computations are included. The situation is simplified by using Rayleigh-sized particles and utilising an interacting dipole method. The forces acting on Rayleigh-sized particles was calculated using the aforementioned method under monochromatic and broadband illumination. The methods of the Maxwell Stress Tensor and Surface force are discussed in Appendix 7.3.

3.6.1 Maxwell Stress Tensor and Surface Force

A number of methods can be used to calculate the force acting on and between optically bound particles. Our calculations of the binding force required two equivalent approaches,

namely the surface-force method and the Maxwell stress tensor method following numerical calculation of the electromagnetic field distribution using the finite element method program, COMSOL. The Maxwell stress tensor method is concerns the flux of momentum over the surface of the particles [122]. The surface-force method considers only the effect of the momentum flux over the surface as this is where the force manifests itself. These are equivalent methods because they start with the well known Lorentz force equation, which describes the force acting on a charge within an electric and magnetic field.

3.6.2 Computational results: finite element method

Here, results from the finite element method are shown. These preliminary results demonstrate some aspects of the oscillatory nature of the binding forces between two particles. These results are included to demonstrate an oscillatory binding force is expected. However, the model does not indicate a significant difference between the cases of the perpendicular and parallel cases, indicating further work is required. Figs. 3.7 and 3.8 show the binding forces for perpendicular and parallel polarisations, accordingly. Consistent

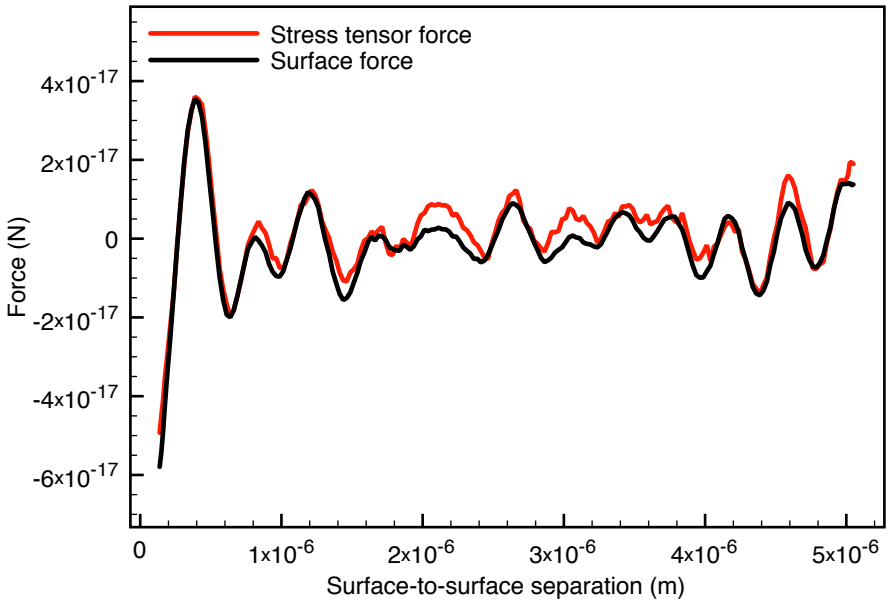

Figure 3.7: Binding force as function of particle surface-to-surface separation for the stress tensor and surface force methods illuminated by 500 mW plane waves in the perpendicular polarisation.

results were unobtainable due to complications potentially arising from element-mesh in-

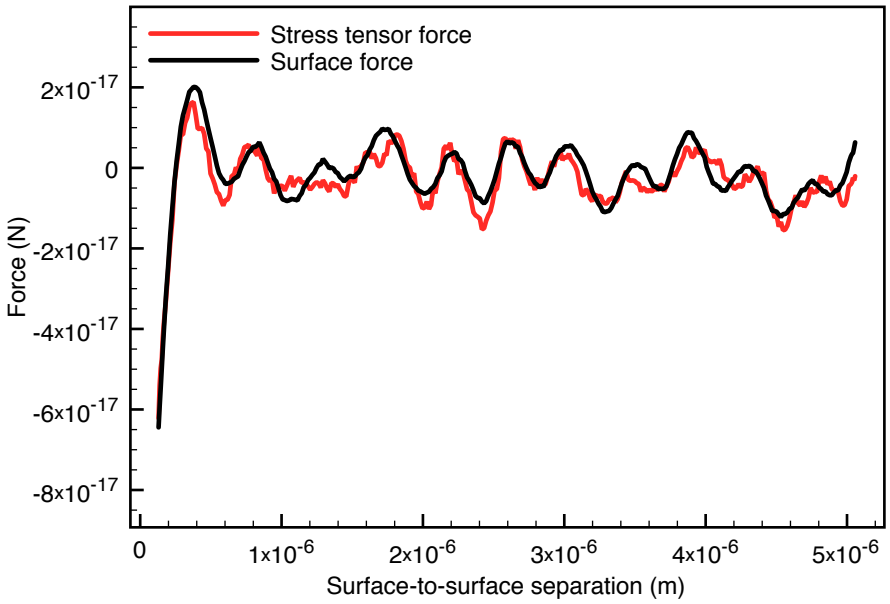

Figure 3.8: Binding force as function of particle surface-to-surface separation for the stress tensor and surface force methods illuminated by 500 mW plane waves in the parallel polarisation.

consistencies, particularly when particles were in close proximity. However in principle, infinitesimally small elements may improve results, however this is not to say that this alone would necessarily solve the problems with this model.

3.7 Computational study: interacting dipole method

In light of the results of the finite element models it is prudent to consider the case of a simple pair of interacting dipoles instead. In this situation the problem is simplified significantly, such that an analytical study is feasible due to the relative small size of the interacting dipoles relative to the illuminating wavelength. A model was developed involving an interacting dipole method to calculate the binding forces acting on at least a pair of Rayleigh-sized particles. Further, the model was implemented for broadband spectral content.

3.7.1 Optical binding: Rayleigh regime

The spatial periodicity associated with optical binding under monochromatic illumination is a well documented result of self-interaction due to scattered light affecting the potential landscape. Indeed, this was experimentally verified previously [109]. Naturally, it is anticipated that different wavelengths result in different optically trapping potential landscapes. Hence, where multiple wavelengths are present, each constituent wavelength will induce an associated potential landscape. If the spectral constituents are approximately similar in electric field magnitude then the potential landscapes may overlap, resulting in an overall blurred potential landscape, hence there will be reduced force oscillations [123]. The situation in which a single, broadband laser source has been considered previously. For example, the effect of supercontinuum generated light has been experimentally considered in longitudinal optical binding [124]. Theoretically, a broad spectral content has been shown to result in a blurred potential landscape between two optically bound Rayleigh-sized particles in the longitudinal configuration [125–127].

In our studies considered several situations were considered. Firstly, broadband light was considered, as typically generated by a Ti:Sapphire ultrashort pulse laser. In this first case, optical binding forces were considered [128] between two Rayleigh-sized dielectric particles, modeled as point dipoles. Further, multiple scattering events were incorporated into the calculations by considering the Clausius-Mossotti relation for the radiative reaction as a result of scattering [129]. Secondly, systems of greater than two particles were considered according to their reaction under plane wave illumination in the CW case. Finally, binding under illumination by ultrashort pulse SHG pulses was considered, as might be generated by a frequency-doubled Ti:Sapphire laser of the aforementioned specifications.

3.7.2 Theory

This section contains the theoretical background required to develop the interacting dipole model used for the simulating binding using broadband light. The MATHEMATICA code relating to the model is provided for the reader's interest in the supplementary along with appropriate acknowledgements in Appendix 7.5. In the model the following is considered. Firstly, a fundamental optical pulse centred at 800 nm interacts with at least a pair of dielectric particles having a diameter, for example, of 100 nm. Secondly a SHG pulse, as might be generated by the fundamental pulse is considered in the same situation. In each case a comparison can be made between the broadband (pulsed) case and the CW case.

In the model, a point dipole having a defined polarisation represents a corresponding

dielectric particle and is given by [130]

$$\mathbf{p_j} = \varepsilon_\mathbf{0} \alpha \mathbf{E}, \tag{3.9}$$

where p_j and E represent the j^{th} microscopic polarisation and electric field, respectively. While, ε_0 is the permittivity of free space. The macroscopic polarisability, α is provided by [130]

$$\alpha = 4\pi a^3 \frac{n^2 - 1}{n^2 + 2}, \tag{3.10}$$

where n is the index of refraction (relative to unity) and a is the assumed particle radius (note the polarisability of particles is calculated from the volume; however the model assumes these particles are point dipoles). The illuminating laser field observed by the point dipole is assumed to be constant due to the particle being sized in the Rayleigh regime. The field $\mathbf{E}'$, which is scattered by any j^{th} dipole can be described by [130]

$$\mathbf{E}' = \frac{e^{i\omega|\mathbf{r}|/c}}{4\pi\varepsilon_0} \left(\frac{\omega^2 (\mathbf{r} \times \mathbf{p_j}) \times \mathbf{r}}{c^2 |\mathbf{r}|^3} + \frac{(c - i\omega|\mathbf{r}|)\left(3(\mathbf{r} \cdot \mathbf{p_j})\mathbf{r} - |\mathbf{r}|^2 \mathbf{p_j}\right)}{c|\mathbf{r}|^5} \right), \tag{3.11}$$

wherein the constants c, ε_0 represent the speed of light and free space permittivity, respectively. The angular frequency is represented by its normal symbol, ω. A position vector, $\mathbf{r}$ is used to define a displaced position with respect to the corresponding position of the j^{th} dipole given by $\mathbf{r_j}$.

Equation (3.11) is unified by

$$\mathbf{E}' = \underline{\underline{M}}(\mathbf{r})\mathbf{E} \tag{3.12}$$

wherein $\underline{\underline{M}}$ is a second order tensor. The matrix, $\underline{\underline{M}}_{ij}$ describes the scattered electric field at the i^{th} position $\mathbf{r_i}$. This field comprises two parts. In the first part, $\mathbf{E} = \mathbf{E_j^0} + \mathbf{E_j}$, where $\mathbf{E_j^0}$ is the incident field. The second part, $\mathbf{E_j}$ corresponds to the scattered field that originates from all other dipoles, $\mathbf{r_j}$. Multiple scattering events can be considered by defining a self-consistent relationship, whereby all the fields are linked together through

$$\mathbf{E_i} = \sum_{j \neq i} \underline{\underline{M}}_{ij} (\mathbf{E_j^0} + \mathbf{E_j}). \tag{3.13}$$

Equation 3.13 comprises $3N$ equations with N unknown vector fields. The solution of this system of equations provides the the total scattered optical fields, whereby N dipoles may be subjected to an arbitrary incident field. Larger particles can be instead considered through the coupled dipole method [131], whereby the larger particles are treated as a

large set of self-interacting dipoles located at regular locations within a three dimensional array of dipoles which define the larger particle by their vector sum.

Ultrashort pulses which have broad spectral content can be treated by considering all contained spectral components within the pulse [132]. Accordingly, equations (3.11-3.13) are depend on the optical angular frequency. The resulting self-consistency relationship can be solved by taking each individual spectral component in its individuality. The resulting field is then provided by the following

$$\mathcal{E}_j(t) = \int_{-\infty}^{\infty} \left(\mathbf{E_j^0} + \mathbf{E_j}(\omega)\right) \hat{a}(\omega) e^{-i\omega t} d\omega, \tag{3.14}$$

where each dipole responds identically in time, that is, $\mathbf{E^0}(x_j, y_j, z_j, t) = \mathbf{E_j^0} a(t)$ with $a(t) = \int_{-\infty}^{\infty} \hat{a}(\omega) e^{-i\omega t} d\omega$.

For point dipoles the instantaneous optical force acting upon them was calculated by using the Lorentz equation for mechanical force derived from electromagnetic fields [133]:

$$\mathbf{F_j}(t) \;=\; \frac{1}{2}\Re((\mathbf{p}_j \cdot \nabla)\mathcal{E}_j^*(t) + \partial_t \mathbf{p}_j \times \mu_0 \mathcal{H}_j(t)^*), \tag{3.15}$$

where * is the relevant complex conjugate, and $\mathcal{H}_j$ the magnetic field. The time-averaged optical force is given by

$$< \mathbf{F_j} > \;=\; \frac{1}{\Delta t} \int_0^{\Delta t} \mathbf{F_j}(t) dt, \tag{3.16}$$

where Δt is the pulse duration defined with $a(t \leq 0) = a(t \geq \Delta t) = 0$. Through use of Parseval's theorem, $\partial_t \mathbf{p}_j(\omega) = (-i\omega)\mathbf{p}_j(\omega)$ for one frequency component, $\hat{a}(-\omega) = \hat{a}^*(\omega)$ and according to the defined local field $\mathcal{E}_j(\omega) = \left(\mathbf{E_j^0} + \mathbf{E_j}(\omega)\right)$ we subsequently obtain

$$< \mathbf{F_j} > \;=\; \int_{-\infty}^{\infty} d\omega \frac{1}{2}\Re((\mathbf{p}_j(\omega) \cdot \nabla)\mathcal{E}_j^*(\omega) + (-i\omega)\mathbf{p}_j(\omega) \times \mu_0 \mathcal{H}_j(\omega)^*), \tag{3.17}$$

Finally, through use of Maxwell's equation for time-averaged electromagnetic induction, $i\omega\mu_0\mathcal{H} = c\nabla \times \mathcal{E}$ the following is obtained

$$< \mathbf{F_j} >_i \;=\; \int_{-\infty}^{\infty} d\omega \frac{\epsilon_0}{2}\Re(\alpha \mathcal{E}_j(\omega) \cdot \partial_i \mathcal{E}_j^*(\omega))|\hat{a}(\omega)|^2 \tag{3.18}$$

Equation 3.18 can be used for an arbitrary distribution of scatterers and appropriately generalises the monochromatic optical binding force [128] for the broadband optical binding situation.

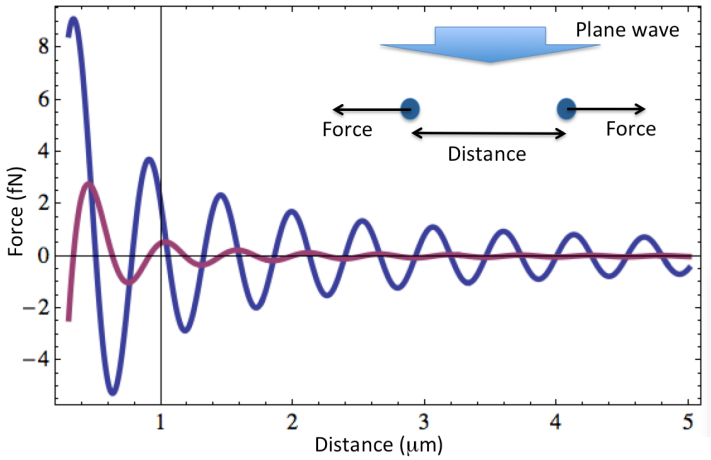

Figure 3.9: Optical binding force between two particles under illumination from light at 800 nm having a perpendicular polarisation (blue, large oscillations) or a parallel polarisation (magenta line). An illustration in this figure indicates the general orientation used in obtaining the graph.

3.7.3 Broadband ultrashort pulsed optical binding

It is known that the optical binding spatial periodicity for CW illumination depends upon the wavelength within the host medium [109, 121]. As such, where multiple wavelengths are present, each constituent has its own associated binding potential, which overlap with one another. When using broadband light therefore, the binding potentials are certainly expected to overlap. The analysis in the previous section presents this exact argument through equation 3.18. In this section broadband illumination is considered having a bandwidth of 100 nm centred at 800 nm, thus corresponding to a 9.4 fs pulse. For calculation of polarisability the particles have a diameter of 100 nm. The peak electric field amplitude used was 1.1×10^7 V/m, which corresponds to an average power of 1.0 W with a beam waist of 2 μm. In each case the perpendicular and parallel polarisations relative to the long axis of the focussed beam were considered. The broadband situation was also directly compared with the CW case to demonstrate how much distortion might be expected. Fig. 3.9 refers to a comparison between the binding forces when the particles are illuminated

by perpendicular or parallel polarisations, wherein the amplitude of oscillations decreases more rapidly with distance for the parallel case.

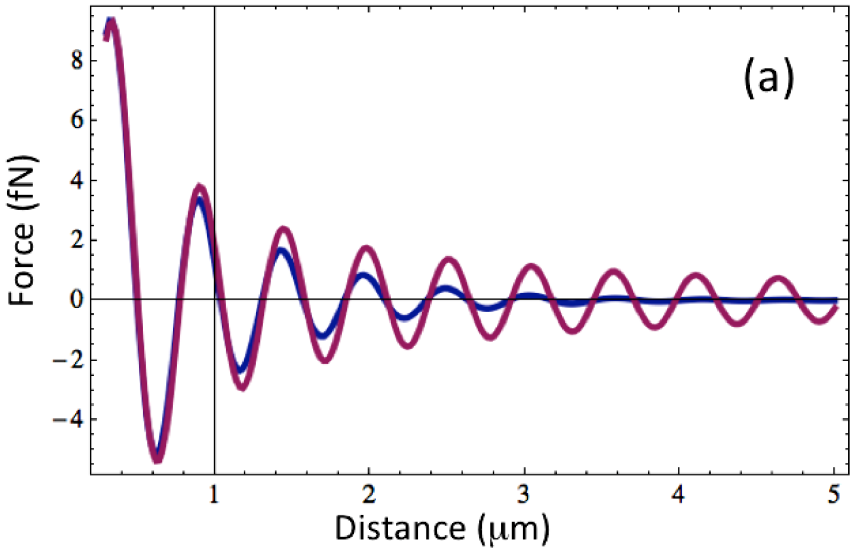

Figure 3.10: Comparison of binding forces for perpendicular polarisation optical binding under 800 nm-centred broadband illumination. In this case the larger oscillations (magenta) refer to the CW case; the smaller oscillations (blue) refer to the broadband case. Note the significant decrease in oscillation amplitude with increasing separation.

Fig. 3.10 features broadband binding, wherein a 100 nm bandwidth pulse is directly compared with the CW equivalent for the perpendicular polarisation. Further, Fig. 3.11 includes the same parameters but with parallel polarisation instead.

As expected for the broadband case the binding forces are decreased in magnitude relative to the CW case. Further, there is a significant difference between the two illumination polarisations. In the case of the perpendicular polarisation the difference between broadband and CW illumination is obvious. Whereas for the parallel polarisation case there is not much observable difference. This would likely manifest itself in an experimental regime, thus a difference as described would be most likely observed with the correct polarisation direction. It should be re-stated that these results refer to Rayleigh-sized particles. However, equivalent results have been demonstrated in the Mie-size regime. The main point to consider is the minimum centre-to-centre distance between the particles described in the experiments is 1.8 microns. Therefore this would be equivalent to

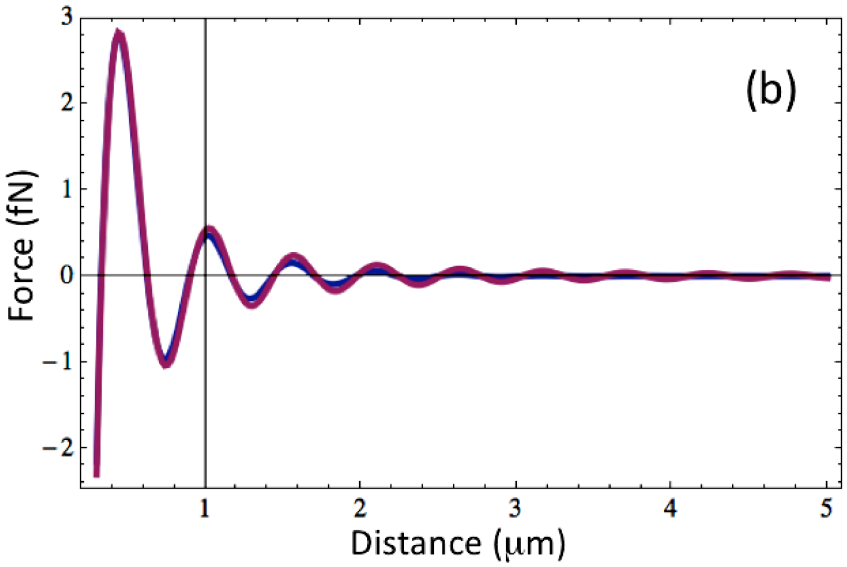

Figure 3.11: Comparison of binding forces for parallel polarisation optical binding under 800 nm-centred broadband illumination. As in Fig. 3.10, the larger oscillations (magenta) refer to the CW case; the smaller oscillations (blue) refer to the broadband case. Note the significant decrease in oscillation amplitude with increasing separation and also the generally smaller amplitude of force oscillations.

approximately 3.5 wavelengths at the experimental wavelength of 514 nm. Whereas for Rayleigh-sized particles they are small enough for this aspect to be negligible.

3.7.4 Broadband SHG ultrashort pulsed optical binding

As a further study the effect of using broadband SHG illumination was examined, as might be generated from frequency doubled pulses as above. In the model it was assumed that a 10% SHG conversion efficiency was appropriate. Fig 3.12 shows a comparison for CW illumination using perpendicular and parallel polarisations, which is the 400 nm centre wavelength equivalent to Fig. 3.9.

The wavelength bandwidth associated with transform-limited frequency doubled light is a quarter that of the fundamental pulse, i.e. a 100 nm fundamental pulse is equivalent to 25 nm a frequency-doubled pulse. The maximum bandwidth obtainable form a frequency-doubled pulse is subject to the spectral conversion efficiency, which largely depends collectively on the phase-matching, GVM and IGVD in the case of ultrashort

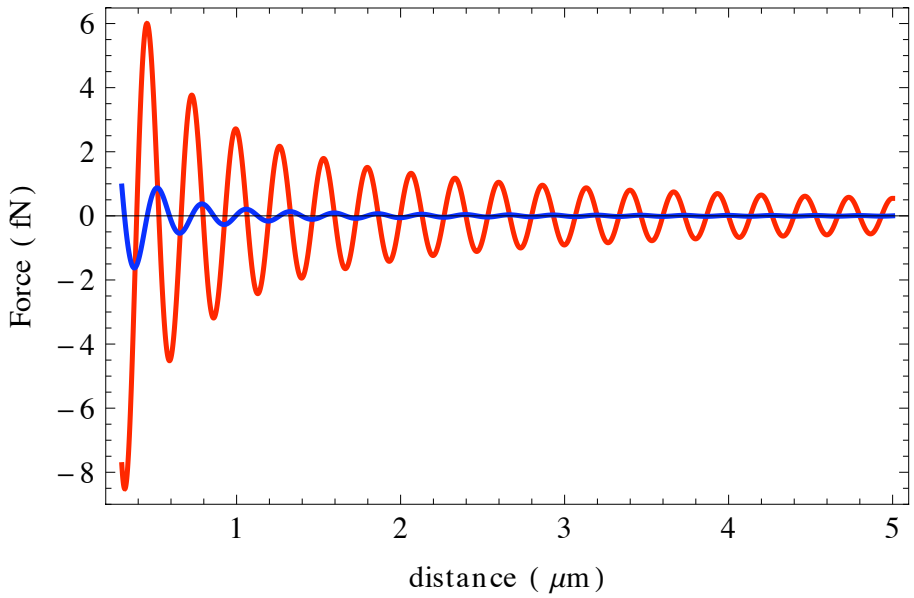

Figure 3.12: Comparison of binding forces for perpendicular and parallel polarised trapping beams for CW SHG illumination at 400 nm. Note the forces are comparable with the 800 nm case despite a factor of ten lower power due to shorter wavelengths being more readily scattered. The larger (red) oscillations correspond to perpendicular light; the relatively smaller oscillations correspond to parallel light.

pulses. The expected bandwidth of SHG light can be calculated either by considering the minimum pulse duration of the fundamental pulse and relating the corresponding frequency bandwidth according to equation 1.12. However this approach ignores the phase and therefore is only appropriate in the case of transform-limited pulses. Instead, equation 2.3 can be used to calculate the bandwidth of SHG pulses when dispersion is present. It should be noted that for the shortest ultrashort pulses the generated SHG is unlikely to achieve theoretical bandwidth due to (i) spectral conversion efficiency, and (ii) spectral phase distortions.

Figs. 3.13 and 3.14 illustrate the SHG equivalent of the fundamental pulses in Figs. 3.10 and 3.10, respectively, wherein the pulse durations are identical for both cases. However in the SHG versions the broadband illumination results in a lesser smoothing of binding force oscillations as a result of the lower wavelength bandwidth requirements. Therefore a wider wavelength bandwidth (corresponding to shorter pulse duration) is required in order to achieve oscillation smoothing to the equivalent effect of pulses centred at 800 nm. Fig. 3.15 implements a broader bandwidth of 50 nm, corresponding to a 4.7 fs

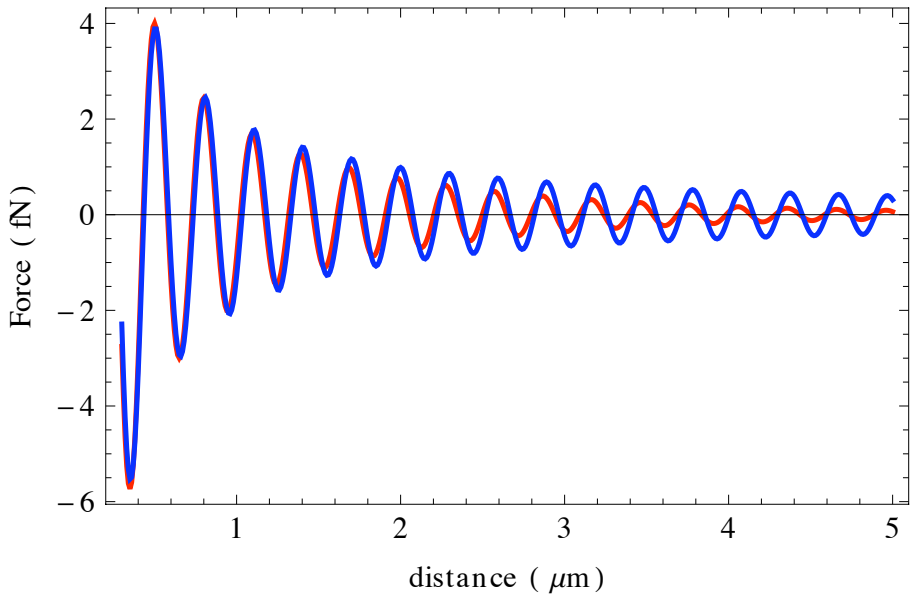

Figure 3.13: Optical binding forces for perpendicular polarised SHG light for either broadband (25 nm) or CW cases. The broadband SHG pulse corresponds to a 9.4 fs pulse. The larger (blue) oscillations correspond to CW light; the relatively smaller oscillations (red) correspond to broadband light.

SHG pulse to demonstrate the required pulse duration necessary to achieve binding force oscillation smoothing.

For broadband SHG illumination the binding force oscillations are relatively smoothed compared with the narrowband cases. However, the shorter pulse durations are required to effect the same degree of smoothing as observed for fundamental pulses at 800 nm. The perpendicular polarisation may result in an experimentally realisable smoothing for broadband illumination, however for the parallel polarisation the difference between broadband and CW appears to be negligible.

3.8 Conclusions

Experiments were performed to attempt to observe the transverse optical binding effect for Mie-sized particles under CW illumination at 514 nm. It was demonstrated that the long-ranged nature of the optical binding force, also showing the polarisation dependence of the optical binding forces. The binding forces were experimentally found to act over a relatively long range in an experimental scenario, in particular up to around 15 wavelengths

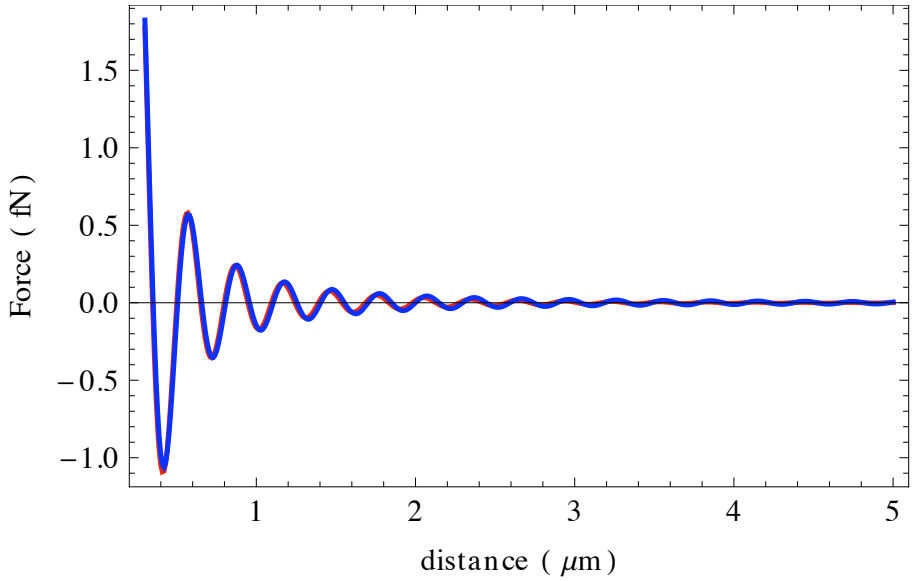

Figure 3.14: Optical binding forces for parallel polarised SHG light for either broadband (25 nm) or CW cases. The larger (blue) oscillations correspond to CW light; the slightly smaller oscillations (red) correspond to broadband light.

for the perpendicular polarisation at 514 nm. The force arising from parallel polarised light decays far more quickly with increasing distance than the perpendicular polarisation.

In relation to the broadband optical binding work it should be noted that broadband sources could include: a) a broadband 10fs source, b) an ultrabroadband 5fs source or c) a supercontinuum-ultrabroadband source. CW experiments were necessary as a preliminary study as little experimental work on this topic had been previously considered. The amplitude and direction of the incident and scattered electric field in the region of the focus defines the strength of any binding force. Importantly, if the electric field amplitude was too small, statistical fluctuations (Brownian motion) would wash out binding oscillations. In this case, the results would provide a flat potential with no oscillations, which is identical to the expected result from a sufficiently broadband source. Therefore, the same optical power would be required for broadband sources (providing focussing conditions are identical). However, after transmission through a typical optical binding experimental setup, average powers from typical Ti:Sapphire systems may not be enough to permit observation of optical binding. Therefore, a supercontinuum source was attempted due to its high average power (6W). In this case only 50 mW of average power remained after transmission through the setup. Alternative configurations may provide sufficient binding force amplitudes, for example, by enhancing the focussing conditions to provide a higher

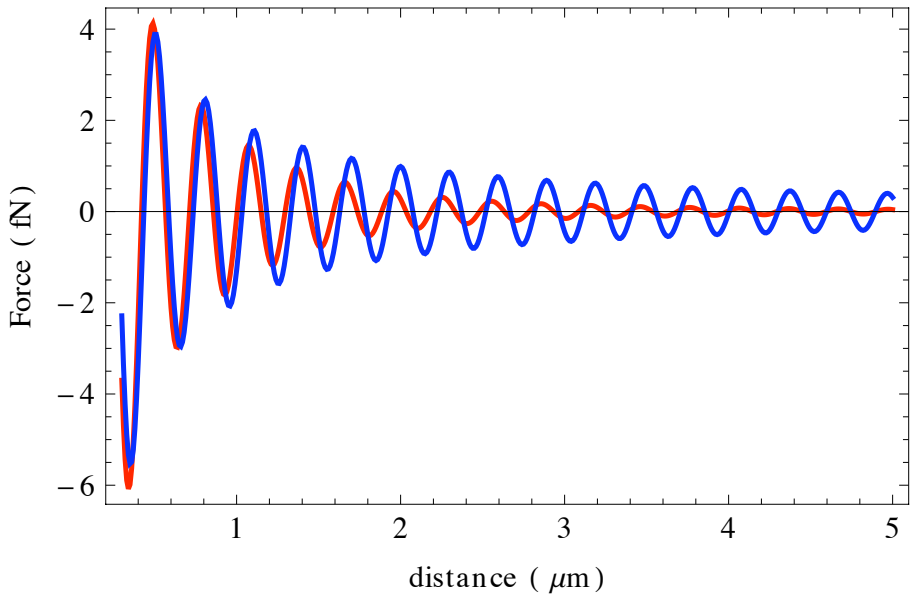

Figure 3.15: Optical binding forces for perpendicular polarisation under either broadband (50 nm) or CW SHG illumination. The broadband pulse corresponds to a 4.7 fs pulse. This shorter pulse duration is necessary in order to introduce sufficient smoothing of oscillations as seen for fundamental pulses. The larger (blue) oscillations correspond to CW light; the relatively smaller oscillations (red) correspond to broadband light.

peak intensity at the beam focus. However, the purpose of the theoretical studies was to build a framework for future experiments. In order to understand how much bandwidth is required to observe binding then modelling is required. This way future experiments could be designed with those modelling results in mind.

We further attempted to model the experimental studies using the finite element method to investigate the optical binding forces from a computational perspective. We did not obtain reliable results in this endeavor, however some indicative data demonstrating the oscillatory nature of optical binding was observed. We also used an interacting dipole method to model point oscillators with the polarisability calculated from 100 nm diameter particles for CW and broadband illumination. The wavelength of the illuminating light provides a well defined oscillatory optical binding force relationship for varying inter-particle distance or broadband illumination. However in broadband illumination this well-defined relationship breaks down because the optical binding potential is spatially dependent upon wavelength and so regions which attract the particles do so with less force than if using CW illumination. We further investigated SHG-illuminated optical binding

and found that the pulse duration required for binding wavelength-dependent oscillations is substantially shorter for SHG than for fundamental pulses due to the lower wavelength content within the pulse. The computational results are potentially indicative of the binding interaction in an experimental setting in that a very wide bandwidth is required for smoothing of the binding oscillations. It should be noted that in any future work involving ultrashort pulses, the MIIPS system would be arbitrarily capable of delivering near transform-limited ultrashort pulses at the sample plane for the envisaged experiments..

The experimental work in this chapter has been published in (i) Proc. SPIE, **7400**, 2009 [121], (ii) J. Phys. Condens. Matter, 2012 (accepted) [134] and (iii) Proc. SPIE, 2012 (accepted).

3.9 Chapter acknowledgements

In this chapter Michael Mazilu designed and implemented the computational studies including finite element models and the interacting dipole models. Further, Joerg Baumgartl designed the experimental aspects and related particle tracking software in LABVIEW. The author built experimental setups and performed computational studies by adapting and editing the computational models as appropriate.

Chapter 4

The role of femtosecond pulse duration in the membrane permeabilisation of mammalian cells

4.1 Introduction

This chapter covers experimental work to characterise the ultrashort laser pulse-induced membrane permeabilisation of mammalian cells. Most importantly, the studies in this chapter would not be permitted were it not for the pulse shaping and measurement apparatus referred to previously. This is because dispersion is difficult to measure accurately. The MIIPS procedure provides means for measuring phase *in situ* to enable delivery of optimised transform-limited ultrashort pulses. The membrane permeability is quantified by performing dye injection experiments known as optoinjection. In this study I performed experiments across a wide parameter space including pulse duration, pulse energy and number of pulses. The results show that two distinct membrane permeabilisation regimes exist. The first of these regimes show an initial nonlinear dependence of order 3.5-9.6, with the second regime exhibiting a typically linear dependence. The transition between these two regimes is marked by a threshold peak power of between 6-20 kW. These results indicate that multiphoton absorption produces a quasi-free electron plasma within the focus of the beam, with the membrane permeabilisation mechanism requiring this multiphoton initiation for the subsequent regime change, whereby linear absorption dominates. Fur-

thermore I show that the number of pulses define the probability with which membrane permeabilisation occurs over time, with the peak power defining the mean and standard deviation number of pulses in order to achieve 50 % efficiency.

Ultrashort laser pulses have proven to be important in the field of biophotonics [135]. The high peak power associated with the ultrashort pulses is crucial for initiating a nonlinear response from matter, and this nonlinear property is very useful in the case of biological matter. However, manipulating biological matter using ultrashort pulses requires extraordinary care due to the possibility of damage resulting from over-exposure to the high intensities associated with focussed laser beams. Therefore it is important to understand what effect different laser parameters have on biological material. The relevant parameters are laser wavelength (and bandwidth), pulse energy, spatial beam profile, laser repetition rate, number of pulses and pulse duration (and pulse shape).

Ultrashort pulses have been used in a wide variety circumstances concerning biological matter. These can be defined in terms of regimes relating to extent of damage which occurs upon laser irradiation. The first of these regimes is the low damage regime, with low cell death rates associated with irradiation with laser beams whose parameters are such that no short term damage occurs. Naturally, any exposure to light can cause damage and some cell death ensues. The main application of ultrashort pulses in the low damage regime is imaging. For example, two-photon excited fluorescence (TPEF) and second harmonic generation (SHG) are important methods for the high resolution imaging of thick biological matter [136]. The application of longer wavelengths, typically in the near infrared also adds the prospect of deeper penetration using such modalities. Both TPEF and SHG exhibit a quadratic dependence upon the peak intensity of the incident laser field [17], therefore the signal to noise ratio is greatly improved owing to the nonlinear response associated with the ultrashort pulses. The high damage regime can be defined in terms of the rapid onset of irreversible damage and cell death. This regime has applications in single-cell nanosurgery and tissue surgery, wherein nanosurgery is defined in terms of spatially constrained surgery down to the nano-scale [137, 138]. In this regime a wide parameter space covering pulse energy [139] and repetition rate [140, 141] have been investigated. The pulse duration dependence of nanosurgery has also been investigated in which an approximate $\tau^{-1/2}$ relationship was found [142]. Typically the laser parameters used in optoinjection and phototransfection experiments are similar, for example being of the order of nJ for MHz repetition rate pulses [141]. Phototransfection using sub-20 fs pulses has been demonstrated using pulse energies of less than 93 pJ [18].

For this chapter, the region between the low damage and high damage regimes is particularly relevant. The correct choice of laser parameter is essential for maintaining the

desired effect and therefore it is crucial to understand the processes leading up cell damage in order to either prevent this damage, or to utilise this damage. One of the applications in this region between low and high damage is phototransfection [143]. Phototransfection involves the permeabilisation of a single-cell membrane using focussed a laser beam in order to permit the introduction of membrane-impermeable genetic material into the cell itself. Understanding the mechanisms which permit the phototransfection of cells is essential for future development of the field. Due to the multiple biological fluctuations associated with cell transfection, it is impractical to gather sufficient statistics to help understand the processes leading to cell membrane permeabilisation. Instead, we utilise another light-induced membrane permeabilisation technique known as optoinjection [144]. Optoinjection involves the introduction of membrane-impermeable fluorescent dyes into single cells. This technique is completely equivalent to the phototransfection technique, however, the technique offers superior statistical information due to the consistent reproducibility of the technique.

The processes leading up to membrane permeabilisation are complicated and not yet fully understood [137]. Currently, the model by Vogel *et al.* offers the greatest insight into membrane permeabilisation mechanisms [137]. In this model, biological material is considered as an amorphous semiconductor based on pure water, due to the high water content of cells. The justification of using water is due to the high water content of cells. However, it is noted in this model that in reality the situation is considerably more complicated, for example, by proteins, lipids, dyes and the like. Upon irradiation with ultrashort laser pulses, multiphoton absorption promotes electrons from the valence band up to the conduction band. Inverse Bremsstrahlung absorption events in which conduction electrons are scattered by incident photons increases the kinetic energy of these electrons up to a critical energy sufficient for impact ionisation to occur. An avalanche increase in the population density of conduction electrons means that a quasi-free electron plasma is formed in the region of high intensity laser pulses. This plasma is associated with the disruption and modification of chemical bonds in the region and subsequently membrane permeabilisation can occur. The multiphoton initiation of membrane permeabilisation is therefore a critical feature for ultrashort pulse optoinjection and phototransfection. The parameters associated with defining the multiphoton response are the pulse duration and pulse energy due to their connection with the peak power through the formula

$$P_{\text{peak}} = k_s \frac{E_p}{\tau_p} \tag{4.1}$$

where k_s is a constant which depends on the temporal profile of the pulse, W_{p} is the pulse

energy and τ_p is the pulse duration. Several studies have investigated the parameter space for cell membrane permeabilisation. In particular, the optoinjection efficiency as function of pulse energy and number of pulses has been investigated [139, 144]. The phototransfection efficiency has been investigated for various parameter including laser fluence [143] and spatial beam profile through the generation of novel beam shapes [145]. In terms of pulse duration, there has been one study concerning optoinjection and phototransfection of cells using sub-20 fs pulses, in which significant decreases in pulse duration permitted phototransfection at decreased pulse energies [18].

We have experimentally determined the absorption characteristics of mammalian cell membranes to ultrashort pulses within the temporary modifcation regime. This study comprehensively covers the laser parameters pulse duration, pulse energy and number of pulses. Crucially, this study is made possible through the implementation of the MIIPS technique in order to measure and characterise the pulse duration *in situ* at the focus of the microscope objective. Without the MIIPS technique this would not have been possible due to the complicated dispersion profile of the experimental setup. The implications of the results and have found that the nonlinear (multiphoton) absorption is critical for initiating efficient linear absorption. The nonlinear absorption generates a quasi-free electron plasma within the focal region of the laser pulse which collectively alters the nonlinear and linear absorption characteristics over a series of pulses. In particular it was found that a peak power threshold defines the region between the (intially) nonlinear and (finally) linear absorption. Furthermore, the number of pulses required to initiate optoinjection strongly depends upon the peak power associated with pulse duration and energy, with a sufficiently high peak power necessary for efficient optoinjection.

4.2 Methods

4.2.1 Experimental arrangement using MIIPS system

The experimental arrangement is shown in Fig. 4.1. A KM Labs Swift 10 Titanium Sapphire oscillator (bandwidth = 60 nm, center wavelength = 800 nm, transform-limited pulse duration of 17 fs) was used for all the optoinjection experiments. A Nikon Eclipse Ti inverted microscope was used with two objectives employed. A Nikon 0.8NA/60x air objective was used when acquiring and measuring the shortest possible pulse duration and for completing the optoinjection experiments. A Nikon 40x/0.75NA phase contrast objective and an Andor Clara CCD camera cooled to -55°C were used for phase contrast and fluorescent images. An electronic shutter (home-built electronic controller; Newport

shutter) was used to controllably permit a specified number of pulses.

Fig. 4.2 shows the fundamental laser spectrum and typical phase distortion obtained and corrected by the MIIPS procedure, as discussed in described in chapter 2. Crucially, the shape of the dispersion profile indicates significant higher order phase contributions that would not be easily measured and compensated for without the MIIPS procedure. We controllably stretched the pulses using anti-reflection coated BK7 optical flats. The flats contribute GVD to the beam, stretching the pulse without introducing higher order effects. This was confirmed by measuring the dispersion caused by the flats using the MIIPS system. Only second-order dispersion was introduced by the optical flats with negligible higher-order contributions. Furthermore, the anti-reflection coated flats maintained the same optical transmission even when several flats were inserted into the beam path. Using a combination of 3mm and 5mm thickness flats the following pulse durations were obtained: 17, 28, 44, 68, 80, 105, 120 and 143 fs. GVD does not change the temporal profile other than affecting the peak power inversely for increasing pulse duration [132]. The optical flats did not in away change the spatial profile or direction of the beam and were carefully inserted into the beam path so as to avoid any adverse effects.

4.2.2 Optoinjection: cell culture and experimental procedure

Chinese Hamster ovary (CHO) cells were cultured in medium consisting of Minimum Essential Medium (Sigma), 10% Fetal Calf Serum (Sera Laboratories International) and L-Glutamine, Penicillin and Streptomycin (Sigma). The cells were plated on 23 mm glass-bottom Petri dishes (Fluorodish, World Precision Instruments) and incubated for at least 24 hours until cells populated the bottom of the Petri dish.

Optoinjection experiments were performed to assess the cell membrane permeability as function of laser parameter [146]. The membrane-impermeable dye, Propidium Iodide (PI, Sigma-Aldrich) was used to indicate whether the cell was permeabilised by the absorption of laser pulses. The medium was subsequently removed from the Petri dish containing the adherent cells. The Petri dish was washed twice with Opti-MEM (Invitrogen). A 3 μM solution of PI in Opti-MEM was added to the sample dish, wherein Opti-MEM was the solvent. PI molecules bind to DNA and RNA in the cell and glow red under green excitation when suitably bound to those molecules [147]. The phase-contrast objective was used to image cells as it provided better contrast for the cells, which are relatively transparent. The laser parameter choice was selected and the 60x/0.8NA objective used to irradiate the cell of interest at 3 axial locations, separated by 1-2 microns. The cells of interest were chosen by drawing a small square (on the underside of the sample dish)

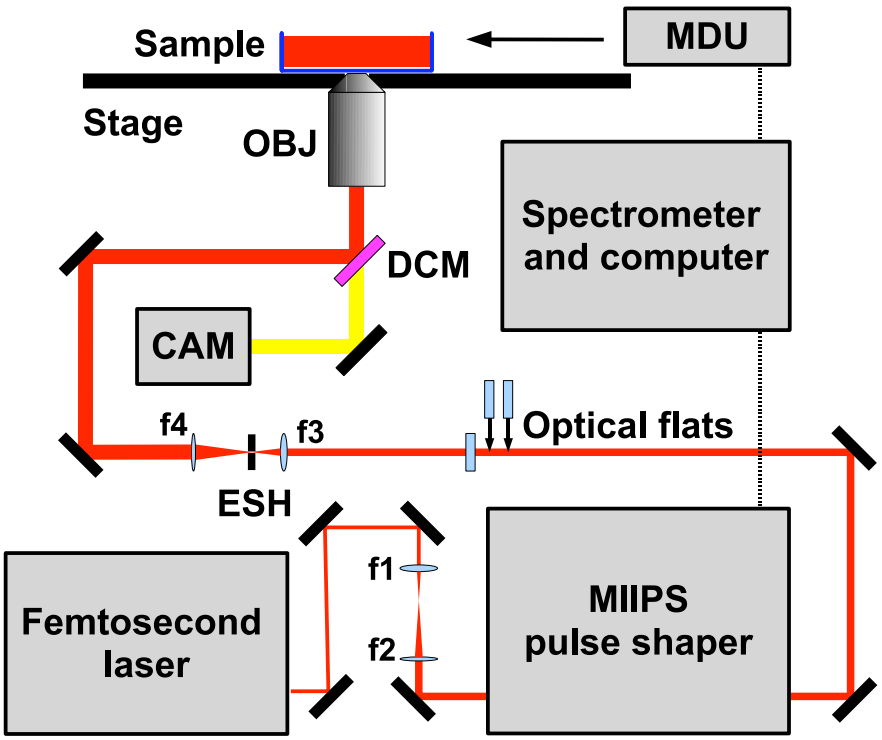

Figure 4.1: Experimental setup with CAM representing the electronically cooled camera, DCM: dichroic mirror, ESH: electronically controlled shutter, MDU: MIIPS microscope detection unit, OBJ: objective lens and OF: optical flats. The lens f1 through f4 refer to the following sequence of focal lengths: 10 cm, 20 cm, 10 cm and 25 cm. The illumination scheme, mercury lamp and filter cubes are not shown for clarity.

so as to identify the relevant cells within that square when viewed under the microscope. Preferably the square was small enough so that approximately less than 50-60 cells were in the square at one time. This was to assist in decreasing the number of cells requiring identification during each stage of the process. Targeting at three sufficiently separate axial locations does not compromise cell viability providing the axial separation is large enough [146]. The pulse energy at the sample was calculated using the dual-objective transmission method [148] with a power meter to measure average power and using the known repetition rate of 76 MHz. The Nikon 60x/0.8NA objective was found to have a transmission ratio of 66%. Thirty cells were targeted and irradiated by the laser in each

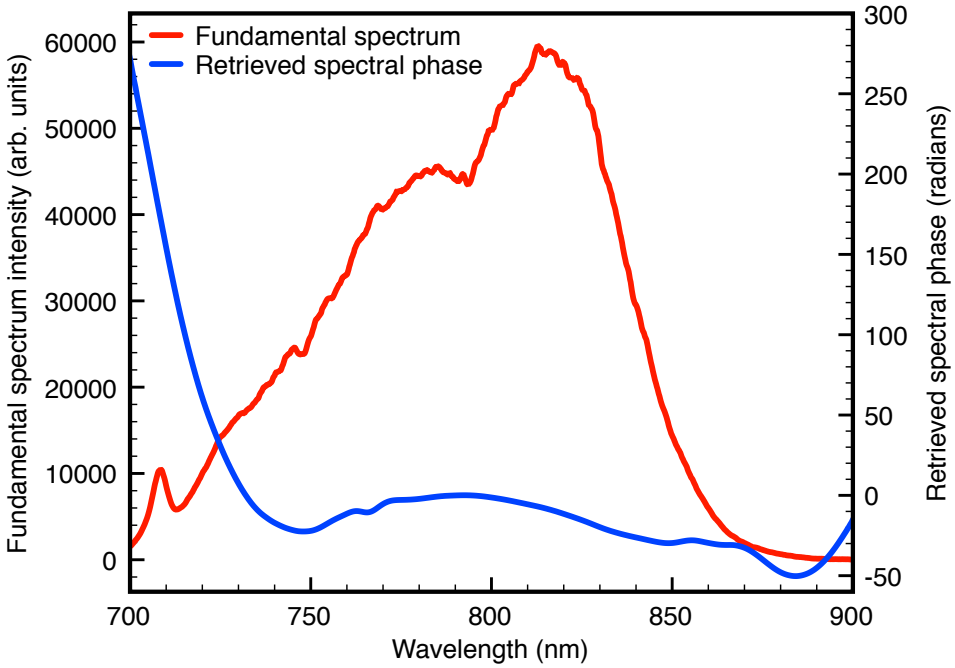

Figure 4.2: Fundamental laser spectrum with the retrieved spectral phase dispersion profile obtained by the MIIPS procedure.

Petri dish. After 5 minutes a fluorescence image was taken to check which of the targeted cells contained PI. This was compared with a control fluorescence image to check for false positives. The efficiency of optoinjection was calculated as the ratio between successfully optoinjected (fluorescent) cells and the number of targeted cells. The PI solution was then removed and the cells were washed twice with culture medium and fresh medium was added and the cells incubated for at least 90 minutes. A live assay with Calcein AM (CAM, Invitrogen) was implemented to check the viability of cells after 90 minutes, wherein CAM interacts with esterases in the cell, which are only present if the cell is alive [146]. Viability was consistently 100% for the low-medium optoinjection efficiency (<60%) samples. After which, viability was only checked where optoinjection efficiency was significantly higher than 60%, or if a visible microbubble was observed during the targeting procedure.

To obtain adequate statistics, each experiment involving a different set of parameters was repeated 8 times per set, each referring to 8x30 cells. The phase contrast and fluorescent images obtained from a representative optoinjection experiment are shown in false colour in Fig. 4.3 and show cells that were successfully optically injected and the

corresponding viable cells.

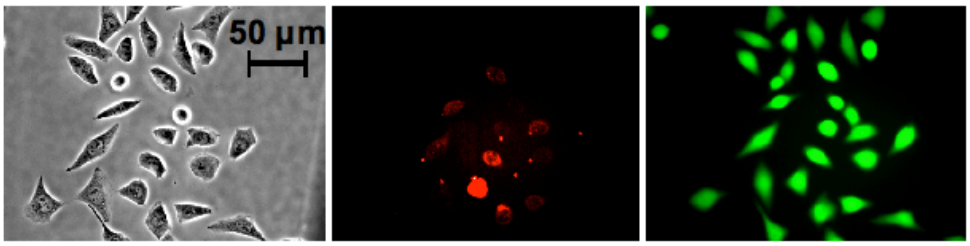

Figure 4.3: Example image of cells optically injected with PI and tested for viability with CAM. Left: Before irradiating (phase contrast), Center: PI uptake (false colour), Right: CAM viability test (false colour).

4.3 Results: optoinjection

A wide parameter space covering multiple combinations of pulse duration, pulse energy and number of pulses was explored. For reference purposes, Table 4.1 displays the relationship between these three parameters and the associated expressions which relate the parameters to the independent variables: peak power and total energy. Table 4.2 summarises the parameter space explored.

4.3.1 The role of pulse duration

By varying the pulse duration it was possible to controllably change the peak power without affecting the total energy, thereby defining the efficiency with which nonlinear processed occurred without being concerned with separate linear absorption issues. The time-averaged intensity-response (S^n) for number of photons (n) follows

$$S^n \propto W_{\mathrm{p}}^n \tau_p^{1-n}, \tag{4.2}$$

where W_{p} is the pulse energy and τ_p is the pulse duration [149]. The optoinjection process requires optical absorption in the locality of the cellular membrane, with the efficiency depending upon linear and nonlinear absorption. However, the nonlinear absorption mechanisms do not necessarily depend upon any one order of n-photon processes. Therefore we introduce a new concept which we refer to as an effective photon number, n_{ef}. This is due to the multiple possibilities for multiphoton absorption owing to the complex nature of the biological matter. The molecules contained within the biological matter each have their

	Pulse duration (τ)	Pulse energy (W_p)	Number of pulses (N_p)	Expression
Peak power (P_peak)	$\propto \tau^{-1}$	$\propto W_\mathrm{p}$	no effect	$P_\mathrm{peak} = kW_\mathrm{p}\tau_p^{-1}$
Total energy (E_total)	no effect	$\propto W_\mathrm{p}$	$\propto N_p$	$E_{total} = W_\mathrm{p}N_p$
Associated absorption mechanisms	Nonlinear only	Nonlinear and linear	Linear only	$\langle S^n \rangle \propto W_\mathrm{p}^n \tau^{1-n}$
Fig. reference:	4.4	4.5	4.6	

Table 4.1: The three varied parameters: pulse duration, pulse energy and number of pulses influence peak power and total energy in the manner shown on the table. The expressions associated with peak power (P_peak) and total energy (E_total) are also shown with k being a constant depending on the temporal profile of the pulse. The table also shows whether the parameter is generally associated with influencing either the nonlinear or linear absorption mechanisms and the associated expression.

own nonlinear cross section, defining the probability of nonlinear processes occurring. We therefore can represent S^n in terms of a sum of several different nonlinear orders

$$\langle S^n \rangle = \sum_{i=1}^{n} k(i) W_\mathrm{p}^i \tau_p^{1-i}, \tag{4.3}$$

where $k(i)$ represents the probability that the i number of photons are responsible for the given interaction. If the sum is normalized it will yield a probability that a n-photon process is responsible for the interaction. However it is not possible to establish the probability of each the n-photon components. Therefore we must average the number of photons responsible and instead calculate the effective photon number, n_ef. The interpretation of the effective photon number therefore indicates the number of photons with the highest probability of being responsible for an interaction, or the dominating photon number. However it must be stressed that a different photon number could simultaneously be responsible for the interaction and therefore the effective photon number is weighted over several photon numbers. Consequently the effective photon number will not necessarily have an integer value but instead it indicates the approximate photon number responsible for the interaction.

By considering the parameter $\langle S^n \rangle$ to be equivalent to the probability that the cell

Experimental set: (Fig. reference)	Pulse duration range (fs)	Pulse energy range (nJ)	Number of pulses ($\times 10^6$)	Photon order (n_{ef})	Threshold peak power (kW)	Mean pulse number ($\times 10^6$)
1: (4.4)	17-68	0.5	3.0	1.5 ± 0.2	8 ± 2	N/A
1: (4.4)	68-143	0.5	3.0	3.5 ± 2.0	as above	N/A
2: (4.4)	17-80	1.1	1.5	1.5 ± 0.2	11 ± 2	N/A
2: (4.4)	80-143	1.1	1.5	6.6 ± 2.5	as above	N/A
3: (4.4)	17-80	1.8	0.4	3.6 ± 0.5	N/A	N/A
4: (4.5)	17	0.33-0.6	3.0	0.9 ± 0.2	18 ± 2	N/A
4: (4.5)	17	0.26-0.33	3.0	7.6 ± 2.0	as above	N/A
5: (4.5)	68	0.53-0.8	3.0	1.3 ± 0.5	7 ± 1	N/A
5: (4.5)	68	0.40-0.53	3.0	5.7 ± 2.3	as above	N/A
6: (4.5)	17	0.53-0.8	0.4	3.3 ± 1.0	N/A	N/A
7: (4.6)	17	0.5	0.4-3.0	N/A	N/A	1.1 ± 0.5
8: (4.6)	44	0.5	0.8-6.0	N/A	N/A	3.4 ± 1.5
9: (4.6)	80	0.5	1.5-7.5	N/A	N/A	10 ± 6

Table 4.2: Summary of experimental parameter space explored. Sets 1-3 refer to experiments involving varying the pulse duration, sets 4-6 refer to experiments involving varying the pulse energy and sets 7-9 refer to experiments involving varying the number of pulses. Also note the threshold peak powers are calculated at the inflection points on the data fits; the inflection points are unavailable for sets 3 and 6 and are listed as N/A in the table. Finally, the mean pulse numbers were calculated by considering a Gaussian error function fitted to the data in Fig. 4.6 and performing a linear regression fit to find the mean pulse number. The ERF was numerically differentiated to find the probability density function (PDF) and corresponding standard deviation. Where not applicable these are also listed as N/A. The parameters were chosen initially to reflect typical values used in the field (40 ms irradiation times). Subsequently, parameters were chosen to see what happened if one parameter was dramatically changes, for example, doubling the pulse energy.

will be permeabilized we can associate the effective photon number with the optoinjection efficiency. We do this by taking the logarithm of

$$\langle S^n \rangle = W_{\mathrm{p}}^{n_{\mathrm{ef}}} \tau^{1-n_{\mathrm{ef}}} \tag{4.4}$$

and varying τ_p and holding W_{p} constant, or vice versa. We perform a linear regression fit on the gradient obtained on a log-log scale of optoinjection efficiency. We associate the obtained gradient with the effective photon number. Therefore in varying τ_p the effective photon number is given by $n_{\mathrm{ef}} = 1 - m$ for a gradient m When varying W_{p} the effective photon number is given by $n_{\mathrm{ef}} = m$. We use this effective photon number n_{ef} to indicate the dominating order of the photon absorption process.

Fig. 4.4 shows the results from the optoinjection experiments for varying pulse duration. The optoinjection efficiency decreased rapidly with increasing pulse duration. In sets 1 and 2 there is a clear transition between low and high gradients. Next, by relating the gradients of optoinjection efficiency in the shorter pulse duration and longer pulse duration regions to the effective photon number, n_{ef} we obtained the effective photon numbers listed in Table 4.2. For sets 1 and 2 the effective photon number was between 1.3 and 1.7 below the 80 fs region for set 1 and 68 fs for set 2. Above these pulse durations the effective photon number was between 3.5 and 9.1. It should be noted that this defines the maximum range of effective photon numbers for these parameter sets. The larger error for longer pulse durations results from the requirement of log-log data for the analysis, where the lower efficiencies and error values record a log-value that is much greater in magnitude than for log-values from near unity. The point of inflection between high and low gradients defines the threshold pulse duration between the two separate regression fits. Where possible the threshold peak power was calculated at this threshold pulse duration The threshold peak powers were in the range 6-13 kW. For set 3 the behaviour is distinctly different from sets 1 and 2, with a higher effective photon number. This is probably due to the greater pulse energy and fewer number of pulses associated with this experimental set.

4.3.2 The role of pulse energy

To complement the pulse duration results we also performed optoinjection experiments for varying pulse energies, as indicated in Fig. 4.5. By increasing the pulse energy, both the peak power and total energy are simultaneously increased. This allows an interesting comparison with the pulse duration data as both methods imply an change in peak power, the only difference being whether the total energy accumulation is constant or varies

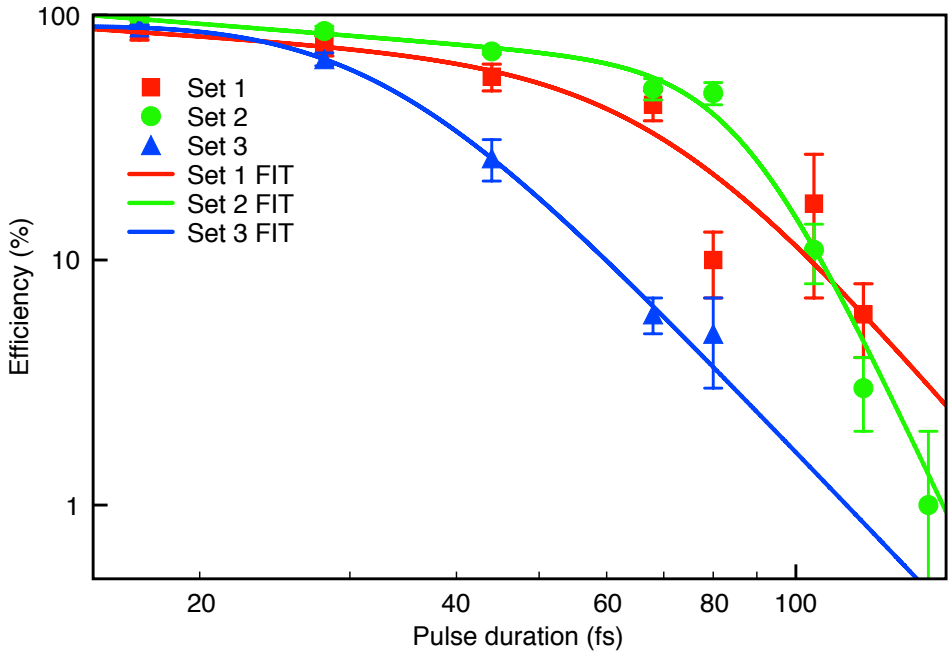

Figure 4.4: Optoinjection efficiency as function of pulse duration (τ_p), with each data point referring to the mean ± standard error of mean (s.e.m). The calculated fits shown for each data set represent continuous functions, which incorporate two separate linear regressions in the shorter pulse duration and longer pulse duration regimes. The point of inflection between each fit defines a transition value between the two regimes.

proportionally.

For each set of data we observed a substantial change in the optoinjection efficiency, which increased with pulse energy. As with the pulse duration data, a transitionary point was also observed between lower pulse energies and higher pulse energies The effective photon numbers were obtained by performing linear regression fits in the appropriate regions and these are summarised in Table 4.2. Below the threshold peak power the effective photon number was located in the maximum range of 3.4 and 9.6 for sets 4 and 5. It should be noted that this is the maximum range of effective photon number. Above the threshold, the effective photon order was approximately unity for each experimental set, implying a linear-type relationship. The threshold peak powers were found to lie within the range of 6-20 kW (sets 4 and 5). Set 6 behaved similarly to set 3. This similarity can be attributed to the greater peak power associated with these data sets.

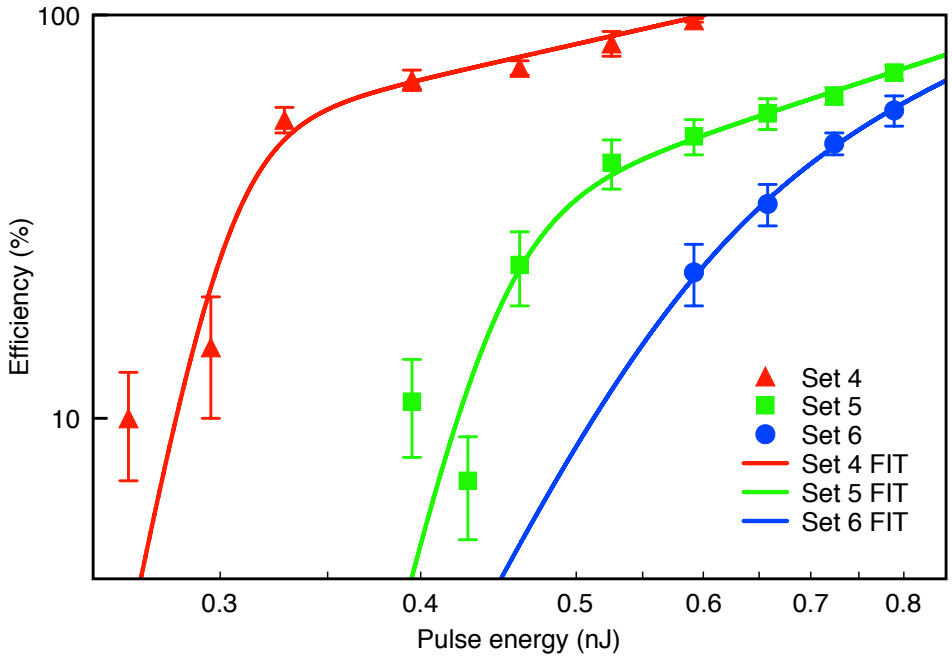

Figure 4.5: Optoinjection efficiency for varying pulse energy (W_p). Each data point is represented by the mean ± s.e.m. The fits shown represent continuous functions with gradients appropriately reflecting the effective photon number in both low and high pulse energy regimes. In each fit the value which defines the transition from low to high gradient is the peak power.

4.3.3 The role of number of pulses

Finally, we explored the efficiency as a function of the number of pulses applied. These experiments probe the time-dependent optical absorption properties of the cell membrane. By varying the number of pulses, as shown in Fig. 4.6 we observed a rapid change in membrane permeabilisation efficiency when shorter pulses (17 fs) are used compared to the case for longer pulses (80 fs). The typical number of pulses required for efficient membrane permeabilisation strongly depends on pulse duration.

In our experimental approach the efficiency of membrane permeabilisation was measured by the presence of fluorescent signal in the cytoplasm rather than its relative intensity. This stems from the observation that there is a clearly distinguishable difference in fluorescence intensity between the cells successfully optoinjected and the control population. This binary type of response to laser irradiation suggests that there is a threshold amount of accumulative damage required for permeabilisation with a step transition from

the impermeable to permeabilised state. A function $f(t)$ was utilised that describes the probability distribution of this transition as a function of time. The integral of $f(t)$ from 0 to N_p is equal to the experimentally measured membrane permeabilisation efficiency (shown in Fig. 4.6).

To find this probability distribution, one would ideally differentiate the data in Fig. 4.6 but this would result in significant numerical error. Instead, note that the obtained membrane permeabilisation efficiency curves for each parameter set can be approximated by a Gaussian error function (ERF), given by the solid lines in Fig. 4.6. Consequently, the membrane permeabilisation probability distribution has a form of normal distribution with the mean and standard deviation characteristic to the given set of laser parameters (dashed lines in Fig. 4.6). Considering a normal distribution of probabilities that a given parameter set will initiate membrane permeabilisation. By performing a linear regression fit on the data displaying a linear trend the mean number of pulses is found. The standard deviation is then found by visually fitting the ERF to the optoinjection data. The membrane permeabilisation probability density function is then found by numerically differentiating the ERF fit. Table 4.2 lists the mean number of pulses required to achieve 50 % efficiency and the corresponding standard deviation number of pulses. Clearly, the required number of pulses and standard deviation decrease significantly with the pulse duration providing robust and reliable membrane permeabilisation at short irradiation times. The similarity between the initiation behaviour when varying pulse duration or pulse energy mean that regardless of method of increasing the peak power one would also expect to see a decrease in the mean number of pulses if one were to increase the pulse energy.

4.4 Discussion

I have shown that the pulse duration is a crucial component in establishing high membrane permeabilisation efficiency. Yet, crucially, a short pulse duration alone will not necessarily yield efficient membrane permeabilisation unless it is accompanied by sufficient pulse energy and number of pulses. The observed threshold-like behaviour when pulse duration is varied is particularly interesting as it demonstrates a clear change in behaviour, suggesting that two different mechanisms with significantly different dependencies on effective photon number are relevant for membrane permeabilisation.

The model proposed by Vogel *et al.* [137] and others [138] show that when operating in the high laser repetition rate regime (tens of MHz) and using tightly focussed femtosecond pulses, a low density free electron plasma is created which causes chemical decomposition of

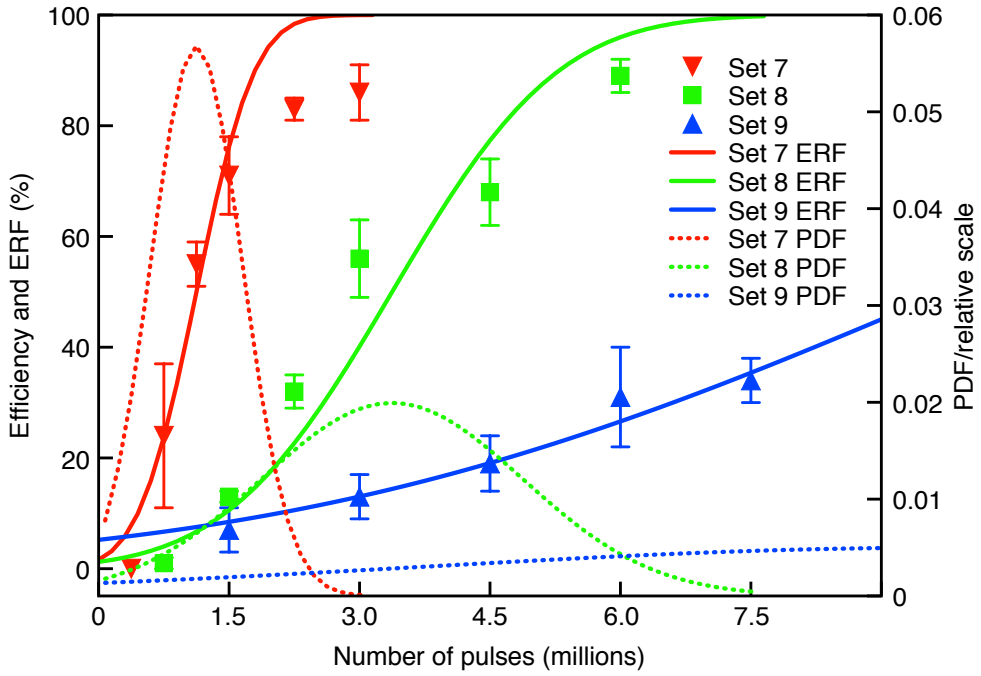

Figure 4.6: Optoinjection efficiency as function of number of pulses, again each data point represents the mean ± s.e.m. The solid line represents a cumulative density function in the form of a Gaussian error function (ERF) fitted to the data. The mean was obtained by regression fit of the linear part of the ERF, and the standard deviation was obtained from the probability density function (PDF) obtained by differentiating the ERF.

the molecules in the region of the focus. Alongside multiphoton-induced chemical changes, chemical bonds in the cell membrane are broken, hence leading to membrane permeabilisation without heating or thermo-elastic stress. The formation of the (quasi) free-electron low density plasma is initiated by multiphoton-ionisation and/or tunneling-ionisation. In solid dielectric media the threshold electric field required to change the ionisation mechanism from multiphoton to tunneling occurs at approximately 100 MV/cm [150]. However the relative roles of ionisation mechanisms requires further investigation [151].

Our findings support the fact that nonlinear absorption mechanisms are initially dominant at creating free electrons, with linear absorption mechanisms dominating once sufficient electron density is reached, leading to efficient membrane permeabilisation. The threshold-like behaviour indicates that efficient nonlinear absorption is required for efficient membrane permeabilisation. However, once the threshold is reached, typically at peak powers with magnitudes between 6-20 kW, the nonlinear processes saturate and the

linear absorption mechanisms dominate for efficient membrane permeabilisation. The creation of a low density free-electron plasma is essential to initiate the necessary chemical decomposition of cellular molecules. However, once the plasma reaches a critical density as a result of nonlinear processes, linear absorption becomes the dominant process. Similar mechanisms have been suggested and modelled for comparable pulse durations in dielectric ablation [152]. Nonlinear absorption changes the optical properties of transparent media and consequently increases the linear absorption cross-section at the near infrared wavelengths. Although linear absorption becomes the dominant mechanism above a threshold peak power, the nonlinear absorption is still likely to play a contributing role.

The pulse duration is a crucial factor to consider when using lasers in biological science. To effect the transient or permanent modification of biological material, nonlinear effects that cause photo-ionisation need to be initiated. High peak power ultrashort pulses maximise the nonlinear mechanisms that lead up to this modification. However, as demonstrated by our findings, the linear component is also essential for achieving substantial modification. Therefore to decrease the permanent damage that occurs, it is necessary to find the correct balance between the linear and nonlinear components of absorption. Through the use of ultrashort laser pulses the total energy required could be minimised by increasing the contribution of nonlinear absorption mechanisms by decreasing the pulse duration.

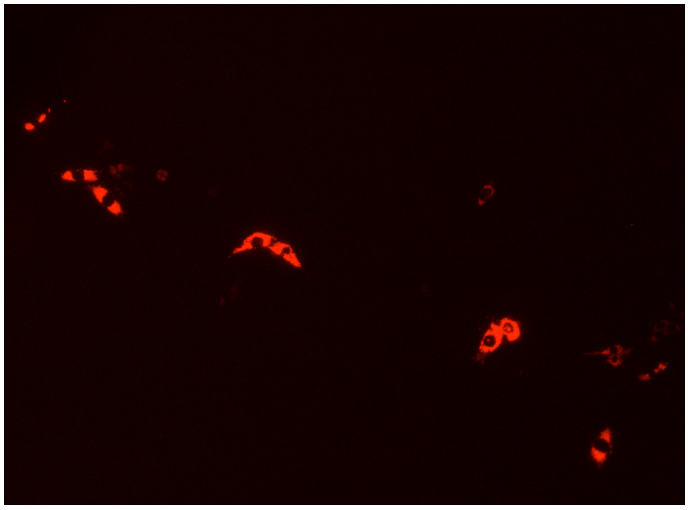

Figure 4.7: Example image of red fluorescing cells which were phototransfected with DS-RED plasmid for targeted expression of fluorescing protein within the mitochrondria using 12 fs pulses.

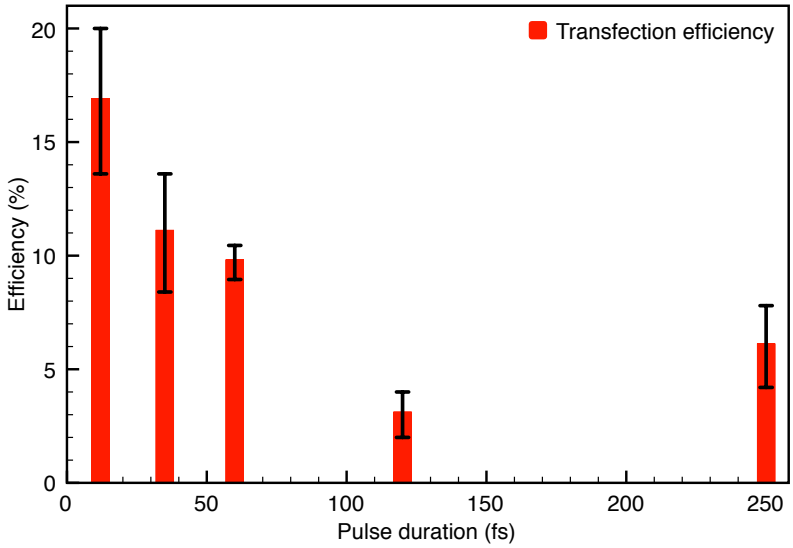

Figure 4.8: Uncorrected transfection efficiency as function of pulse duration (12, 35, 60, 120 and 250 fs).

4.5 Phototransfection experiments

Transfection experiments were carried out in a similar manner to the optoinjection studies using equivalent home-built optical microscope setups with the same objectives and utilising the ultrashort pulse Femtolaser system. The methods used are discussed in Appendix 7.4. Generally the process of phototransfection is poorly understood due to the relative unpredictability of the transfection process. One major question concerns the specific physical interactions and how the DNA is permitted through the membrane upon permeabilisation. Despite a significant devotion of time we did not obtain the level of statistical evidence (dish number, n=4; 50 cells per dish) necessary to make any strong statement about phototransfection as function of pulse duration. Fig. 4.7 shows an example population of cells transfected with DS-RED DNA plasmid, which encodes for targeted expression of red-fluorescing proteins inside the mitochondria. Fig. 4.8 shows the transfection efficiencies obtained as function of pulse duration. We repeated experiments at a multitude of laser parameters. In particular, we began with the standard parameter approach, which is to use a few tens of mWs and irradiate cells three times axially for 40 ms each. However we only obtained transfection in these experiments when using 20 mW average power for a duration of 2 ms was used to irradiate individual cells covering

5-7 axial irradiation events. Note, this graph could not be replicated and the procedure was unusual in comparison with the standard 40 ms duration and 3 axial shots used in previous literature [143, 145].

Clearly, no distinct relationship between transfection efficiency and pulse duration was found. It should be noted that with future work it should be possible to obtain more statistically significant results. It should further be noted that optoinjection experiments provide more consistent data because they are mostly dependent upon a physical response to the laser, whereas for transfection, the biological response is critical. It was not possible to obtain sufficiently consistent data such that a clear picture emerges in terms of laser pulse duration in optoinjection.

4.6 Conclusions

The nature of the coupling between pulse duration, pulse energy and number of pulses defines absorption characteristics of the cell membrane. We identify some key features of our findings which help to explain the processes leading to membrane permeabilisation and hence optoinjection.

(i) The absorption behaviour is initially dominated by multiple-effective photon numbers in the range 3.5-9.6. The equivalence of decreasing the pulse duration and increasing the pulse energy is apparent, as both parameter types initiate efficient optoinjection.

(ii) For peak powers in the range of 6-20 kW there is a behaviour transition, above which the multiphoton absorption transforms into near linear absorption.

(iii) Above the peak power threshold the multiphoton absorption saturates revealing the linear absorption as the dominant mechanism. Figs. 4.4 and 4.5 display this beahviour in the linear regimes of shorter pulse durations and higher pulse energies, respectively.

(iv) The number of pulses required to support efficient optoinjection for fixed pulse duration and energy must exceed a specified value, which was defined as 50 %. Only through appropriate selection of a high peak power parameter choice does the mean number of pulses decrease. This observation also supports the idea that the optoinjection process requires a high peak power initiation.

These findings complement the Vogel model of femtosecond optical absorption in biological material [137]. Importantly, the initial multiphoton absorption events lead to the avalanche creation of a quasi-free electron plasma at the focus, which may be supported by tunneling ionisation, inverse Bremsstrahlung and impact ionisation events. The threshold peak power defines a critical plasma density, which, once exceeded the linear absorption dominates leading to accumulation of energy, bringing about thermo-elastic stress along

with the simultaneous multiphoton-induced chemical breakdown near to the membrane, hence leading to permeabilisation.

To the best of our knowledge this work is the first experimental demonstration of the peak power threshold. Our findings demonstrate that careful selection of laser parameters will achieve efficient membrane permeabilisation and this has significant importance in laser-mediated drug and gene delivery. These findings also have implications for imaging and cell surgery using ultrashort pulses lasers as they describe the processes leading up to damage formation, which is not desirable for imaging, but is potentially desirable for cell surgery.

The optoinjection work in this chapter has been published in Nature Scientific Reports: 'Exploring the ultrashort pulse laser parameter space for membrane permeabilisation in mammalian cells', Andrew P. Rudhall, Maciej Antkowiak, Xanthi Tsampoula, Michael Mazilu, Nikolaus K. Metzger, Frank Gunn-Moore and Kishan Dholakia, Nat. Sci. Rep., **2**, 858, 2012.

4.7 Chapter acknowledgements

The author designed the experiments with advice from Maciej Antkowiak and Lani Torres. The author performed all experiments in this chapter. The author performed the data analysis with assistance from Maciej Antkowiak. Michael Mazilu assisted in providing fits for the experimental data.

Chapter 5

Advanced beam shaping with broadband ultrashort pulses

5.1 Introduction

The following chapter builds upon chapter 2 by examining some of the propagation characteristics of ultrashort pulses. Most specifically ultrashort pulse propagation is examined from a spatial light modulator computationally configured to display a grating pattern, which in the corresponding focal plane yields an interference pattern (beam spot) which contains spatio-temporal couplings. These spatio-temporal couplings can cause problems in terms of ultrashort pulse duration and spatial profile. In the present example, the SLM causes angular dispersion due to its grating display and broad spectral content of the ultrashort pulses. This chapter address how spatial modulation using a SLM can lead to novel beam propagation types. The ability to tailor ultrashort light pulses both spatially and temporally provides the possibility for application-specific light fields, for example, in biophotonics experiments, where an ultrashort pulse is required with different propagation characteristics such as a Bessel beam.

Since the introduction of pulsed lasers there has been remarkable progress concerning the pulse duration. In particular, the ability to generate sub-picosecond pulses heralded a new domain, often referred to as ultrashort pulses. Chapters 1 and 2 introduced the concept of moulding the pulses into any desired temporal shape by arbitrarily adjusting the spectral phase. The controllable formation of arbitrary pulse shapes provides new opportunities for the use of ultrashort pulses lasers. However a further degree of freedom exists, which determines the spatial characteristics of a beam. In the context of monochromatic light, it is possible to phase and/or amplitude modulate spatial zones of the beam to ac-

quire a desired pattern within a corresponding focal plane [7]. The most obvious examples of this type of spatial modulation is in novel beam shape generation, such as Bessel beam formation. In this case, a pattern such as an annulus yields the typical concentric ring pattern associated with Bessel beams.

In the context of ultrashort pulses, this phase and/or amplitude modulation of spatial aspects of the beam can, in addition to focal plane pattern formation, result in spectral phase modulations. The converse is also true, wherein the spectral phase and amplitude modulation may affect the spatial pattern formed at the focal plane. This type of interaction between spatial and spectral components is referred to as spatio-temporal coupling [102, 153]. The spatio-temporal couplings associated with ultrashort pulse result in beam shape distortions including spatial chirp (observed as a spread in phase across the wavefront), angular dispersion (resulting in spatial chirp, such as would be generated from a grating) and pulse front tilt (as would be generated from a prism), to name but a few. A more complete listing of first-order spatio-temporal couplings is found in [102, 153]. Note, the term temporal is correspondingly equivalent to the term spectral, wherein the phase and amplitude spectral information directly infers the temporal information through the associated Fourier transform, as discussed previously.

In this chapter I examine the ultrashort pulse beam profiles generated by different functions applied to a spatial light modulator placed the back aperture of a lens. In particular I generate Gaussian and Bessel beams and study the transverse beam profile, propagation and spectral phase of ultrashort pulses occurring in the focal plane. The use of the SLM opens up the opportunity of using spatial phase modulations to effect temporal modulation due to the associated spatio-temporal couplings.

5.1.1 Bessel beams

The main part of this study considers the use of Bessel beams. This type of beam has been studied extensively in the CW regime as well as a number of studies of polychromatic and/or ultrashort pulse Bessel beams [154, 155]. However, some studies have been concerned with applications of ultrashort pulsed Bessel beams, for example ultrashort pulse Bessel beam photoporation [145]. Nonetheless, novel beam shapes continue to fascinate due to their unique propagation characteristics and surprising properties.

The introduction of so-called diffraction-free beams, in particular those having a Bessel-like solution in 1987 provided an intriguing possibility of needle-like beams which may propagate over long distances compared with Gaussian equivalents [156,157]. Bessel beams of the zeroth order are characterised in the transverse plane by having a high intensity

circular core with a multitude of radially progressing concentric annuluses having progressively less intensity extending radially outwards from the central core; although an equal amount of energy can be contained within each ring [156]. It should be noted that ideally the Bessel beam could propagate in a diffraction-free manner, however in practice this is unachievable, as the ideal Bessel beam would require infinite energy to do so [156]. Therefore experimental implementations of the Bessel beam are usually referred to as quasi-Bessel beams. Throughout this chapter the term quasi is not used, but in all cases it is implied.

The equation used to describe the monochromatic Bessel beam electric field in the z-direction is one of the solutions of the wave equation, $\left(\nabla^2 - \mu_0\epsilon_0\frac{\partial^2}{\partial t^2}\right)E(\mathbf{r},t) = 0$ and is given by [158]

$$E(r,z) = AJ_0(\alpha r)\exp\left(-i\frac{2\pi f}{\lambda}\right)\exp\left(-i\frac{\pi\rho_a^2}{f\lambda}\right)\exp(-i\beta z), \tag{5.1}$$

where

$$A = i\frac{2\pi}{\lambda f}E_{\text{incident}}(\rho_a)\rho_a\Delta\rho, \tag{5.2}$$

$$\alpha = \frac{2\pi\rho_a}{\lambda f}, \tag{5.3}$$

$$\beta = \frac{2\pi}{\lambda} - \frac{\pi\rho_a^2}{\lambda f^2}, \tag{5.4}$$

for a monochromatic beam of wavelength λ, annular aperture radius ρ_a, annular aperture thickness $\Delta\rho$ with a lens of focal length f.

Bessel beams are usually generated in two ways. In the first case the Bessel beam can be generated by illuminating an annular aperture.. This type of configuration was used in the experiments presented in this chapter. The other solution is to use a conical lens, better known as an axicon. The axicon method is more light-efficient as no light is blocked, however axial intensity modulations appear as a result of the finite tip size of the axicon [159]. These are discussed in the context of ultrashort pulses below.

Bessel beams generated using broadband ultrashort pulses

The transverse spatial distribution associated with Bessel beams is wavelength dependent. Therefore in broadband Bessel beams each spectral component provides concentrically displaced rings, resulting in decreased concentric fringe visibility, as was shown theoretically [158]. In this study 10 fs beams were found to have slightly decreased fringe

visibility, while a 3 fs beam was found to have substantially decreased fringe visibility. An experimental demonstration of this decrease in fringe visibility was obtained using a micro-axicon array to generate a multitude of Bessel beams with various pulse durations [154]. Further, a programmable array of ultrashort pulsed needle-like beams was achieved using a SLM [160]. A marked change in fringe visibility was observed in [154] which was also observed in our experiments, for example, in Fig. 5.6, in which the beam was subject to angular dispersion in one direction. The generation of ultrashort pulse Bessel beams is often referred to as the so-called X-pulse formation in which the axial propagation has an apparent X-shaped transverse profile extending axially [161, 162]. However, in [162] the experimental realisations of the Bessel-X pulses were emphasised with the use of super-broadband emission from a Xe-arc lamp with a 3 fs correlation time. The possibility of generating so-called light bullets in which the propagation of a beam is transversally invariant and localised in time may be potentially realised in linear optics through the use Airy-Bessel beams [163].

5.2 Ultrashort pulse novel beams: studies

Various experiments were conducted involving a spatial light modulator in conjunction with the MIIPS pulse shaper. For the purposes of clarity this section introduces each separate experiment in more detail in subsections containing the related methods, results and discussion. A conclusion is presented after the experiments.

5.2.1 Experimental setup

In this section the experimental arrangements used are outlined for reference to the later sections in which different experiments are discussed. In the first instance, a single pass on the SLM was used and subsequently a double pass on the SLM was used (in order to compensate for spatial chirp). The single pass SLM version either used lenses or focusing mirrors. Fig. 5.1 illustrates the single-pass arrangement; Fig. 5.2 illustrates the double-pass arrangement. The single-pass arrangement was set up by expanding a beam to overfill the SLM display, which was oriented to match the input polarisation of the laser beam, and the reflected orders were imaged at a closed aperture. The SLM was modulated to show a grating, of which the first order was selected and passed through the aperture and subsequently imaged onto the camera. The arrangement for the double-pass arrangement was a little more involved. Firstly, the SLM display was split in two halves; and the beam was configured to slightly overfill one half of the SLM display. The first order was

imaged onto a mirror placed behind the aperture and the reflection directed towards the other half of the SLM display. The reflection from this half was collected by a mirror and subsequently imaged onto the camera. It should be first noted that in order to displace the second pass of the beam sufficiently it was necessary to transversely displace the beam as shown at f5 in Figure 5.2, wherein the beam passed through either side of the lens symmetrically so as to not introduce unwanted aberrations. it should be secondly noted that it was beneficial to use small optics (e.g. mirrors) in order to prevent blocking the beam inappropriately. The single-pass arrangement resulting in an extended transversal

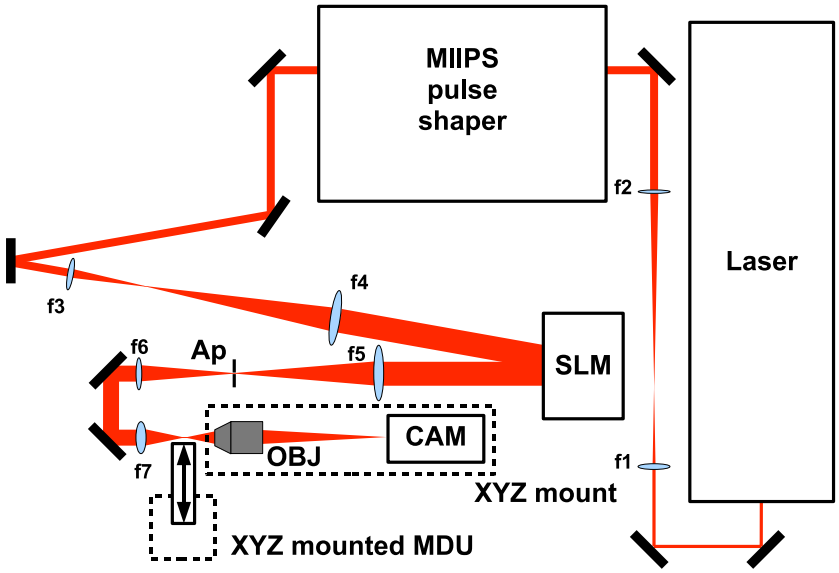

Figure 5.1: The initial experimental arrangement in which a single-pass arrangement is utilised; an equivalent setup is later used whereby focusing mirrors are used appropriately. SLM refers to spatial light modulator, Ap is an aperture, CAM is a camera (Basler Pi-A640-210GM) and MDU is the MIIPS detection unit outlined in chapter 4. Lenses f1 through f7 refer to 10 cm, 25 cm, 7.5 cm, 40 cm, 30 cm, 20 cm and 20 cm (interchanged with 5 cm) (image not to scale).

beam profile for Gaussian and Bessel beams due to the diffraction grating displayed by the SLM. It was found that the double-pass arrangement assisted in decreasing spatial chirp. This is discussed below.

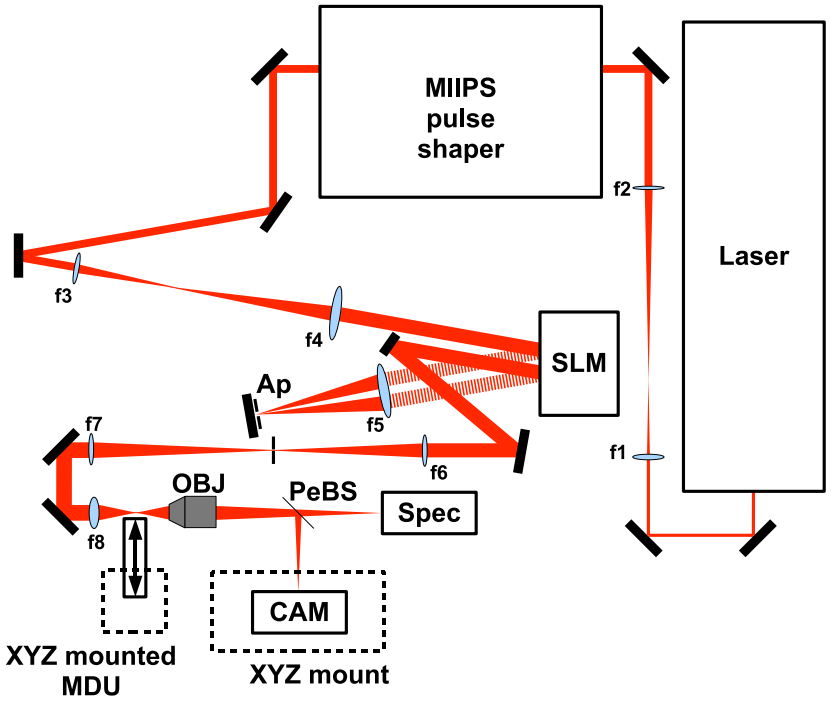

Figure 5.2: The experimental setup designed to take into account the geometrical dispersion introduced by the spatial light modulator, wherein the beam is back-reflected along a near-identical path, resulting in less spatial chirp. In addition to the elements of Fig. 5.1, Spec refers to the Ocean Optics fibre spectrometer USB4000 and PeBS refers to a 92:8 pellicle beam splitter (8% for the camera). Lenses f1 through f8 refer to focal lengths of 10 cm, 25 cm, 7.5 cm, 30 cm, 25 cm, 20 cm, 20 cm (interchanged with 5 cm).

5.2.2 Choice of lens for the focusing of ultrashort pulses

The choice of lens can be important for defining ultrashort pulse propagation. In particular it is important that the transverse beam components are refracted such that the time delay from each component to beam focus is identical. To test the effect of beam radius dispersion several differently sized annular apertures were created using the SLM, up to a maximum radius of 0.65 cm and focusing achieving using two different lens types (singlet and achromat) of equal focal length (5 cm). In principle an achromat does not have a radially dependent time delay [4] and further focuses all wavelengths in the same location [2]. In contrast a singlet lens cannot compensate for this radially dependent time delay, nor chromatic aberration either. The resulting discrepancy in the focusing of ultrashort light

pulses has been shown theoretically to provide pulse broadening in the focus [164]. The annular aperture radii used were: 0-1.6 mm (for Gaussian profiles), 1.6-3.2 mm (for Bessel profiles), 3.2-4.8 mm (for Bessel profiles), 4.8-6.4 mm (for Bessel profiles) and 0-6.4 mm (for Gaussian profiles). Note that the SLM was arranged in the aforementioned double-pass manner to control the angularly dispersive spectral components.

Lens choice: method and results

For each case the maximum SHG signal at the focus of the lens in question and performed the standard MIIPS analysis to retrieve the system dispersion. Each step was repeated at least ten times to minimise error in determining the system dispersion. In each case the difference in dispersion between each annular radius and the averaged radial dispersion (that is, Gaussian 0-6.4mm) was calculated. This way a direct comparison was made which demonstrated the small differences in dispersion that would not otherwise be shown if one were to examine the pulse shape from the *total* dispersion in each case. In Fig. 5.3 the singlet lens dispersion is shown. Importantly note the equivalent (frequency equivalent of wavelength) frequency width over which the difference is exactly zero (where the lines do not deviate from zero) is equivalent to $0.02 \times 10^{15}/s$, corresponding to a minimum sech-squared pulse duration of $\tau_{\text{min}} = 99$ fs. This is the minimum pulse duration obtainable that MIIPS can completely compensate using a singlet lens of 5 cm. In Fig. 5.4 the situation is improved when using the achromat. The angular frequency width is now equivalent to $0.07 \times 10^{15}/s$, corresponding to a minimum sech-squared pulse duration of $\tau_{\text{min}} = 28$ fs. The implication is that the achromat is ideal down to 28 fs whereas the singlet is ideal down to 99 fs for this focal length and annular radius.

The lens choice is critical for achieving a good quality MIIPS (or otherwise) compensation of spectral phase dispersion. The achromatic lens type was found to be preferable in that the radial dispersion profile was relatively flatter compared with the singlet lens type. Therefore in experiments involving the shortest pulses the best lenses should be chosen to suit the purpose, in particular paying attention to the radial time delay.

5.2.3 Spatial chirp

Spatial chirp arises when a spatially-dependent phase modulation is imparted upon spectral components of the beam [102]. Spatial chirp becomes particularly important for ultrashort pulses as it can mean that spectral content is converted into spatial content and vice versa. While spatial chirp can be useful, for example, in ultrashort pulse measurement or compensating for dispersion it must be compensated for so as to prevent unwanted beam

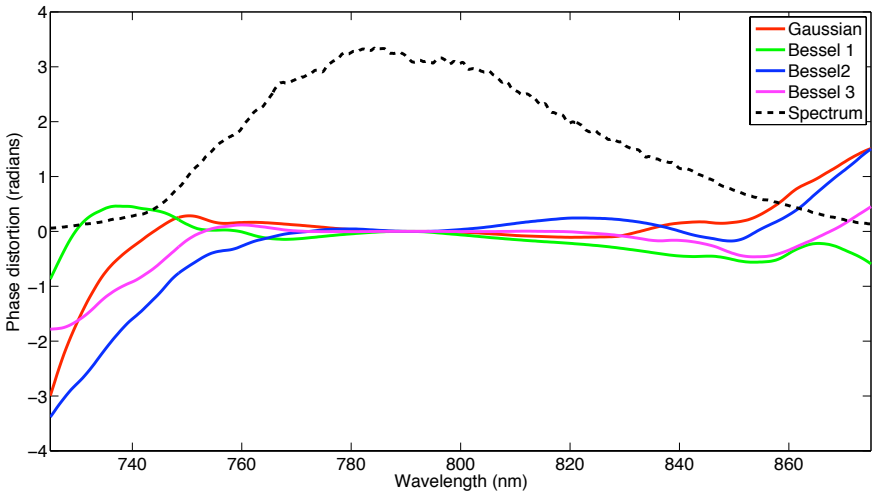

Figure 5.3: Spectral phase distortion differences for a 5 cm singlet lens. Graph showing relative phase distortions for (i) Gaussian beam of pre-lens radius 6.4 mm, (ii) Bessel 1 of pre-lens radius of 4.8-6.4 mm, (iii) Bessel 2 of pre-lens radius of 3.2-4.8 mm, Bessel 3 of pre-lens radius of 1.6-3.2 mm and the related spectrum.

distortion [165]. A feature of using a spatial light modulator for defining the desired beam shape is that a grating is displayed. A consequence of using the grating is the resulting wavelength-dependent angular dispersion according to the grating equation, hence resulting in spatial chirp. In the single-pass arrangement this manifests itself in terms of a spatial wavelength dependence in the focal plane which can not be eliminated. In this pattern the beam spot becomes elongated with wavelength, with a different spectrum as function of position. For this reason the pulse is no longer well defined in tight spot, instead by considering each spatial location the local spectral content defines the pulse duration. For this reason very little SHG was found due to the exceptionally long pulse duration and the associated spectral dispersion, which could not be compensated using MIIPS due to lack of SHG signal. Fig. 5.5 shows the fundamental spectrum as function of position for a Gaussian pulse with 80 nm bandwidth. The detector could not discriminate between tiny spatial locations, therefore the graph indicates a general tendency for the centre wavelength to shift with position. As a further demonstration of this effect an image of the spatial beam profile (Bessel) was recorded as function of spectral width. The Gaussian beam become elongated in the same fashion as the core of the Bessel beam. In this study, beams corresponding to CW, 25 nm and 80 nm were examined, as shown in Fig. 5.6. In the case of CW the beam the Bessel beam had the usual spatial profile, as expected.

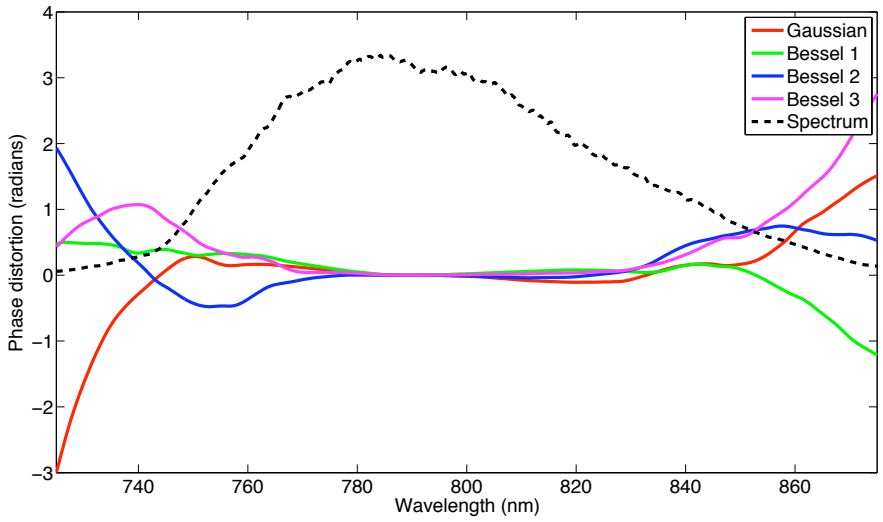

Figure 5.4: Spectral phase distortion differences for a 5 cm achromat lens. Graph showing relative phase distortions for (i) Gaussian beam of pre-lens radius 6.4 mm, (ii) Bessel 1 of pre-lens radius of 4.8-6.4 mm, (iii) Bessel 2 of pre-lens radius of 3.2-4.8 mm, Bessel 3 of pre-lens radius of 1.6-3.2 mm and the related spectrum.

However for 80 nm the Bessel beam is very distorted. Note the angle of 45 degrees is introduced by the grating being oriented at 45 degrees. The most important consequences were that no SHG could be generated in this arrangement, either for narrower or broader bandwidths due the lowered peak intensity. This is compounded by the fact that SHG is a 2-photon process, and further still, the spectral phase at these pulse durations plays a significant role. We did, however manage to correct for the angular dispersion by employing the double-pass arrangement shown previously in Fig. 5.2. In this setup the half of SLM area was imaged back to the opposite half and the transverse displacement achieved allowed the double-passed beam to be directed towards the detection setup. The transverse displacement was achieved by passing the beam initially through the left-hand side of a lens (introducing aberrations) and reflected through the corresponding right-hand side of the lens, thus compensating for the introduced aberrations. In this setup, the beam was sufficiently localised such that a sufficiently short fundamental pulse was defined and SHG could be generated, thus permitting MIIPS compensation. Fig. 5.7 shows the Bessel beam generated using this method (with a few minor aberrations). Importantly however, SHG signal could be collected this way. It would have been desirable to examine the fundamental and SHG beams as function of propagation distance however due to time constraints

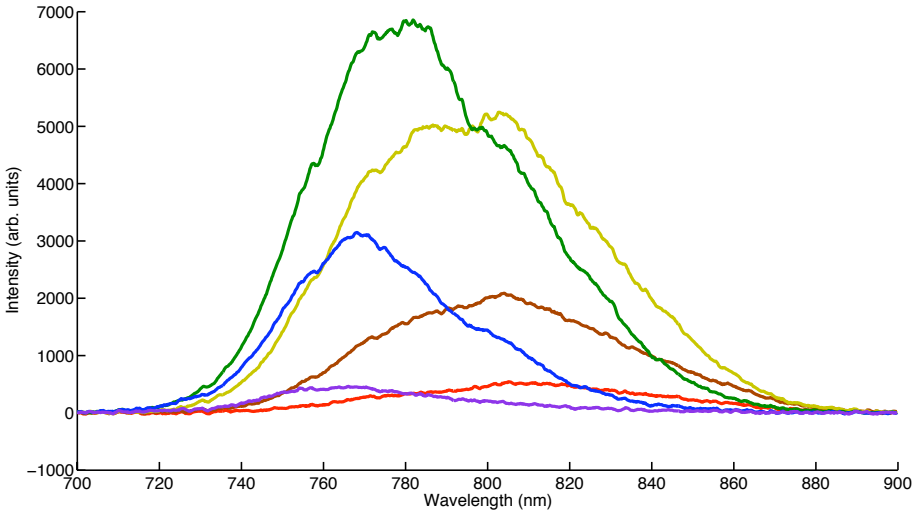

Figure 5.5: Spatial chirp demonstration with a spectrometer partially translated across the width of the beam in the SLM focal plane resulting in a position-dependent spectrum. Note the centre wavelength shifting to the left (going from red to violet in the usual sequence).

it was not possible to deal with some significant problems. For example, to collect the SHG the alignment needed to be perfect while translating along the beam propagation axis. While this concept is trivial, the implementation of such an arrangement was not. However, it should be noted that it should be possible to design a system as such. In a latter experimental arrangement the beam was imaged instead. This provide means for post-processing of the SHG data. However in this configuration the single-pass method was used and the spatial chirp prevented sufficient generation of SHG. A further problem is the need to completely eliminate the fundamental pulse from transmitting through the SHG filter. However these are all engineering problems that could be overcome in a future study.

5.2.4 Gaussian and Bessel beam propagation introduction

In the following set of experiments the axial propagation characteristics of Gaussian and Bessel beams of different bandwidths was examined. For a Gaussian beam the beam waist radius for a given wavelength at an input beam radius r_0 can be approximated as [44]

$$w_0 \approx \frac{f\lambda}{2r_0}, \tag{5.5}$$

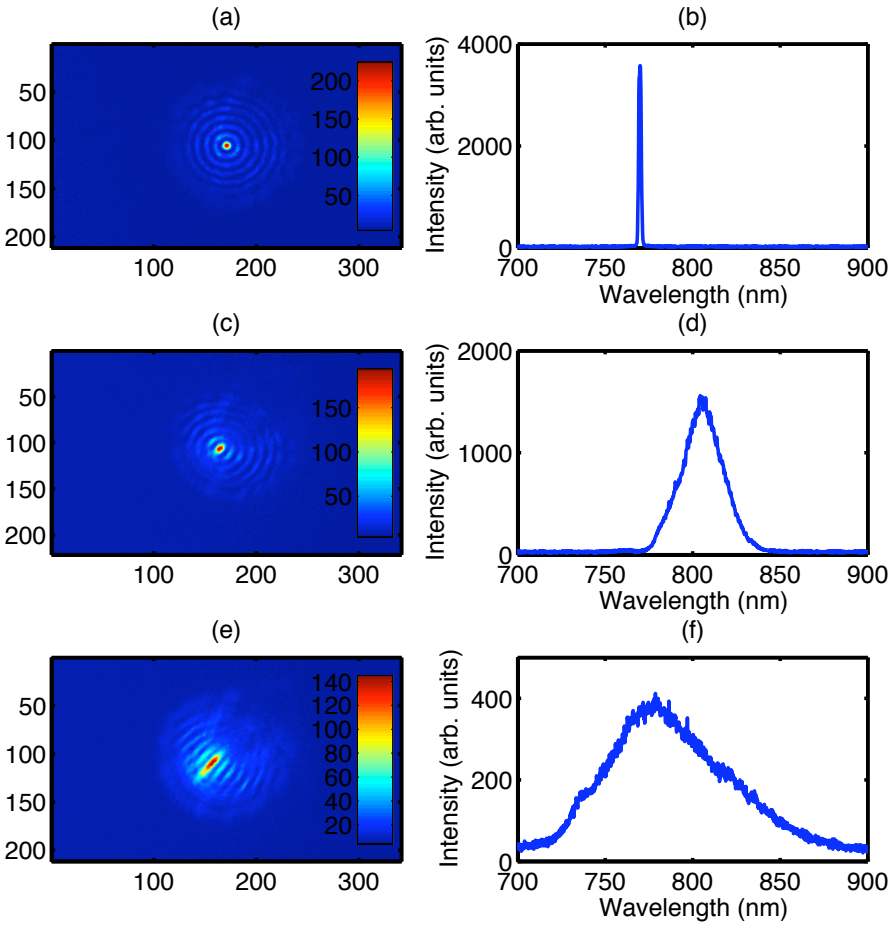

Figure 5.6: Angular frequency spread within Bessel beams; (a) corresponds to a Bessel beam generated by the CW spectrum indicated by (b); (c) corresponds to the equivalent Bessel beam but with 25 nm bandwidth indicated by spectrum (d); (e) corresponds to the equivalent Bessel beam as (a) and (c), but with 80 nm bandwidth, as seen in spectrum (f). The intensity scale clearly shows that the CW case exhibits the highest fundamental intensity (at constant average power) due to the spatial spread of the beam.

where the beam width convention used was 1/e. The beam propagation equation in the paraxial approximation is given by [44]

$$\nabla^2 \tilde{u}(x,y,z) - 2ik\frac{\partial \tilde{u}(x,y,z)}{\partial z} = 0, \tag{5.6}$$

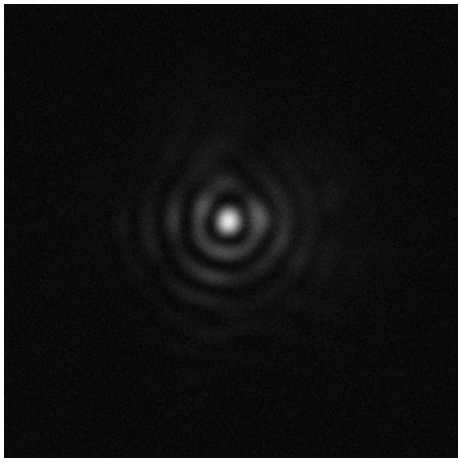

Figure 5.7: The Bessel beam generated with 80 nm bandwidth using the double-pass SLM arrangement.

where $\tilde{u}(x, y, z)$ is the slowly varying (in z) electric field amplitude in terms of cartesian coordinates. The equation used to model the propagation is one of the solutions of equation 5.6 and is given by [44]

$$\tilde{u}(x, y, z) = \left(\frac{2}{\pi}\right)^{1/2} \frac{\exp\left[-ikz + i\psi(z)\right]}{w(z)} \exp\left[-\frac{x^2 + y^2}{w^2(z)} - ik\frac{x^2 + y^2}{2R(z)}\right], \tag{5.7}$$

where the following expressions are used

$$w(z) = w_0\sqrt{1 + \left(\frac{z}{z_R}\right)^2}, \tag{5.8}$$

$$R(z) = z + \frac{z_R^2}{z}, \tag{5.9}$$

$$\psi(z) = \tan^{-1}\left(\frac{z}{z_R}\right), \tag{5.10}$$

$$z_R = \frac{\pi w_0^2}{\lambda}, \tag{5.11}$$

where w_0 is the beam waist radius in the focal plane, z is the axial position vector, z_R is the Rayleigh range (the range over which the beam radial width is less than $\sqrt{2}$ times that of the beam waist w_0, $R(z)$ is the radius of curvature of the propagating wavefront at position z and $\phi(z)$ is the Guoy phase shift. Equation 5.7 was used to model Gaussian beam propagation in the beam propagation experiments. The program was written in

MATLAB and is provided in the supplementary CD (acknowledged in Appendix 7.5). The following parameters were used to model propagation. The focal length was 20 cm, the small beam radius was 2.4 mm and the large beam radius was 5.0 mm. The beam width radius w_0 was calculated theoretically. Further, the multiple wavelength components were considered, each of which having a wavelength-dependent amplitude. Once taken into account these multiple wavelengths did not change the propagation length due; instead the central wavelength of 800 nm defined the propagation length.

Gaussian beam propagation

We measured the Gaussian beam propagation using the values outlined in Table 5.1 using the lens values outlined in Fig. 5.1 and analysed the axial intensity data. Fig. 5.8 refer to the measured propagation characteristics of an apertured Gaussian beams with 80 nm of bandwidth. Table 5.1 shows the calculated and measured propagation lengths

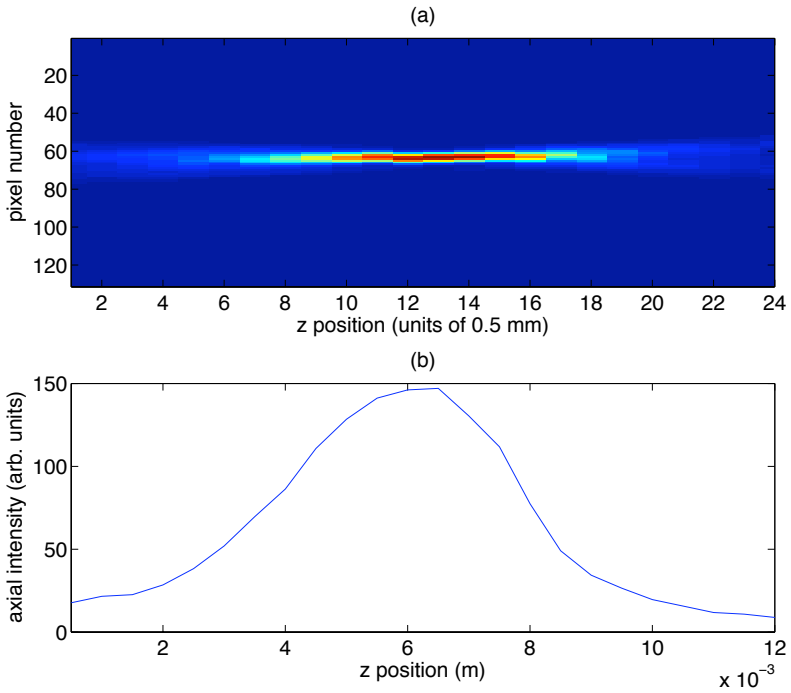

Figure 5.8: Top panel: colour-scaled propagation of a broadband Gaussian beam in the direction of beam propagation. Bottom panel: intensity cross section corresponding to above Gaussian beam.

for various-sized broadband (80 nm) and narrowband (25 nm) apertured Gaussian beams.

Figure number	bandwidth (NB or BB)	Disc size before lens (mm)	Calculated propagation length (mm)	Measured propagation length (mm)
N/A	NB	5.0	1.1	1.0
N/A	BB	5.0	1.1	1.0
N/A	NB	2.4	4.5	2.5
5.8	BB	2.4	4.5	2.5

Table 5.1: Comparison between propagation lengths for broadband (BB) and narrowband (NB) beams for different sizes circular aperture sizes (apertured Gaussian). Where calculated and measured propagation lengths differ slightly there may be errors e.g. incorrectly calculated apertured disc size due to the annular beam being distorted by virtue of pixel discontinuities on the SLM.

Not all images are shown to save space and are listed as N/A in the table. For some cases the calculated and theoretical values of Gaussian beam propagation length were in close agreement. Where the values were not in close agreement then the most likely explanation is due to assumptions made about e.g. beam size and aperture size. In experiments to determine the propagation length the beam width was not measured as the number of pixels covering this width were insufficient to provide accurate data.

Bessel beam propagation

The 2009 paper by Cižmár *et al.* provides an excellent reference to Bessel beams and has been referred to [159]. However the author has implemented relevant aspects of the paper but will not provide a full account. The most relevant equation for our purposes concerns the Bessel beam propagation as function of axial displacement, z. The axial electric field amplitude is given by

$$u(r=0,z) \propto \frac{\sin(bdz)}{z} \exp(iaz), \tag{5.12}$$

where

$$a = \frac{kf}{\sqrt{f^2+R^2}}, \tag{5.13}$$

$$b = \frac{aR}{2(f^2+R^2)}, \tag{5.14}$$

where R is the annular aperture radius, d is the thickness of the annular aperture and f is the lens focal length. Equation 5.12 was utilised in generating the calculated axial

intensity profiles below, wherein the field was multiplied by its corresponding complex conjugate. Equation 5.12 was further utilised to verify the Gaussian beam propagation model by setting the annular thickness d equal to the annular aperture radius R. The results were obtained were identical, with the Bessel equation resulting in very small axial oscillations.

In addition to the Gaussian measurement above we measured the Bessel beam propagation using the SLM values outlined in Table 5.2 using the lens values outlined in Fig. 5.1 and analysed the axial intensity data. Fig. 5.9 refers to the measured propagation characteristics of a Bessel beam with 80 nm of bandwidth. Table 5.2 shows the calculated

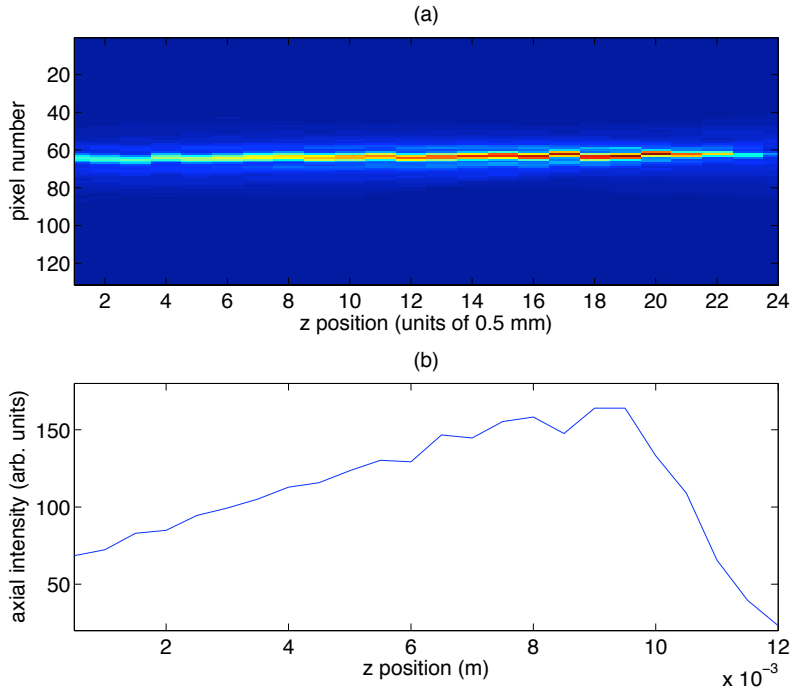

Figure 5.9: Top panel: colour-scaled propagation of a broadband Bessel beam in the direction of beam propagation. Bottom panel: intensity cross section corresponding to above Bessel beam.

and measured propagation lengths for various-sized broadband (80 nm) and narrowband (25 nm) Bessel beams. Not all images are shown to save space and are listed as N/A. In contrast with the Gaussian propagation, Bessel beams were measured to have a greater propagation length, as expected.

Figure number	bandwidth (NB or BB)	Annulus size before lens (mm)	Calculated propagation length (mm)	Measured propagation length (mm)
N/A	NB	4.6-5.0	13	4.5
N/A	NB	3.0-5.0**	2.7	4.5
N/A	NB	4.6-5.0	13	2.5
N/A	NB	3.0-5.0**	2.7	2.5
N/A	BB	2.0-2.4	28	4.0
N/A	BB	1.4-2.4**	11	4.0
5.9	BB	2.0-2.4	28	4.0
5.9	BB	1.4-2.4**	11	4.0

Table 5.2: Comparison between propagation lengths for broadband (BB) and narrowband (NB) beams for different annular sizes. Note, it is expected that the propagation lengths for broadband and narrowband should be very similar. In some case the comparison between calculated and measured values are similar; however in the cases that are different it should be noted that the theoretical calculations require a number of assumptions such as exact annular size, beam size and no diffractive effects. For the data marked with ** the measured annular radius value was used; in all other cases the expected annular size was used according to the exact experimental implementation (lenses/mirrors and SLM pixel size). This is because for very thin annular gratings displayed on the SLM the annular pattern obtained in the corresponding Fourier plane was generally smeared out, due to diffractive effects.

5.2.5 Concentric annular rings, their phase, and interference in the focal plane

One aspect of interest concerns the interference from individual spatial portions within the beam profile, as imaged from the SLM. In particular, portions of the SLM can be modulated to effect a change of phase of one spatial portion with respect to any other chosen spatial portion. As a result the interference pattern (beam focus) can be modulated such that the transverse intensity distribution within the beam focus may be significantly altered. In this way the effective chirp in one portion of the beam may potentially be changed.

Concentric annular ring interference: theory

A basic theory of the interference pattern in the focal plane, as provided by a circle surrounded by an annulus of varying phase is presented. It is firstly assumed that the peak electric field amplitude of the inner circle is equal to the outer circle. The inner electric field E_{inner} can be described by

$$E_{\text{inner}} = E\exp(-f(\omega) + i\phi(\omega))f(x,y,z), \tag{5.15}$$

where $f(\omega)$ is a general function describing the spectral electric field amplitude as function of frequency (e.g. a non-Gaussian distribution such as some asymmetric non-analytic function could be approximated by some unknown function $\exp(-(f(\omega))))$, $\phi(\omega)$ is the spectral phase and $f(x,y,z)$ is a general function describing the spatial beam profile (e.g. a Gaussian) in terms of cartesian coordinates x,y and z. The outer electric field is given by

$$E_{\text{outer}} = E\exp(-f(\omega) + i\phi(\omega) + i\Phi)f(x,y,z), \tag{5.16}$$

where Φ is the spectral phase imparted by the SLM. For simplicity it is initially assumed that Φ is constant, however this unduly complicates the point of this description. In practice the SLM imparts a different phase as function of wavelength and this may have contributed to deviations from theory, as reported later. The total field is provided by

$$E_{\text{sum}} = E_{\text{inner}} + E_{\text{outer}} = E(\exp(-f(\omega) + i\phi(\omega))\left[1 + \exp(i\Phi)\right]. \tag{5.17}$$

From equation 1.2 in Chapter 1 we can write the intensity as

$$I(\omega,\Phi,x,y,z) \propto \int_0^\infty E_{\text{sum}}E_{\text{sum}}^* d\omega, \tag{5.18}$$

where * denotes the complex conjugate and where the spatial aspects of the integer have been incorporated into the $\propto$ sign. We obtain

$$I(\omega, \Phi, x, y, z) \propto EE^*(1 + \exp(i\Phi))(1 + \exp(-i\Phi)), \tag{5.19}$$

where the integer relating to the frequency terms have been further incorporated into the proportionality term. Thus,

$$I(\omega, \Phi, x, y, z) \propto 4\cos^2(\Phi/2). \tag{5.20}$$

Hence, at any frequency and position, there is a cosine-squared relationship between intensity and SLM outer pattern phase. This results in an intensity modulation as function of phase. Therefore it should be possible to obtain near zero field at certain phases. Over a 2π range, the maxima intensities are obtained at $2m\pi$ for integer values of m. The minima intensities are obtained at $(2m + 1)\pi/2$ for integer values of m. To verify this a 2D Fourier transform model is provided for establishing the intensity for this particular case of interfering concentric annular components. The model does not take into account the wavelengths involved due to lack of knowledge of the mapping between frequency and position and so the broadband case is not described. However, this model is instructive for examining what happens when the spatial phase is changed. It should be emphasised that this model refers to monochromatic waves (as this is only allowed in the Fourier transform model). Therefore this model is indicative but not definitive. The MATLAB code for this model is provided in the supplementary CD and acknowledgements given in Appendix 7.5.

Figs. 5.10(a-d) show some of the computationally calculated beam spot resulting from interfering outer pattern with the inner pattern, whereby the phase difference of the outer pattern is varied continually from 0 to 2π, wherein four cases are selected including outer annulus phase of 0, $\pi/2$, π and $3\pi/2$. Note how the beam spot changes in shape significantly for varying phase. To accompany the fundamental beam spots the corresponding SHG beam spots were also calculated and are presented in Figs. 5.11(a-d). In the model 33 units of $\pi/16$ were used to cover phase values of 0 to 2π inclusively. Equation 5.20 shows that the fundamental intensity signal is oscillatory and positive. From the computational model the centre pixel values were recorded across the 33 units and the results are shown in Fig. 5.12. These calculations serve as an introduction to the experiments involving interference between concentric rings. Importantly, these experiments are indicative and do not consider broadband light, nor the spectral phase response of the SLM. Further, they are not scaled according to wavelength and actual beam profile. However

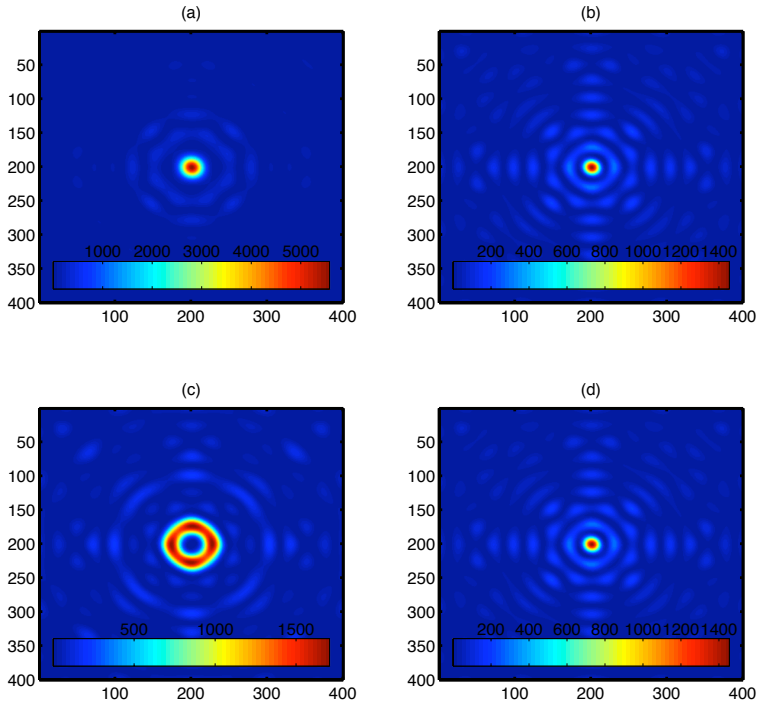

Figure 5.10: Calculated fundamental beam profiles for the following outer annular phase values: (a) 0, (b) $\pi/2$, (c) π and (d) $3\pi/2$. Note the significant change in beam shape. The full range of shapes can be calculated through use of the code in the supplementary CD. In each case the signal is not scaled absolutely, instead the scaling colours are evenly spread out using the obtained range of signal values. Actual values can be obtained from the aforementioned code.

they do indicate that a spectral intensity response can be expected for given relative phase difference between different spatial beam components.

Concentric annular ring interference: experiments

The phase was adjusted by displaying on the SLM an an outer annular pattern and a concentrically aligned inner Gaussian pattern. The resulting beam interference pattern at the focus of an achromat lens was imaged onto a CCD. The power of the outer and inner patterns was adjusted relatively so that when measured, the two-photon intensity response was similar whether using either the inner or outer pattern. The radius of the inner pattern before the focusing lens was 2.3 mm. The radius of the outer (annular)

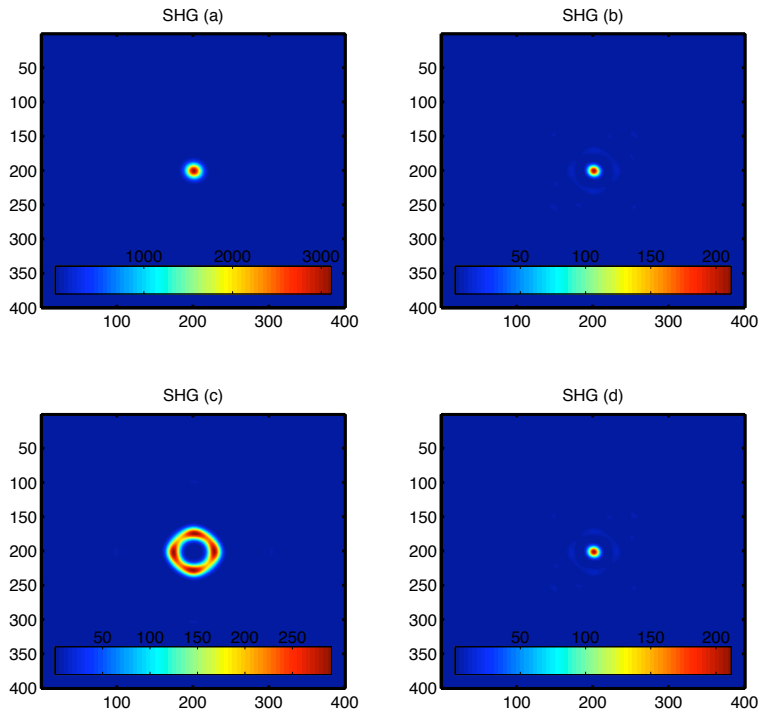

Figure 5.11: Calculated SHG beam profiles corresponding with Fig. 5.10 for the following outer annular phase values: (a) 0, (b) $\pi/2$, (c) π and (d) $3\pi/2$. Again, in each case the signal is not scaled absolutely.

pattern was 2.5-4 mm. The bandwidth of the laser used was 50 nm FWHM bandwidth, and was corrected by MIIPS to have a corresponding minimum pulse duration of 16 fs.

Fig. 5.13 demonstrates that the spectral content within the spatial distribution of the beam is constant, with the inner and outer patterns separately contributing to give the sum of the spectral content, as given when the inner and outer patterns were simultaneously displayed. Note that in Fig. 5.13 the spectrum is different to that of a compensated beam, where the spectrum is modulated by the MIIPS compensation function. Fig. 5.14 shows the uncompensated SHG obtained with the fundamental spectrum obtained in Fig. 5.13. By ensuring the SHG of the inner or outer pattern was constant, thus indicated that the peak intensity of the inner and outer pattern was similar, the beam spot size and corresponding axial intensity would be approximately the same. However at this point it should be noted that alternatively it may have been appropriate to calculate an

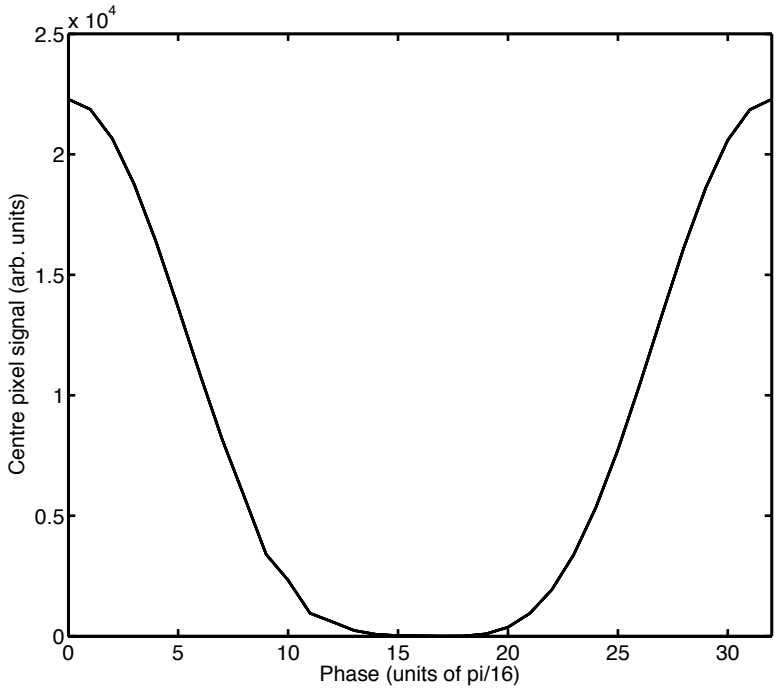

Figure 5.12: Calculated centre pixel fundamental signal for the range of phase units from 0 to 2π.

identically-valued electric field, however this would have required exact knowledge of the beam spot profile.

Next, the phase distortions obtained for the inner, outer and combined patterns were obtained. Firstly, Fig. 5.15 shows the relative spectral intensity obtained after the MIIPS compensation procedure, with the MIIPS-obtained correction applied. The phase distortions obtained from the inner, outer and combined patterns are shown in Fig. 5.16. Clearly there was quite a difference in dispersion when interfering the inner and outer patterns separately, with the sum of inner and outer pattern phase not corresponding with the phase obtained with the combined pattern.

Finally, the effect of changing the phase of the outer pattern with respect to the inner pattern using either 1, i, -1, or $-i$ modulation applied was considered. The phase of the inner pattern was kept constant with 1 being applied; the obtained spectra are shown in Fig. 5.17. The corresponding phase distortions, as obtained by MIIPS are shown in Fig. 5.18. The resulting relative SHG signal obtained is shown in Fig. 5.19

As a further experiment we varied the phase in 36 steps in units of $\pi/36$ from 0 to

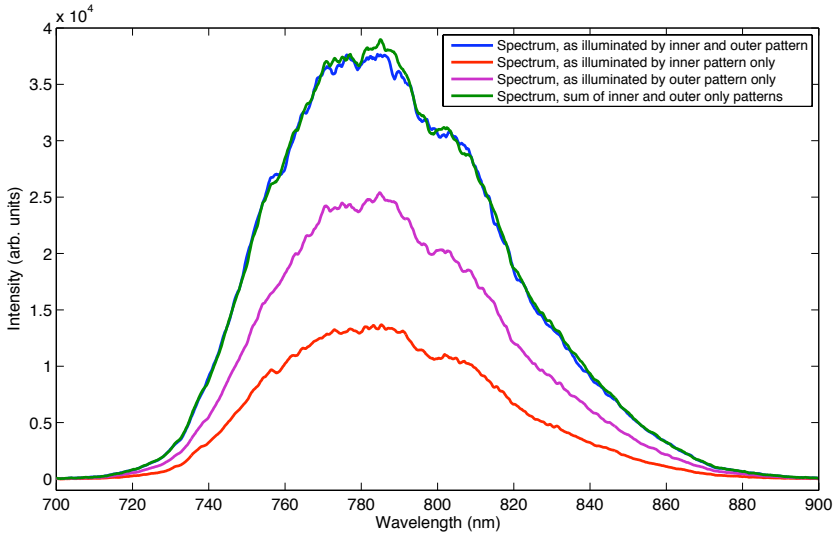

Figure 5.13: Spectral distribution (without MIIPS phase distortion correction) when illuminating with either inner and/or outer patterns on the SLM.

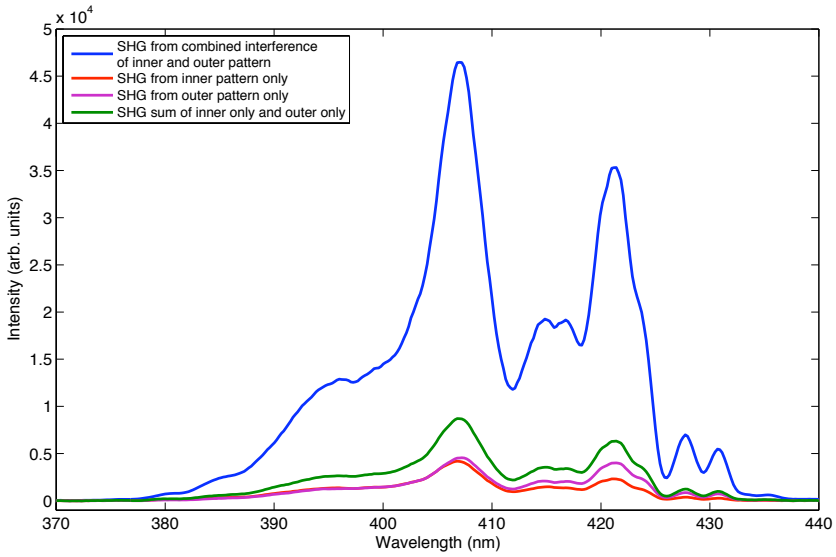

Figure 5.14: SHG distribution when uncompensated while illuminated with inner and/or outer patterns on the SLM. Note how sum of inner and outer patterns of SHG signal is, as expected, different from the combined interference of the inner and outer pattern.

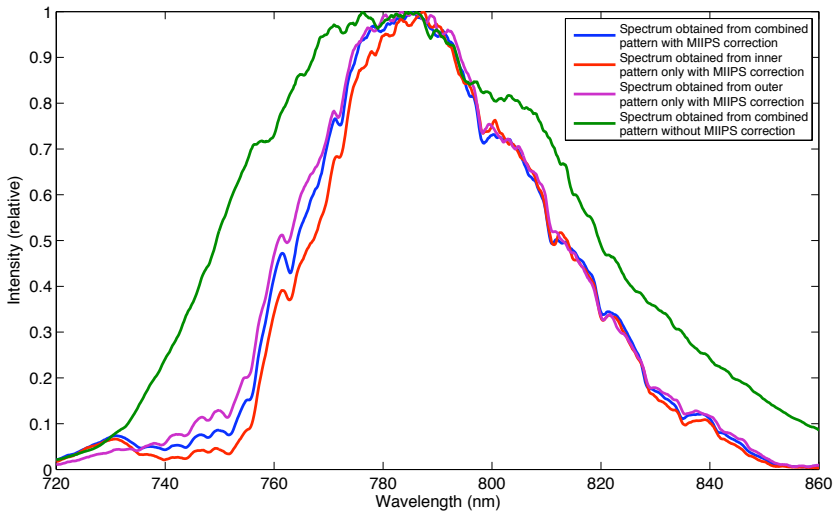

Figure 5.15: Measured spectra after MIIPS compensation function applied. Note the slight spectral difference between inner, outer, and combined patterns on SLM. Also note the spectral modification from uncompensated to compensated spectra.

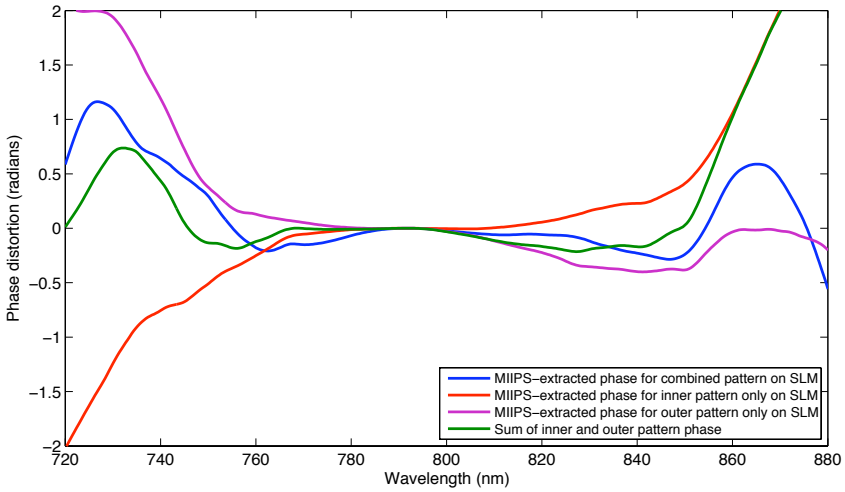

Figure 5.16: MIIPS-obtained phase distortion for the inner, outer, and combined patterns. Also shown is the sum of the inner and outer phase. In this case the outer pattern phase was kept at '1', or $\exp(0i)$, with the inner pattern phase being also kept at '1'.

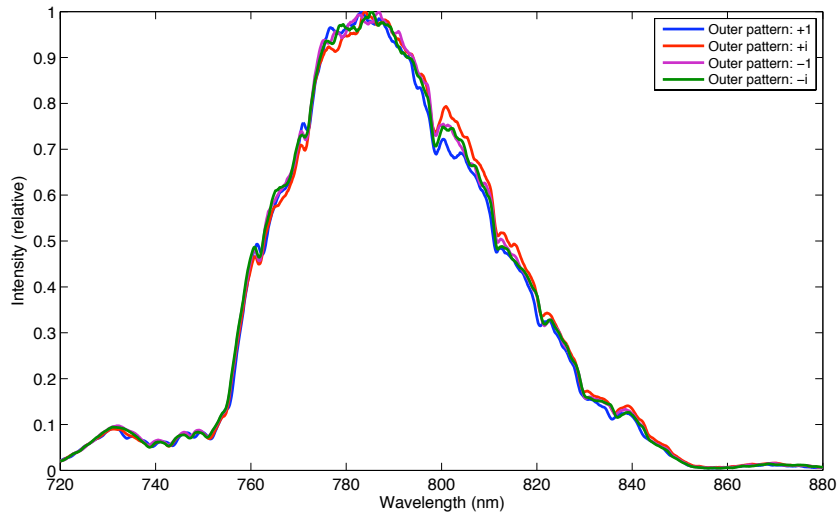

Figure 5.17: Relative spectra obtained with outer ring phase modulated by 1, i, -1, or $-i$.

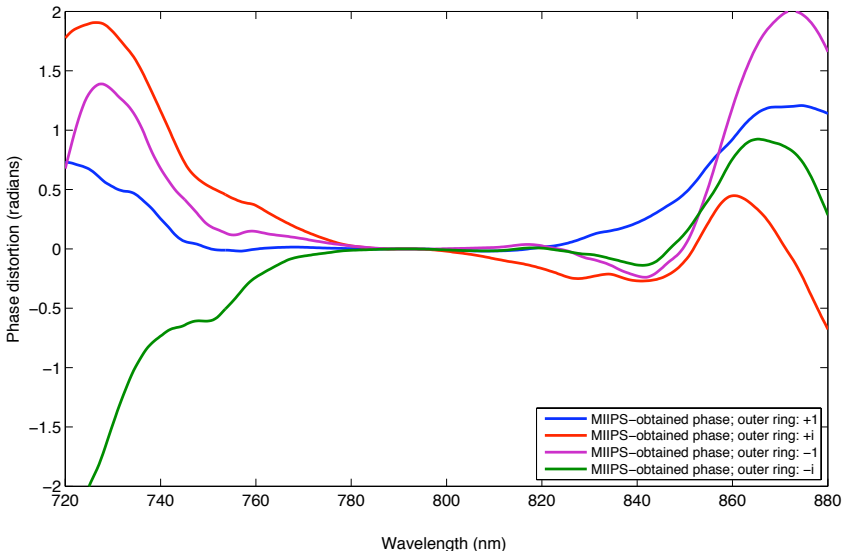

Figure 5.18: Phase distortions measured by MIIPS obtained with outer ring phase modulated by 1, i, -1, or $-i$.

2π to establish whether the results from theory could be replicated such as in Fig. 5.12. In the experiment we took the fundamental spectrum from the inner circle, concentric

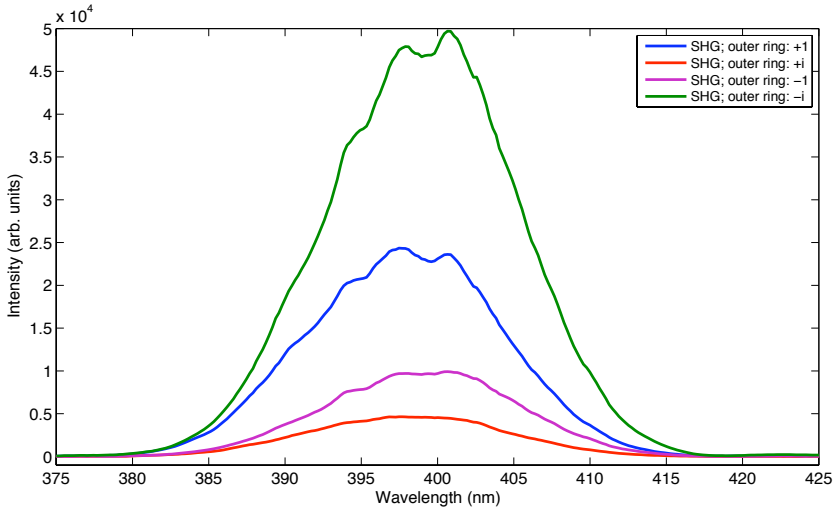

Figure 5.19: Measured SHG signal obtained with outer ring phase modulated by 1, i, -1, or $-i$.

outer ring and both combined in the series of phase steps as mentioned. If any intensity modulation were to occur then the expression $I_{\text{total}} = I_{\text{inner}} + I_{\text{outer}} + I_{\text{diff}}$ would hold, with I_{diff} being amount of modulation. In Fig. 5.12 several assumptions were made including examining only a tiny portion of the image plane, e.g. one pixel, and not the total signal, as was effectively measured in our experiments. It would be expected that the total signal would be constant as function of phase. It is possible that with the right settings a high dynamic range camera could pick up the single-pixel information. However, results from the aforementioned calculations showed that the cosine-relationship broke down if for example the annular ring was very small, or very large with respect to the central core. Owing to lack of conclusive results in this experiment (noise) the results are not presented, however a program as used to analyse the large sets of data in this experiment is included in the supplementary CD accompanying this thesis for future reference. It should be noted that the experiment concerned broadband light and not monochromatic light, as supported by the model. The SLM cannot impart constant phase as function of frequency, hence it is more difficult to obtain the results identified in the theory section. Nonetheless, should it be possible to obtain such results by applying constant phase overall a broadband range then such an experimental result may be realisable.

5.3 Conclusions

In this chapter the propagation characteristics of ultrashort pulse Gaussian and Bessel beams were examined, as generated by a SLM configured to provide these beam types. The SLM performs amplitude and phase modulation by displaying a grating, which has a wavelength dependent diffraction angle. As a result the broadband spectral components were angularly dispersed such that when imaged, the spatial beam profile was elongated, with transversally displaced spectral components. As a result the pulse duration was significantly lengthened due to lack of spectral content within one spatial location. Therefore SHG signal was minimal and as a result MIIPS compensation could not be conducted. We further examined the radial dispersion dependence of two lens types and found that radial dispersion within the system can have a significant impact of the pulse duration. We also examined the fringe visibility of ultrashort pulse Bessel beams. The wide spectral bandwidth associated with ultrashort pulses for Bessel beams means that the outer fringes are washed out due to overlapping spectral components in the spatial domain. In our experiments the angular dispersion distorted the results so it was not immediately clear whether the annular ring intensity was reduced. However on close inspect it is possible to make out 6 rings on the CW example and 4 concentric rings for the broadband example. We further found a way of correcting for the angular dispersion by spatially-displacing a the beam through a lens with a mirror for reflecting the beam and directing towards the opposite side of the lens for subsequent reflection from the SLM, thus compensating for some angular dispersion. We also examined concentric spatial annular zones, wherein concentric zones were interferes to provide an interference pattern in the focal plane which depended on the phase difference between spatial annular zones within the beam. The flexibility of the SLM-based beam shaping provides a multitude of opportunities for ultrashort pulse spatio-temporal manipulation with applications in all the natural sciences. Most importantly, it is possible to apply ultrashort beam propagation techniques for any of the aforementioned techniques listed. In particular a broadband Bessel beam could be used for effecting membrane permeabilisation without strict focusing requirements, while maintaining low overall dose in terms of pulse energy. This beam type may also be used for other light-matter experiments in which a broadband spectral width is required, for example in optical binding using ultrashort pulses, in which novel beams shapes may be useful.

5.4 Chapter acknowledgements

The author performed experiments and data analysis in this chapter with assistance from Svetlana Zolotovskaya. Further, Michael Mazilu and Tom Vettenburg provided different SLM programs.

Chapter 6

Conclusions and prospects for future work

The invention of ultrashort pulsed lasers has provided us with an important tool for probing light-matter interactions. Ultrashort pulses have a very high peak power for a given average power, which is particularly useful in situations requiring a nonlinear response. The time gap between the arrival of each ultrashort pulse may permit the dissipation of some of the energy accumulated in a given region irradiated by the laser, which helps to minimise damage caused by localised heating. This advantage is maximised with broadband ultrashort pulses, wherein the peak power may be substantially higher than for standard ultrashort pulses whereby the light-matter interaction may require less accumulation of energy, which may otherwise be translated into heat. However, broadband ultrashort pulses are susceptible to dispersion, which can significantly increase their pulse duration. Therefore, the use of broadband ultrashort pulses can be relatively restricted unless appropriate compensation means are employed. Many dispersion management techniques exist such as using prism pairs. However these dispersion management techniques are relatively inflexible and cannot compensate for arbitrary dispersion. I employed a dispersion measurement and compensation device for the purposes of dispersion compensation. The measurement technique is known as multiphoton intrapulse interference phase scan (MIIPS) and involves using a spatial light modulator (SLM) operating in the frequency domain in combination with performing SHG spectral measurements to obtain the dispersion profile of the optical system from output coupler to the plane of interest where the SHG measurements are performed in order to apply a compensation function onto the SLM to appropriately compensate for the optical system dispersion, thereby delivering transform-limited ultrashort pulses to the plane of interest.

In this thesis several inter-linked themes were considered. Dispersion-compensated broadband ultrashort pulses were generated and compensated using the MIIPS system and pulse shaper and were considered both experimentally and theoretically throughout this thesis. Firstly, transverse optical binding was considered. Under laser illumination, optically co-trapped particles may undergo additional forces due to the inter-particle light scattering. When under CW illumination the co-trapped particles may be subjected to oscillatory binding forces which are proportional to the wavelength in the host medium at different inter-particle separations. I initially observed the CW optical binding in an experimental setting and found that as expected, the perpendicular polarisation yielded greater binding forces than for the longitudinal polarisation. Further, the binding forces acted over a long separation range of up to around 15 wavelengths in the host medium, water. Further to this, a theoretical model for optically bound particle systems for broadband illumination was considered. In principle each of the spectral constituents provides a different binding force characteristic to that spectral component, resulting in the loss of the oscillatory nature of the binding forces. Instead, a smooth binding potential would be observed for a given inter-particle separation. It was found that for broadband pulses there was some decrease in binding force oscillations. For the case of SHG, optical binding required transform-limited pulses (for maximum SHG generation) in order to have similar decreases in binding oscillations.

I attempted to investigate the expected decrease in binding oscillation amplitude using a super-broadband supercontinuum laser source for the experimental studies. However the need to simultaneously image the particles and block a spectral covering the entire visible range prevented us from realising any experimental results. In the future this experiment may be achieved using a broadband source not covering the entire visible and near-infrared spectrum. Instead, a broadband laser covering several hundred nanometres of bandwidth may be sufficient to investigate the broadband binding effect providing a sufficient wide spectral window for imaging is provided. One possible solution, which at the time was not investigated, is imaging the experiment in reflection rather than in transmission. At the time this was not possible as a short focus (f = 3 cm) cylindrical lens was used however an objective in place of this lens with a weakly focussed cylindrical lens for illuminated the back aperture of said objective may provide means to permit imaging in reflection.

A further aspect to be considered in any future experiments is to perform a centre-of-mass intensity correction for particles imaged when in close proximity. When performing video-based tracking the particles are tracked by considering the peak intensity of light corresponding to the centre of the particle. When two particles are in close proximity they appear closer together than they really are due to spatial overlap of these central

intensities. A correction method has been implemented previously in which a moving particle is tracked relative to a single fixed particle and the data used to correct for two moving particles [166].

I performed optoinjection experiments upon cells using broadband ultrashort pulses with the appropriate laser parameters such that the cell membrane became permeabilised. In this study the laser parameters pulse duration, pulse energy and number of pulses were varied to examine the interplay between linear and nonlinear absorption processes leading up to cell membrane permeabilisation. I found that nonlinear absorption was crucial for initiating efficient cell membrane permeabilisation, with subsequent linear absorption processes also playing a crucial role in this. Importantly, both nonlinear and linear processes appear to be important in that one without the other was not effective. It would appear that a nonlinear initiation is required for bringing about free electron generation and avalanche creation, thereby increasing the initially low linear absorption cross section such that linear absorption is permitted. This process is necessary for permeabilisation of cell membranes and is likely to be of significance to other applications such as in cell nano-surgery.

The laser parameter space that could be explored is vast and is limited only by the significant time required to perform sufficient experiments for adequate statistical meaning. Furthermore, the parameter type could be widened to include wavelength, which would be particularly relevant for probing the multiphoton response of dyes and other molecules. From an application point of view, the lower number of pulses required for the shortest pulses may prove useful in high-throughput applications such as in microfluidics [167], wherein short irradiation times and low total cumulative dose are required. Furthermore, it would be highly desirable to examine the phototransfection pulse parameter space dependence however this is particularly challenging owing the unpredictability of the phototransfection process.

Finally, I examined the propagation characteristics of broadband ultrashort pulses using a SLM to create novel beam shapes, in particular a Bessel beam. I found that both Gaussian and Bessel beams were subject to angular dispersion resulting from interaction of the beam with the grating of the SLM. Consequently, the beams became elongated in the image planes due to the spatial spread of spectral components. Importantly, this meant that the pulse duration was also increased for any given spatial location within the beam focus and insufficient SHG was generated to provide MIIPS capabilities. SHG is key to the operation of the MIIPS system and MIIPS will not function without it. In one experiment I configured the setup into a double-pass SLM arrangement, thereby negating the issues with angular dispersion as this configuration compensated for such

dispersion. In this configuration SHG was obtained and used for MIIPS experiments. I demonstrated that the radial dependence of dispersion from a lens has a significant effect upon laser pulse duration. Most notably an achromatic lens provides a more consistent radial dispersion profile compared with a singlet lens. Furthermore, concentric annular zones were interfered together to examine the interference pattern in the focal plane of the lens for different relative phase relationships between the respective annular zones. I did not find the expected relationship, however with further work this should be achievable in the future.

Due to time constraints it was not possible to continue these experiments further. Nonetheless I have demonstrated the use of dispersion-compensated ultrashort pulses in a variety of topics. In particular I note that the SHG propagation characteristics could be obtained in a well designed system. For example, the SHG signal could be better detected using a camera to perform localised detection in the beam focal plane as the camera is translated along the beam.

Novel ultrashort pulsed beams have a multitude of potential applications, not least in the other topics in this thesis. For example, a broadband ultrashort pulsed Bessel beam could be used for cell membrane permeabilisation to obviate the stringent focussing requirements. The higher peak power afforded by broadband ultrashort pulses would compensate for the lower power density in the central core of the Bessel beam. Furthermore, the Bessel beam could be used in a longitudinal optical binding arrangement, or even the beam could spatially chirped with the potential for varying spatial binding periodicity along the full extent of the beam. Looking ahead it may be possible to create novel ultrashort beam shapes which can be shaped in four dimensions to provide tailored pulse and beam profiles, as provided by the spatio-temporal coupling of ultrashort pulses.

Bibliography

[1] F. Gires and P. Tournois. Interferometre utilisable pour la compression d'impulsions lumineuses modulees en frequence. *CR Acad. Sci. Paris*, **258**:6112–6115, 1964.

[2] E. Hecht. *Optics.* Pearson Education Inc., 4th edition, 2006.

[3] D.J. Richardson, J. Nilsson, and W.A. Clarkson. High power fiber lasers: Current status and future perspectives. *J. Opt. Soc. Am B*, **27**:110B63(1–30), 2010.

[4] J.-C. Diels and W. Rudolph. *Ultrashort Laser Pulse Phenomena.* Academic Press, 1st edition, 1996.

[5] K.L. Sala, G.A. Kenney-Wallace, and G.E. Hall. CW autocorrelation measurements of picosecond laser pulses. *IEEE J. Quantum Electron.*, **16**:990–996, 1980.

[6] R.W. Boyd. *Nonlinear optics.* Academic Press, 3rd edition, 2008.

[7] M. Born and E. Wolf. *Principles of Optics.* Cambridge University Press, 7th edition, 1999.

[8] K. Riley, M. Hobson, and S. Bence. *Mathematical methods for physics and engineering.* Cambridge University Press, 2nd edition, 2002.

[9] J.W. Cooley and J.W. Tukey. An algorithm for the machine computation of the complex Fourier series. *Math. Comput.*, **19**:297–301, 1965.

[10] J.D. Jackson. *Classical electrodynamics.* John Wiley & Sons, Inc., 3rd edition, 1999.

[11] I. Pastirk, X. Zhu, R.M. Martin, and M. Dantus. Remote characterization and dispersion compensation of amplified shaped femtosecond pulses using miips. *Opt. Express*, **14**:8885–8889, 2006.

[12] G.K. Woodgate. *Elementary atomic structure.* Oxford University Press, 2nd edition, 1980.

[13] I. Walmsley, L. Waxer, and C. Dorrer. The role of dispersion in ultrafast optics. *Rev. Sci. Instrum.*, **72**:1–29, 2001.

[14] S. Backus, C.G. Durfee III, M.M. Murnane, and H.C. Kapteyn. High power ultrafast lasers. *Rev. Sci. Instrum.*, **69**:1207–1223, 1998.

[15] F. Salin. Dispersion compensation for femtosecond pulses using high-index prisms. *J. Appl. Phys.*, **61**:4736–4739, 1987.

[16] R.L. Fork, O.E. Martinez, and J.P Gordon. Negative dispersion using pairs of prisms. *Opt. Lett.*, **9**:150–152, 1984.

[17] P. Xi, Y. Andegeko, D. Pestov, V.V. Lozovoy, and M. Dantus. Two-photon imaging using adaptive phase compensated ultrashort laser pulses. *J. Biomed. Opt.*, **14**:014002, 2009.

[18] A. Uchugonova, K. König, R. Bueckle, A. Isemann, and G. Tempea. Targeted transfection of stem cells with sub-20 femtosecond laser pulses. *Opt. Express*, **16**:9357–9364, 2008.

[19] M. Müller, J. Squier, R. Wolleschensky, U. Simon, and G.J. Brakenhoff. Dispersion pre-compensation of 15 femtosecond optical pulses for high-numerical-aperture objectives. *J. Microscopy*, **191**:141–150, 1998.

[20] P.A. Franken, A.E. Hill, C.W. Peters, and G. Weinreich. Generation of optical harmonics. *Phys. Rev. Lett.*, **7**:118–120, 1961.

[21] D.N. Nikogosyan. *Nonlinear optical crystals: A complete survey.* Springer, 1st edition, 2005.

[22] J.E. Sipe, D.J. Moss, and H.M. van Driel. Phenomenological theory of optical second- and third-harmonic generation from cubic centrosymmetric crystals. *Phys. Rev. B*, **35**:1129–1141, 1987.

[23] T. Stehlin, M. Feller, P. Guyot-Sionnest, and Y.R. Shen. Optical second-harmonic generation as a surface probe for noncentrosymmetric media. *Opt. Lett.*, **13**:389–39, 1988.

[24] G.J. Ashwell, G. Jefferies, D.G. Hamilton, D.E. Lynch, M.P.S. Roberts, G.S. Bahra, and C.R. Brown. Strong second-harmonic generation from centrosymmetric dyes. *Nature*, **375**:385–387, 1995.

[25] G.D. Boyd and D.A. Kleinman. Parametric interaction of focused Gaussian light beams. *J. Appl. Phys.*, **39**:3597–3639, 1968.

[26] D.A. Kleinman. Theory of second harmonic generation of light. *Phys. Rev.*, **128**:1761–1775, 1962.

[27] E. Sidick, A. Knoesen, and A. Dienes. Ultrashort-pulse second-harmonic generation. I. Transform-limited fundamental pulses. *J. Opt. Soc. Am. B*, **12**:1704–1712, 1995.

[28] E. Sidick, A. Dienes, and A. Knoesen. Ultrashort-pulse second-harmonic generation. II. Non-transform-limited fundamental pulses. *J. Opt. Soc. Am. B*, **12**:1713–1722, 1995.

[29] D.N. Fittinghoff, J.A. Squier, C.P.J. Barty, J.N. Sweetser, R. Trebino, and M. Müller. Collinear type II second-harmonic-generation frequency-resolved optical gating for use with high-numerical-aperture objectives. *Opt. Lett.*, **23**:1046–1048, 1998.

[30] H. Wang and A.M. Weiner. Efficiency of short-pulse type-I second harmonic generation with simultaneous spatial walk-off, temporal walk-off, and pump depletion. *IEEE J. Quantum Electron.*, **39**:1600–1618, 2003.

[31] W.H. Glenn. Second-harmonic generation by picosecond optical pulses. *IEEE J. Quantum Electron.*, **5**:284–290, 1969.

[32] A.M. Weiner. Effect of group velocity mismatch on the measurement of ultrashort optical pulses via second harmonic generation. *IEEE J. Quantum Electron.*, **19**:1276–1283, 1983.

[33] J. Comly and E. Garmire. Second harmonic generation from short pulses. *Appl. Phys. Lett.*, **12**:7–9, 1968.

[34] S.M. Saltiel, K. Koynov, B. Agate, and W. Sibbett. Second-harmonic generation with focused beams under conditions of large group-velocity mismatch. *J. Opt. Soc. Am. B*, **21**:591–598, 2004.

[35] T.R. Zhang, H.R. Choo, and M.C. Downer. Phase and group velocity matching for second harmonic generation of femtosecond pulses. *Appl. Opt.*, **29**:3927–3933, 1990.

[36] D. Meshulach, Y. Barad, and Y. Silberberg. Measurement of ultrashort optical pulses by third-harmonic generation. *J. Opt. Soc. Am. B*, **14**:2122–2125, 1997.

[37] P.E. Powers. *Fundamentals of nonlinear optics*. CRC Press, 1st edition, 2011.

[38] A.V. Smith. SNLO, 2013. SNLO nonlinear optics code available from A.V. Smith, AS-Photonics, Albuquerque. NM.

[39] O.E. Martinez. Achromatic phase matching for second harmonic generation of femtosecond pulses. *IEEE J. Quant. Electron.*, **25**:2464–2468, 1989.

[40] A.M. Schober, M. Charbonneau-Lefort, and M.M. Fejer. Broadband quasi-phase-matched second-harmonic generation of ultrashort optical pulses with spectral angular dispersion. *J. Opt. Soc. Am. B*, **22**:1699–1713, 2005.

[41] G. Steinmeyer, D.H. Sutter, L. Gallmann, N. Matuschek, and U. Keller. Frontiers in ultrashort pulse generation: Pushing the limits in linear and nonlinear optics. *Science*, **286**:1507–1512, 1999.

[42] P.F. Moulton. Spectroscopic and laser characteristics of Ti:Al_2O_3. *J. Opt. Soc. Am. B*, **3**:125–133, 1986.

[43] R. Ell, U. Morgner, F. X. K AÂrtner, J. G. Fujimoto, E. P. Ippen, V. Scheuer, G. Angelow, T. Tschudi, M. J. Lederer, A. Boiko, and B. Luther-Davies. Generation of 5-fs pulses and octave-spanning spectra directly from a ti:sapphire laser. *Opt. Lett.*, **26**(6):373–375, 2001.

[44] A.E. Siegman. *Lasers.* University Science Books, 1st edition, 1986.

[45] C.E. Byvik and A.M. Buoncristiani. Analysis of vibronic transitions in Titanium doped Sapphire using the temperature of the fluorescence spectra. *IEEE J. Quantum Electron.*, **21**:1619–1624, 1985.

[46] G. Steinmeyer. A review of ultrafast optics and optoelectronics. *J. Opt. A: Pure Appl. Opt.*, **5**:1–15, 2003.

[47] D.E. Spence, P.N. Kean, and W. Sibbett. 60-fsec pulse generation from a self-mode-locked Ti:sapphire laser. *Opt. Lett.*, **16**:42–44, 1991.

[48] C. Spielmann, P.F. Curley, T. Brabec, and F. Krausz. Ultrabroadband femtosecond lasers. *IEEE J. Quantum Electron.*, **30**:1100 –1114, apr 1994.

[49] R. Szipöcs, K. Ferencz, C. Spielmann, and F. Krausz. Chirped multilayer coatings for broadband dispersion control in femtosecond lasers. *Opt. Lett.*, **19**:201–203, 1994.

[50] A. Stingl, M. Lenzner, Ch. Spielmann, and F. Krausz. Sub-10-fs mirror-dispersion-controlled Ti:sapphire laser. *Opt. Lett.*, **20**:602–604, 1995.

[51] D.H. Sutter, L. Gallmann, N. Matuschek, F. Morier-Genoud, V. Scheuer, G. Angelow, T. Tschudi, G. Steinmeyer, and U. Keller. Sub-6-fs pulses from a SESAM-assisted Kerr-lens modelocked Ti:sapphire laser: at the frontiers of ultrashort pulse generation. *Appl. Phys. B*, **70**:S(5–12), 2000.

[52] V.V. Lozovoy, I. Pastirk, and M. Dantus. Multiphoton intrapulse interference. IV. Ultrashort laser pulse spectral phase characterization and compensation. *Opt. Lett.*, **29**:775–777, 2004.

[53] S. Akturk, X. Gu, M. Kimmel, and R. Trebino. Extremely simple single-prism ultrashort-pulse compressor. *Opt. Express*, **14**:10101–10108, 2006.

[54] O.E. Martinez. Grating and prism compressors in the case of finite beam size. *J. Opt. Soc. Am. B*, **7**:929–934, 1986.

[55] E.B. Treacy. Optical pulse compression with diffraction gratings. *IEEE J. Quantum Electron.*, **5**:454–458, 1969.

[56] A.M. Weiner, J.P Heritage, and E.M. Kirschner. High-resolution femtosecond pulse shaping. *J. Opt. Soc. AM. B*, **5**:1563–1572, 1988.

[57] J. Zhou, C.-P. Huang, C. SHi, M.M. Murnane, and H.C. Kapteyn. Generation of 21-fs millijoule-energy pulses by use of Ti:sapphire. *Opt. Lett.*, **19**:126–128, 1994.

[58] R.L. Fork, C.H. Brito Cruz, P.C. Becker, and C.V. Shank. Compression of optical pulses to six femtoseconds by using cubic phase compensation. *Opt. Lett.*, **12**:483–485, 1987.

[59] V.K. Chauhan, J. Cohen, P.M. Vaughan, P. Bowlan, and R. Trebino. Distortion-free single-prism/grating ultrashort laser pulse compressor. *IEEE J. Quantum Electron.*, **46**:1726–1730, 2010.

[60] U. Morgner, F.X. Kärtner, S.H. Cho, Y. Chen, H.A. Haus, J.G. Fujimoto, and E.P.Ippen. Sub-two-cycle pulses from a Kerr-lens mode-locked Ti:sapphire laser. *Opt. Lett.*, **24**:411–413, 1999.

[61] F.X. Kärtner, U. Morgner, R. Ell, T. Schibli, J.G. Fujimoto, E.P. Ippen, V. Scheuer, G. Angelow, and T. Tschudi. Ultrabroadband double-chirped mirror pairs for generation of octave spectra. *J. Opt. Soc. Am. B*, **18**:882–885, 2001.

[62] M. Nisoli, S. De Silvestri, O. Svelto, R. Szipöcs, K. Ferencz, Ch. Spielmann, S. Sartania, and F. Krausz. Compression of high-energy laser pulses below 5 fs. *Opt. Lett.*, **22**:522–524, 1997.

[63] N. Matuschek, F.X. Kärtner, and U. Keller. Theory of double-chirped mirrors. *IEEE J. Sel Top. Quant.*, **4**:197–208, 1998.

[64] B. Golubovic, R.R. Austin, M.K. Steiner-Shepard, M.K. Reed, S.A. Diddams, D.J. Jones, and A.G. Van Engen. Double Gires-Tournois interferometer negative-dispersion mirrors for use in tunable mode-locked lasers. *Opt. Lett.*, **25**:275–277, 2000.

[65] R. Szipöcs, A. Köházi-Kis, S. Lakó, P. Apai, A.P. Kovács, G. DeBell, L. Mott, A.W. Louderback, A.V. Tikhonravov, and M.K. Trubetskov. Negative dispersion mirrors for dispersion control in femtosecond lasers: chirped dielectric mirrors and multi-cavity Gires-Tournois interferometers. *Appl. Phys. B*, 70:S(51–57), 2000.

[66] F.X. Kärtner, N. Matuschek, T. Schibili, U. Keller, H.A. Haus, C. Heine, R. Morf, V. Scheuer, M. Tilsch, and T. Tschudi. Design and fabrication of double-chirped mirrors. *Opt. Lett.*, **22**:831–833, 1997.

[67] C.W. Hillegas, J.X. Tull, D. Goswami, D. Strickland, and W.S. Warren. Femtosecond laser pulse shaping by use of microsecond radio-frequency pulses. *Opt. Lett.*, **19**:737–739, 1994.

[68] M.A. Dugan, J.X. Tull, and W.S. Warren. High-resolution acousto-optic shaping of unamplified and amplified femtosecond laser pulses. *J. Opt. Soc. Am. B*, **14**:2348–2358, 1997.

[69] A.M. Weiner. Femtosecond pulse shaping using spatial light modulators. *Rev. Sci. Instrum.*, **71**:1929–1960, 2000.

[70] E. Zeek, K. Maginnis, S. Backus, U. Russek, M. Murnane, G. Mourou, H. Kapteyn, and G. Vdovin. Pulse compression by use of deformable mirrors. *Opt. Lett.*, **24**:493–495, 1999.

[71] N.K. Metzger, W. Lubeigt, D. Burns, M. Griffith, L. Laycock, A.A. Lagatsky, C.T.A. Brown, and W. Sibbett. Ultrashort-pulse laser with an intracavity phase shaping element. *Opt. Express*, **18**:8123–8134, 2010.

[72] C. Dorrer, F. Salin, F. Verluise, and J.P. Huignard. Programmable phase control of femtosecond pulses by use of a nonpixelated spatial light modulator. *Opt. Lett.*, **23**:709–711, 1998.

[73] J. Wilson and J.F.B. Hawkes. *Optoelectronics: An introduction.* Prentice Hall International (UK) Ltd., 2nd edition, 1989.

[74] M.M. Wefers and K.A. Nelson. Generation of high-fidelity programmable ultrafast optical waveforms. *Opt. Lett.*, **20**:1047–1049, 1995.

[75] A.M. Weiner. Ultrafast optical pulse shaping: A tutorial review. *Opt. Commun.*, **284**:3669–3692, 2011.

[76] M Dantus, VV Lozovoy, and I Pastirk. Miips characterizes and corrects femtosecond pulses. *Laser Focus World*, 43:101–104, 2007.

[77] VV Lozovoy, I Pastirk, and M Dantus. Multiphoton intrapulse interference. iv. ultrashort laser pulse spectral phase characterization and compensation. *Optics letters*, 29(7):775–777, 2004.

[78] B. Xu, J.M. Gunn, J.M. Dela Cruz, V.V. Lozovoy, and M. Dantus. Quantitative investigation of the multiphoton intrapulse interference phase scan method for simultaneous phase measurement and compensation of femtosecond laser pulses. *J. Opt. Soc. Am. B*, **23**:750–759, 2006.

[79] VV Lozovoy, I Pastirk, KA Walowicz, and M Dantus. Multiphoton intrapulse interference. ii. control of two- and three-photon laser induced fluorescence with shaped pulses. *J. Chem. Phys.*, 118(7):3187–3196, 2003.

[80] Vadim V Lozovoy and Marcos Dantus. Systematic control of nonlinear optical processes using optimally shaped femtosecond pulses. *ChemPhysChem*, 6(10):1970–2000, Oct 2005.

[81] VV Lozovoy, Y Andegeko, X Zhu, and M Dantus. Applications of ultrashort shaped pulses in microscopy and for controlling chemical reactions. *Chem. Phys.*, 350:118–124, 2008.

[82] VV Lozovoy, TC Gunaratne, JC Shane, and M Dantus. Control of molecular fragmentation using binary phase-shaped femtosecond laser pulses. *Chem. Phys. Chem.*, 7:2471–2473, 2006.

[83] I Pastirk, M Kangas, and M Dantus. Multidimensional analytical method based on binary phase shaping of femtosecond pulses. *J. Phys. Chem. A*, 109(11):2413–2416, 2005.

[84] M Comstock, VV Lozovoy, I Pastirk, and M Dantus. Multiphoton intrapulse interference 6; binary phase shaping. *Optics Express*, 12(6):1061–1066, 2004.

[85] JM Dela Cruz, VV Lozovoy, and M Dantus. Quantitative mass spectrometric identification of isomers applying coherent control. *J. Phys. Chem. A*, 109:8447–8450, 2005.

[86] JM Dela Cruz, M Kangas, I Pastirk, VV Lozovoy, and M Dantus. Systematic chemical recognition using shaped laser pulses. *J. Mod. Opt.*, 53(16):2533–2541, 2006.

[87] VV Lozovoy, X Zhu, TC Gunaratne, D Ahmasi Hassis, JC Shane, and M Dantus. Control of molecular fragmentation using shaped femtosecond pulses. *J. Phys. Chem. A*, 112(17):3789–3812, 2008.

[88] T Gunaratne, M Kangas, S Singh, A Gross, and M Dantus. Influence of bandwidth and phase shaping on laser induced breakdown spectroscopy with ultrashort laser pulses. *Chem. Phys. Lett.*, 423:197–201, 2006.

[89] GT Nogueira, B Xu, Y Coello, M Dantus, and FC Cruz. Broadband 2.12 ghz ti: sapphire laser compressed to 5.9 femtoseconds using miips. *Optics Express*, 16(14):10033–10038, 2008.

[90] B Xu, Y Coello, GT Nogueira, FC Cruz, and M Dantus. Asynchronous encrypted information transmission with sub-6 fs laser system at 2.12 GHz repetition rate. *Optics Express*, 16(19):15109–15114, 2008.

[91] B Xu, Y Coello, VV Lozovoy, DA Harris, and M Dantus. Pulse shaping of octave spanning femtosecond laser pulses. *Optics Express*, 14(22):10939–10944, 2006.

[92] Y Coello, B Xu, T.L Miller, VV Lozovoy, and M Dantus. Group-velocity dispersion measurements of water, seawater, and ocular components using multiphoton intrapulse interference phase scan. *Applied Optics*, 46(35):8394–8401, Nov 2007.

[93] I Pastirk, X Zhy, RM Martin, and M Dantus. Remote characterization and dispersion compensation of amplified shaped femtosecond pulses using miips. *Optics Express*, 14(19):8885–8889, 2006.

[94] M. Mazilu, A. C. De Luca, A. Riches, and and K. Dholakia C. S. Herrington. Optimal algorithm for fluorescence suppression of modulated Raman spectroscopy. *Opt. Express*, **18**:11382–11395, 2010.

[95] H Li, DA Harris, B Xu, PJ Wrzesinski, VV Lozovoy, and M Dantus. Coherent mode-selective raman excitation towards standoff detection. *Optics Express*, 16(8):5499–5504, 2008.

[96] H Li, D Ahmasi Harris, B Xu, PJ Wrzesinski, VV Lozovoy, and M Dantus. Standoff and arms-length detection of chemicals with single-beam coherent anti-stokes raman scattering. *Appl. Opt.*, 48(4):17–22, 2009.

[97] O Katz, A Natan, Y Silberberg, and S Rosenwaks. Standoff detection of trace amounts of solids by nonlinear raman spectroscopy using shaped femtosecond pulses. *Appl. Phys. Lett.*, 92(171116):1–3, 2008.

[98] P Xi, Y Andegeko, LR Weisel, VV Lozovoy, and M Dantus. Greater signal, increased depth, and less photobleaching in two-photon microscopy with 10fs pulses. *Optics Communications*, 281(7):1841–1849, 2008.

[99] M Muller, J Squier, R Wolleschensky, U Simon, and GJ Brakenhoff. Dispersion pre-compensation of 15 femtosecond optical pulses for high-numerical-aperture objectives. *Journal of Microscopy*, 191(2):141, 1998.

[100] R. Wolleschensky, T. Feurer, R. Sauerbrey, and U. Simon. Characterization and optimization of a laser-scanning microscope in the femtosecond regime. *Appl. Phys. B*, **67**:87–94, 1998.

[101] JM Dela Cruz, I Pastirk, M Comstock, VV Lozovoy, and M Dantus. Use of coherent control methods through scattering biological tissue to achieve functional imaging. *Proceedings of the National Academy of Sciences*, 101(49):16996–17001, 2004.

[102] S. Akturk, X. Gu, P. Gabolde, and R. Trebino. The general theory of first-order spatio-temporal distortions of Gaussian pulses and beams. *Opt. Express*, **13**:8642–8661, 2005.

[103] A. Ashkin. Acceleration and trapping of particles by radiation pressure. *Phys. Rev. Lett.*, 24(4):156–159, Jan 1970.

[104] A. Ashkin. Applications of laser radiation pressure. *Science*, 210(4474):1081–1088, 1980.

[105] A Ashkin. Optical trapping and manipulation of neutral particles using lasers. *Proc. Natl. Acad. Sci. USA*, 64:4853–4860, 1997.

[106] MP MacDonald, , GC Spalding, and K Dholakia. Microfluidic sorting in an optical lattice. *Nature*, 426:421–424, 2003.

[107] PRT Jess, V Garcés-Chávez, AC Riches, CD Herrington, and K Dholakia. Simultaneous raman micro-spectroscopy of optically trapped and stacked cells. *J. Raman Spectrosc.*, 38(9):1082–1088, 2007.

[108] RM Berry and HC Berg. Absence of a barrier to backwards rotation of the bacterial flagellar motor demonstrated with optical tweezers. *Proc. Natl. Acad. Sci. USA*, 94:14433–14437, 1997.

[109] MM Burns, J-M Fournier, and JA Golovchenko. Optical binding. *Phys. Rev. Lett.*, **63**:1233–1236, 1989.

[110] MM Burns, J-M Fournier, and JA Golovchenko. Optical matter: Crystallization and binding in intense fields. *Science*, **249**:749–754, 1990.

[111] S Mohanty, J Andrews, and P Gupta. Optical binding between dielectric particles. *Optics Express*, 12(12):2746–2753, 2004.

[112] Maria Dienerowitz, Michael Mazilu, and Kishan Dholakia. Optical manipulation of nanoparticles: a review. *J. Nanophoton.*, 2(1):021875, Jan 2008.

[113] M Born and E Wolf. *Principles of Optics*. Cambridge University Press, 7th edition, 1999.

[114] E Aspnes, T Milster, and K Visscher. Optical force model based on sequential ray tracing. *Applied Optics*, Jan 2009.

[115] T.M Grzegorczyk, B.A Kemp, and J.A Kong. Trapping and binding of an arbitrary number of cylindrical particles in an in-plane electromagnetic field. *J. Opt. Soc. Am. A*, 23(9):2324–2330, Jul 2006.

[116] N. K Metzger, K Dholakia, and E. M Wright. Observation of bistability and hysteresis in optical binding of two dielectric spheres. *Phys. Rev. Lett.*, 96(6):1–4, Feb 2006.

[117] N K Metzger, E M Wright, and K Dholakia. Theory and simulation of the bistable behaviour of optically bound particles in the mie size regime. *New J. Phys.*, 8(8):139–139, Aug 2006.

[118] NK Metzger, EM Wright, W Sibbett, and K Dholakia. Visualization of optical binding of microparticles using a femtosecond fiber optical trap. *Optics Express*, 14(8):3677–3687, 2006.

[119] DLAJ Rodríguez. Collapse of optical binding under secondary irradiation. *Opt. Lett*, 33:1830–1832, 2008.

[120] JC Crocker and DG Grier. Methods of digital video microscopy for colloidal studies. *Journal of colloid and interface science*, 179(1):298–310, 1996.

[121] J Baumgartl, AP Rudhall, M Mazilu, E Wright, and K Dholakia. Revisiting transverse optical binding. *Proc. SPIE*, **7400**:74001, 2009.

[122] BA Kemp, TM Grzegorczyk, and JA Kong. Lorentz force on dielectric and magnetic particles. *Journal of Electromagnetic Waves and Applications*, 20(6):827–839, 2006.

[123] DL Andrews and J Rodríguez. Collapse of optical binding under secondary irradiation. *Opt. Lett.*, **33**:1830–1832, 2008.

[124] D.M. Gherardi, A.E. Carruthers, T Cizmar, E.M. Wright, and K Dholakia. A dual beam photonic crystal fiber trap for microscopic particles. *Appl. Phys. Lett.*, 93:041110, 2008.

[125] J Rodríguez and DL Andrews. Influence of the state of light on the optically induced interparticle interaction. *Phys. Rev. A*, **79**:022106, 2009.

[126] J Rodríguez and DL Andrews. Inter-particle interaction induced by broadband radiation. *Opt. Comm.*, **282**:2267–2269, 2009.

[127] DS Bradshaw and DL Andrews. Optically induced forces and torques: Interactions between nanoparticles in a laser beam. *Phys. Rev. A*, **72**:033816, 2005.

[128] PC Chaumet and M Nieto-Vesperinas. Time-averaged total force on a dipolar sphere in an electromagnetic field. *Opt. Lett.*, **25**:1065–1067, 2000.

[129] BT Draine. The discrete-dipole approximation and its application to interstellar graphite grains. *Astrophys. J.*, **333**:848–872, 1988.

[130] J.D. Jackson. *Classical Electrodynamics*. Wiley, 3rd edition, 1998.

[131] V Karásek, O. Brzobohaty, and P Zemanek. Longitudinal optical binding of several spherical particles studied by the coupled dipole method. *J. Opt. A*, 11(3):034009, 2009.

[132] J.C. Shane, M. Mazilu, W.M. Lee, and K. Dholakia. Effect of pulse temporal shape on optical trapping and impulse transfer using ultrashort pulsed lasers. *Opt. Express*, **18**:7554–7568, 2010.

[133] J Gordon. Radiation Forces and Momenta in Dielectric Media. *Phys Rev A*, 8(1):14–21, 1973.

[134] M. Mazilu, A. Rudhall, E. Wright, and K. Dholakia. An interacting dipole model to explore broadband transverse optical binding. *J. Phys. Condens. Matter "to appear"*, 2012.

[135] W.R. Zipfel, R.M. Williams, and W.W. Webb. Nonlinear magic: multiphoton microscopy in the biosciences. *Nat. Biotechnol.*, **21**:1369–1377, 2003.

[136] R. Carriles, D.N. Schafer, K.E. Sheetz, J.J. Field, R. Cisek, V. Barzda, A.W. Sylvester, and J.A. Squier. Imaging techniques for harmonic and multiphoton absorption fluorescence microscopy. *Rev. Sci. Instrum.*, **80**:081101(1–23), 2009.

[137] A. Vogel, J. Noack, G. Hüttman, and G. Paltauf. Mechanisms of femtosecond laser nanosurgery of cells and tissues. *Appl. Phys. B*, **81**:1015–1047, 2005.

[138] P.A. Quinto-Su and V. Venugopalan. Mechanisms of laser cellular microsurgery. *Methods Cell Biol.*, **82**:113–151, 2007.

[139] A. Heisterkamp, I.Z. Maxwell, E. Mazur, J.M. Underwood, J.A. Nickerson, S. Kumar, and D.E. Ingber. Pulse energy dependence of subcellular dissection by femtosecond by femtosecond laser pulses. *Opt. Express*, **13**:3690–3696, 2005.

[140] K. Kuetemeyer, J. Baumgart, H. Lubatschowski, and A. Heisterkamp. Repetition rate dependency of low-density plasma effects during femtosecond-laser-based surgery of biological tissue. *Appl. Phys. B*, **97**:695–699, 2009.

[141] J. Baumgart. Repetition rate dependency of reactive oxygen species formation during femtosecond laser-based cell surgery. *J. Biomed. Opt.*, **14**:054040(1–9), 2009.

[142] A. Uchugonova, M. Lessel, S. Nietzsche, C. Zeitz, K. Jacobs, C. Lemke, and K. König. Nanosurgery of cells and chromosomes using near-infrared twelve-femtosecond laser pulses. *J. Biomed. Opt.*, **17**:101502(1–6), 2012.

[143] D. Stevenson. Femtosecond optical transfection of cells: viability and efficiency. *Opt. Express*, **14**:7125–7133, 2006.

[144] J. Baumgart, W. Bintig, A. Ngezahayo, S. Willenbrock, H. M. Escobar, W. Ertmer, H. Lubatschowski, and A. Heisterkamp. Quantified femtosecond laser based opto-perforation of living GFSHR-17 and MTH53a cells. *Opt. Express*, **16**:3021–3031, 2008.

[145] X. Tsampoula, V. Garcés-Chávez, M. Comrie, D.J. Stevenson, B. Agate, C.T.A. Brown, F. Gunn-Moore, and K. Dholakia. Femtosecond cellular transfection using a nondiffracting light beam. *Appl. Phys. Lett.*, **91**:053902(1–3), 2007.

[146] M. Antkowiak, M.L. Torres-Mapa, F. Gunn-Moore, and K. Dholakia. Application of dynamic diffractive optics for enhanced femtosecond laser based cell transfection. *J. Biophotonics*, **3**:696–705, 2010.

[147] J. Tas and G. Westerneng. Fundamental aspects of the interaction of Propidium Diiodide with nucleic acids studied in a model system of polyacrylamide films. *J. Histochem Cytochem*, **29**:929–936, 1981.

[148] H. Misawa, M. Koshioka, K. Sasaki, and N. Kitamura. Three-dimensional optical trapping and laser ablation of a single polymer latex particle in water. *J. Appl. Phys.*, **70**:3829–3836, 1991.

[149] D. Pestov, Y. Andegeko, V.V. Lozovoy, and M. Dantus. Photobleaching and photoenhancement of endogenous fluorescence observed in two-photon microscopy with broadband laser sources. *J. Opt.*, **12**:084006, 2010.

[150] A.C. Tien, S. Backus, H. Kapteyn, M. Murnane, and G. Mourou. Short-pulse laser damage in transparent materials as a function of pulse duration. *Phys. Rev. Lett.*, **82**:3883–3886, 1999.

[151] M. Lenzner, J. Krüger, S. Sartania, Z. Cheng, Ch. Spielmann, G. Mourou, W. Kautek, and F. Krausz. Femtosecond optical breakdown in dielectrics. *Phys. Rev. Lett.*, **80**:4076–4079, 1998.

[152] B.C. Stuart, M.D. Feit, A.M. Rubenchik, B.W. Shore, and M.D. Perry. Laser-induced damage in dielectrics with nanosecond to subpicosecond pulses. *Phys. Rev. Lett.*, **74**:2248–2252, 1995.

[153] S. Akturk, X. Gu, P. Bowlan, and R. Trebino. Spatio-temporal couplings in ultrashort laser pulses. *J. Opt.*, **12**(093001):1–20, 2010.

[154] R. Grunwald, U. Griebner, F. Tschirschwitz, E. T. J. Nibbering, T. Elsaesser, V. Kebbel, H.-J. Hartmann, and W. Jüptner. Generation of femtosecond bessel beams with microaxicon arrays. *Opt. Lett.*, 25(13):981–983, Jul 2000.

[155] JE Morris, AE Carruthers, M Mazilu, PJ Reece, T Cizmar, P Fischer, and K Dholakia. Optical micromanipulation using supercontinuum laguerre-gaussian and gaussian beams. *Optics Express*, 16(14):10117–10129, 2008.

[156] J. Durnin, J.J. Miceli, and J. Eberly. Diffraction-free beams. *Phys. Rev. Lett.*, **58**:1499–1501, 1987.

[157] J. Durnin. Exact solutions for nondiffracting beams. I The scalar theory. *J. Opt. Soc. Am. A*, **4**:641–651, 1987.

[158] M. Piché, G. Rousseau, C. Varin, and N. McCarthy. Concical wave packets: their propagation speed and their longitudinal fields. *SPIE Laser Resonators II*, **3611**:332–343, 1999.

[159] T. Cižmár and K. Dholakia. Tunable Bessel light modes: engineering the axial propagation. *Opt. Express*, **17**:15558–15570, 2009.

[160] M. Bock, S.K. Dad, and R. Grunwald. Programmable ultrashort-pulsed flying images. *Opt. Express*, **17**:7465–7478, 2009.

[161] Heiki S onajalg, Margus Rätsep, and Peeter Saari. Demonstration of the bessel-x pulse propagating with strong lateral and longitudinal localization in a dispersive medium. *Opt. Lett.*, 22(5):310–312, Mar 1997.

[162] P. Saari and K. Reivelt. Evidence of X-shaped propagation-invariant localized light waves. *Phys. Rev. Lett.*, **79**:4135–4138, 1997.

[163] A. Chong, W.H. Renninger, D.N. Christodoulides, and F.W. Wise. Airy-Bessel wave packets as versatile linear light bullets. *Nat. Photon.*, **4**:103–106, 2010.

[164] Z. Bor. Distortion of femtosecond laser pulses in lenses and lens systems. *J. Mod. Opt.*, **35**:1907–1918, 1988.

[165] D Li, S Zeng, Q Luo, P Bowlan, V Chauahan, and R Trebino. Propagation dependence of chirp in gaussian pulses and beams due to angular dispersion. *Optics letters*, 34(7):962–964, 2009.

[166] J. Baumgartl and C. Bechinger. On the limits of digital video microscopy. *Europhys. Lett.*, **71**:487–493, 2005.

[167] R.F. Marchington, Y. Arita, X. Tsampoula, F.J. Gunn-Moore, and K. Dholakia. Optical injection of mammalian cells using a microfluidic platform. *Biomed. Opt. Express*, **1**:527–536, 2010.

[168] D.J. Bradley and G.H.C. New. Ultrashort pulse measurements. *Proc. IEEE*, **62**:313–345, 1974.

[169] W. Rudolph, M. Sheik-Bahae, A. Bernstein, and L.F. Lester. Femtosecond autocorrelation measurements based on two-photon photoconductivity in ZnSe. *Opt. Lett.*, **22**:313–315, 1997.

[170] J.-C.M. Diels, J.J Fontaine, I.C. McMichael, and F. Simoni. Control and measurement of ultrashort pulse shapes (in amplitude and phase) with femtosecond accuracy. *Appl. Opt.*, **24**:1270–1282, 1985.

[171] D.J. Kane and R. Trebino. Characterization of arbitrary femtosecond pulses using frequency-resolved optical gating. *IEEE J. Quantum Electron.*, **29**:571–579, 1993.

[172] R. Trebino and D.J. Kane. Using phase retrieval to measure the intensity and phase of ultrashort pulses: frequency-resolved optical gating. *J. Opt. Soc. Am. A*, **10**:1101–1111, 1993.

[173] A. Baltuška, M.S. Pschenichnikov, and D.A. Wiersma. Amplitude and phase characterization of 4.5-fs pulses by frequency-resolved optical gating. *Opt. Lett.*, **23**:1474–1476, 1998.

[174] K.W. DeLong, R. Trebino, J. Hunter, and W.E. White. Frequency-resolved optical gating with the use of second-harmonic generation. *J. Opt. Soc. Am. B*, **11**:2206–2215, 1994.

[175] C. Iaconis and I.A. Walmsley. Spectral phase interferometry for direct electric-field reconstruction of ultrashort pulses. *Opt. Lett.*, **23**:792–794, 1998.

[176] K.C. Chu, J.P Heritage, R.S. Grant, K.X. Liu, A. Dienes, W.E. White, and A. Sullivan. Direct measurement of the spectral phase of femtosecond pulses. *Opt. Lett.*, **20**:904–906, 1995.

[177] JD Jackson. *Classical Electrodynamics*. John Wiley and Sons, Inc, 3rd edition, 1999.

[178] R Gussard, T Lindmo, and I Brevik. Calculation of the trapping force in a strongly focused laser beam. *J. Opt. Soc. Am. B*, 9(10):1922–1930, 1992.

[179] B.B. Praveen, D.J. Stevenson, M. Antkowiak, K. Dholakia, and F.J. Gunn-Moore. Enhancement and optimization of plasmid expression in femtosecond optical transfection. *J. Biophotonics*, **4**:229–235, 2011.

Chapter 7

Appendix

7.1 Calculation of pulse shape profiles

In chapter 1 expressions for different pulse profiles are presented. This section of the appendix explains how the values obtained in Table 1.2 are calculated as well as the profiles in Fig. 1.1.

7.1.1 Gaussian pulses

The following method was used to calculate the power of the pulse profile for Gaussian-shaped pulses. The Gaussian profile is written as

$$P = P_0 \exp\left(k_p \frac{t^2}{\tau_p^2}\right), \tag{7.1}$$

where P_0 is the peak power, k_p is a constant depending upon the pulse profile and τ_p is the FWHM pulse duration. To find the constant k_p we find the half-maximum power by setting the ratio of power to peak power to one half.

$$\frac{P}{P_0} = \frac{1}{2} = \exp\left(k_p \frac{t^2}{\tau_p^2}\right). \tag{7.2}$$

The FWHM pulse duration occurs at

$$t = \frac{\tau_p}{2}. \tag{7.3}$$

Rearranging equation 7.2 using equation 7.2 results in

$$k_p = 4 \ln 2. \tag{7.4}$$

To find the peak power P_0 we integrate a single pulse (in terms of power) with respect to time from minus to plus infinity, which gives the pulse energy, E_p.

$$E_p = \int_{-\infty}^{\infty} P dt, \tag{7.5}$$

$$E_p = P_0 \int_{-\infty}^{\infty} \exp\left(k_p \frac{t^2}{\tau_p^2}\right) dt = P_0 \sqrt{\frac{\pi \tau_p^2}{k_p}}. \tag{7.6}$$

Rearranging equation 7.6 gives

$$P_0 = \frac{E_p}{\tau_p} \sqrt{\frac{k_p}{\pi}} = \frac{E_p}{\tau_p} \sqrt{\frac{4 \ln 2}{\pi}} = k_s \frac{E_p}{\tau_p}, \tag{7.7}$$

where k_s is the constant which relates the pulse shape with the peak power, as demonstrated in Table 1.2. Therefore the Gaussian power pulse profile for any given FWHM pulse duration τ_p is given by

$$P_{Gaussian}(t) = \frac{E_p}{\tau_p} \sqrt{\frac{4 \ln(2)}{\pi}} \exp\left(-\frac{4 \ln(2) t^2}{\tau_p^2}\right). \tag{7.8}$$

7.1.2 Sech-squared pulses

The same method is used to calculate the Sech-squared pulse profile. In short, k_p is found to be

$$k_p = 2 \cosh^{-1}(\sqrt{2}). \tag{7.9}$$

The integration of the power pulse profile gives the pulse energy,

$$E_p = P_0 \int_{-\infty}^{\infty} \operatorname{sech}^2\left(k_p \frac{t}{\tau_p}\right) dt = \frac{P_0 \tau_p}{k_p} \left[\tanh\left(k_p \frac{t}{\tau_p}\right)\right]_{-\infty}^{\infty} = \frac{2 P_0 \tau_p}{k_p}, \tag{7.10}$$

which gives the Sech-squared power pulse profile for any given FWHM pulse duration as

$$P_{Sech-squared}(t) = \frac{E_p}{\tau_p} \cosh^{-1}(\sqrt{2}) \operatorname{sech}^2\left(\frac{2 \cosh^{-1}(\sqrt{2}) t}{\tau_p}\right). \tag{7.11}$$

7.2 Well-known pulse measurement techniques

In this section other measurement techniques are discussed as they are considered relevant to the subject matter, However as these techniques were not performed experimentally (with the exception of interferometric autocorrelation), this discussion has been reserved for the Appendix.

7.2.1 Autocorrelation (AC) and interferometric autocorrelation (IAC)

The intensity autocorrelation (AC) is a relatively simple way to measure the pulse duration. This technique involves splitting the pulse into two identical pulses and then delaying one pulse with respect to the other and measuring the resulting intensity as function of pulse overlap [4]. This is generally performed using a nonlinear medium, such as a nonlinear crystal optimised for SHG [4]. Fig 7.1 illustrates a typical arrangement for an autocorrelator aligned for interferometric detection. Intensity autocorrelation (AC) and interferometric autocorrelation can both be performed in the interferometric setup by adjusting the scanning rate (fast for AC, low for IAC). The scan rate allows pulses of femtoseconds duration to slowly sweep over the reference pulse by spatially displacing the pulse (which is equivalent to a time-displaced pulse). The reason for choosing a nonlinear method over a linear method can be attributed to the better signal to background ratio obtained. By using $E_1(t-\delta)\exp(i\phi_1)$ for the time-dependent electric field in δ time-sweeping arm 1 and $E_2(t)\exp(i\phi_2)$ for arm 2 where E is the amplitude and ϕ is the phase, we can obtain the intensity obtained at the detector by considering equation 1.2 [4]. For linear detection as in Fig. the intensity is given by

$$\begin{aligned} I_{\text{linear}}(t,\delta) &= \frac{1}{2}nc\epsilon_0\int_{-\infty}^{\infty}(E_1(t-\delta)E_1^*(t-\delta)+E_1(t-\delta)E_2^*(t)\exp(i\Phi) \\ &+ E_1^*(t-\delta)E_2(t)\exp(-i\Phi)+E_2(t)E_2^*(t))\,dt, \end{aligned} \tag{7.12}$$

where $\Phi = \phi_1 - \phi_2$. Depending on whether AC or IAC is used the peak-to-background ratio varies. For IAC the peak signal occurs at $\delta = 0$ and results in

$$I_{\text{linear}}(max) \propto 4\int_{-\infty}^{\infty}E^2dt, \tag{7.13}$$

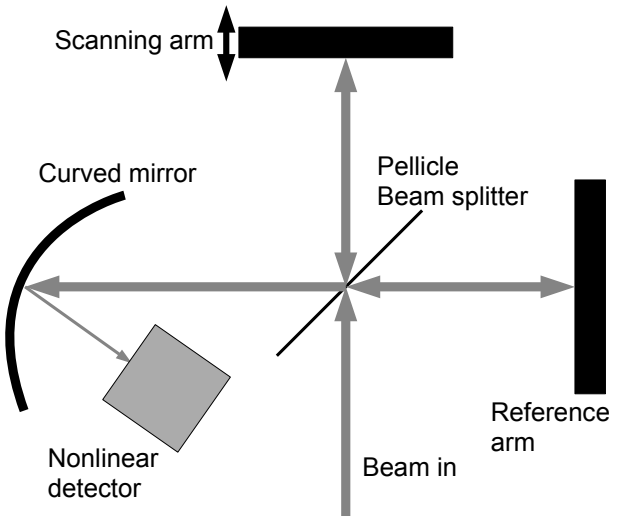

Figure 7.1: An interferometric autocorrelator with a ultra-thin beam splitter and curved mirror for dispersion-free operation. The nonlinear detector can either be a second harmonic crystal with filtering or based on two-photon conductivity in a semiconductor. A scanning arm is employed to allow the two pulse replicas to sweep over one another sufficiently slowly for detection electronics.

for constant amplitudes $E_1 = E_2 = E$. The minimum signal observed occurs at large δ and and has no cross-terms between E_1 and E_2, so resulting in

$$I_{\text{linear}}(min) \propto 2 \int_{-\infty}^{\infty} E^2 dt. \tag{7.14}$$

Therefore the peak-to-background ratio for linear IAC is 2:1. In practice noise and misalignments reduce this ratio further and therefore nonlinear autocorrelation is preferred. For AC this ratio falls to 1:1 since intensity autocorrelation is insensitive to phase and can only consider the constant-amplitude terms. Therefore it is impractical to distinguish peaks from noise in standard AC, but is theoretically possible in IAC, however it is not a standard ultrashort pulse characterisation technique [168].

In nonlinear (2-photon) autocorrelation the intensity is given by

$$I_{\text{nonlinear}} = I_{\text{linear}}(t, \delta) + k_{\text{2-photon}} \int_{-\infty}^{\infty} \left[\left(E(t-\delta) + E(t) \right)^2 \right]^2, \tag{7.15}$$

where $k_{\text{nonlinear}}$ is a factor defining the efficiency of the 2-photon process. Since the linear signal dominates, this must be removed in order obtain the peak 2-photon signal from the background. This is usually achieved by use of a filter or by arranging the setup for background-free SHG (AC only) [5]. The need for a filter can be obviated by utilising 2-photon conductivity in a semiconductor such that the 2-photon process is integrated into the detection unit [169]. By the same reasoning as previously, the peak-to-background ratio in 2-photon AC is 3:1, and in 2-photon IAC the ratio 8:1. Therefore using 2-photon processes for the autocorrelation improves the peak-to-background ratio. Further improvements to this ratio can be achieved by utilising 3-photon processes to achieve a 3-photon AC ratio of 10:1 and 3-photon IAC ratio of 32:1 [36].

The expression usually used to describe the autocorrelation of an ultrashort pulse with GVD [4]. Starting with the electric field for a chirped pulse

$$E(t) = \exp\left(-\frac{(1+ia)t^2}{\tau_G^2}\right), \tag{7.16}$$

where a is the chirp parameter and τ_G is related to the Gaussian FWHM pulse duration, τ_p by $\tau_G = 1.177\tau_p$. Equation 7.16 is inserted into equation 7.15 to obtain

$$\begin{aligned} I_{\text{2nd-AC}}(\delta) &= 1 + 2\exp\left[\left(\frac{\delta}{\tau_G}\right)^2\right] + 4\exp\left[\left(\frac{a^2+3}{4}\right)\left(\frac{\delta}{\tau_G}\right)^2\right]\cos\left(\frac{a}{2}\left(\frac{\delta}{\tau_G}\right)^2\right)\cos(\omega_c\delta) \\ &+ 2\exp\left[-(1+a^2)\left(\frac{\delta}{\tau_G}\right)^2\right]\cos(2\omega_c\delta), \end{aligned} \tag{7.17}$$

where ω_c is the centre frequency.

Figs. 7.2 and 7.3 show the theoretical IAC traces of a 100 nm bandwidth pulse centred at 800 nm when unchirped and chirped, respectively. Note the 1:8 ratio in intensity of the background to maximum fringe intensity. The chirped IAC trace shows a narrower set of fringes which are overlapped with the AC intensity corresponding to the chirped pulse duration.

We obtained an example set of interferometric autocorrelation results for reference. However we did not utilise the technique during experiments. The results of the experiment using a Femtochrome FR-103PD autocorrelator with additional phase added (explained below in the MIIPS section) are illustrated in Fig. 7.4. The interferometric autocorrelations contained higher-order spectral phase contributions due to dispersion that could not be corrected in this arrangement. The autocorrelation traces extended beyond the shown times but is not fully shown for clarity. A MATLAB program is provided in the

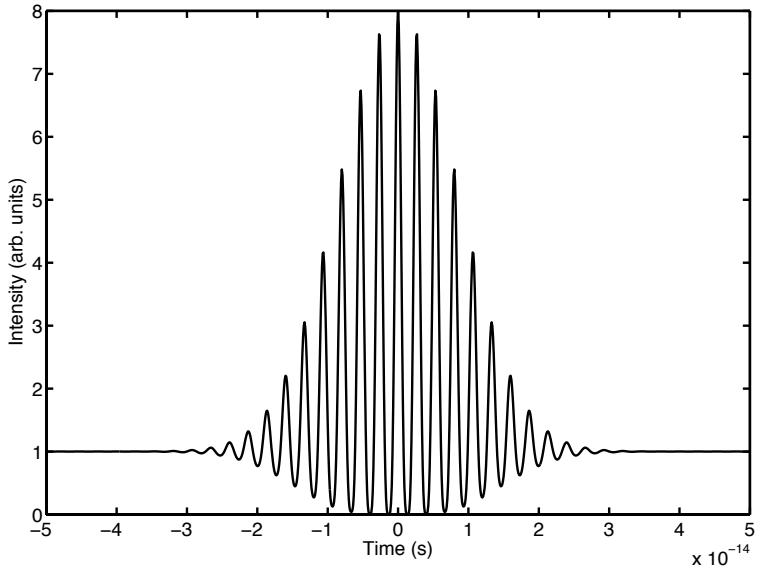

Figure 7.2: The IAC trace of an unchirped pulse of 100 nm bandwidth centred at 800 nm.

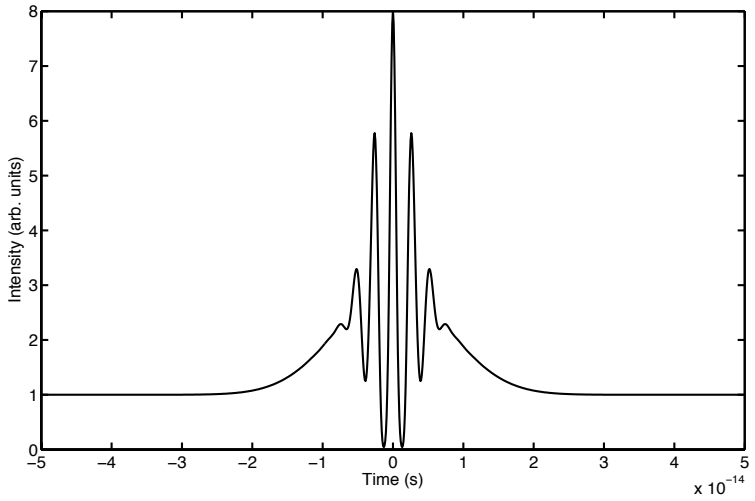

Figure 7.3: The IAC trace of a chirped pulse for the same parameters as the unchirped example in Fig. 7.2. The chirp parameter used was 5.

supplementary CD to demonstrate the calibration procedure (appropriate for the aforementioned autocorrelator family) and simple re-scaling of the data. The autocorrelation

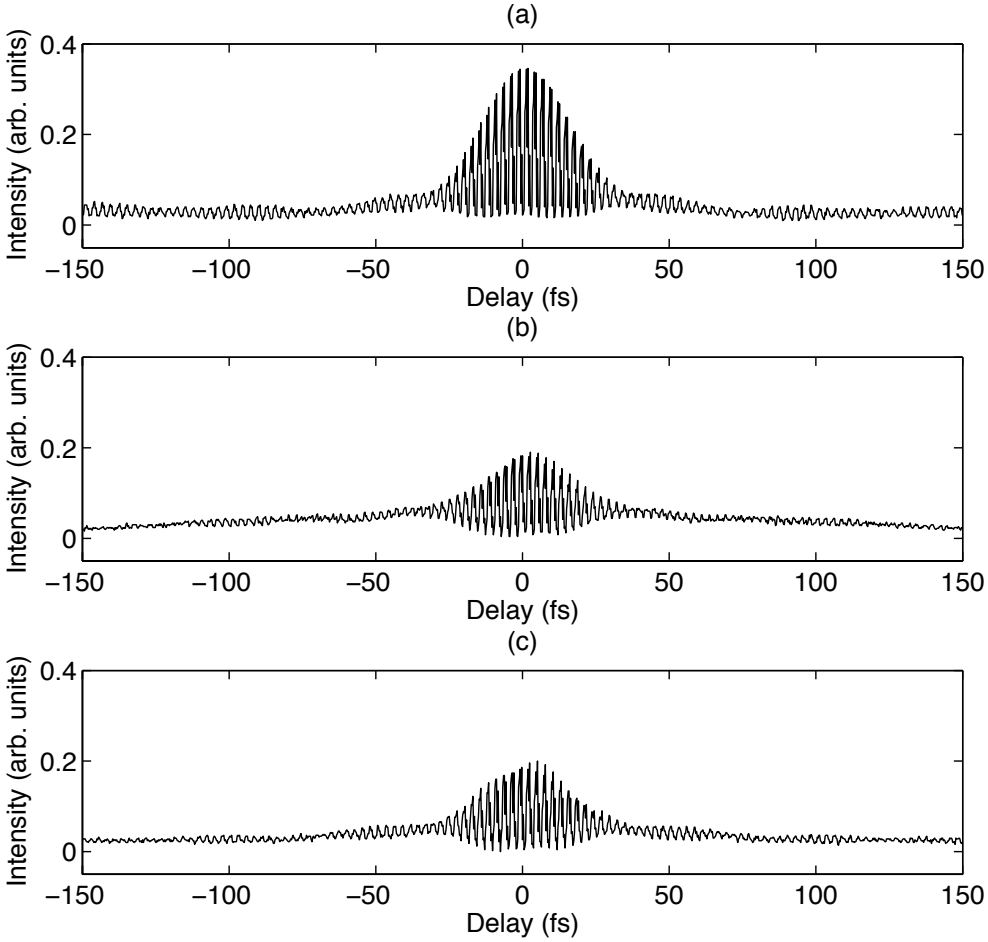

Figure 7.4: Example interferometric autocorrelation traces obtained for (a) zero-phase added, (b) 500 fs^2 phase added and (c) 1000 fs^2 phase added. Note the optical system dispersion dominates and results in complex autocorrelation traces.

offers a relatively simple way to estimate the pulse duration however this method has some disadvantages. Most importantly, the the pulse shape needs to be known or retrieved. In general it is difficult to know exactly what the pulse shape looks like and direct pulse shape retrieval is impossible because the same autocorrelation can be produced by many different pulse shapes. The problem is even worse in the sub-10 fs regime where pulses become increasingly complex and autocorrelator design must be totally dispersion-free [46]. Therefore additional knowledge is required in order to describe the pulse. A partial so-

lution involves measuring the spectrum and using an iterative computer program [170], however this does not remove ambiguities [46]. Further methods have been developed to improve upon the results obtained by autocorrelation methods and are discussed below.

7.2.2 Frequency resolved optical gating (FROG)

Following autocorrelation techniques, a major step forward in ultrashort pulse characterisation was achieved in what is known as frequency resolved optical gating (FROG) [171]. FROG offered a more complete picture of ultrashort pulse intensity and phase by splitting the pulse into two identical parts and varying the overlap of the pulse replicas in a nonlinear medium such as glass and then imaging the resultant pulse in terms of its spectral components [172]. In Fig. 7.5 (a) the setup used in [171] is summarised. In this arrangement the Kerr-induced diffracted light is spectrally resolved and imaged onto a camera and a two dimensional image is created of delay time vs frequency. The resultant image width shows the pulse duration in one direction, while any chirp will be seen as a frequency-dependent evolution in time whose angle shows whether the pulse is positively or negatively chirped. Part (b) of Fig. 7.5 illustrates this effect of chirp. The equation which describes the FROG trace is given by [172]

$$S_{\mathrm{FROG}}(\omega,\delta) = \left| \int_{-\infty}^{\infty} E(t) g(t-\delta) \exp(-i\omega t) dt \right|^2 , \tag{7.18}$$

where the $g(t-\delta) = |E(t-\delta)|^2$ is the delay gate defining the strength of the nonlinear process as function of delay time δ. Equation 7.18 defines the example traces in Fig. 7.5 and allows full characterisation of the pulse since the problem has been converted from one to two dimensions, allowing simultaneous display of frequency and gate delay time [172]. FROG has been successfully used for the characterisation of ultrashort pulses down to 4.5 fs, however the design of the setup requires particular care to avoid dispersive effects [173].

The use of the third-order Kerr process for FROG eliminates the direction of time ambiguity that exists in second-order autocorrelation that means that it is impossible to distinguish the difference between a pulse that is reversed in time. A version of FROG involving SHG retains this ambiguity in time but allows the use of lower peak power pulses due to the higher effective nonlinearity afforded by second-order processes [174].

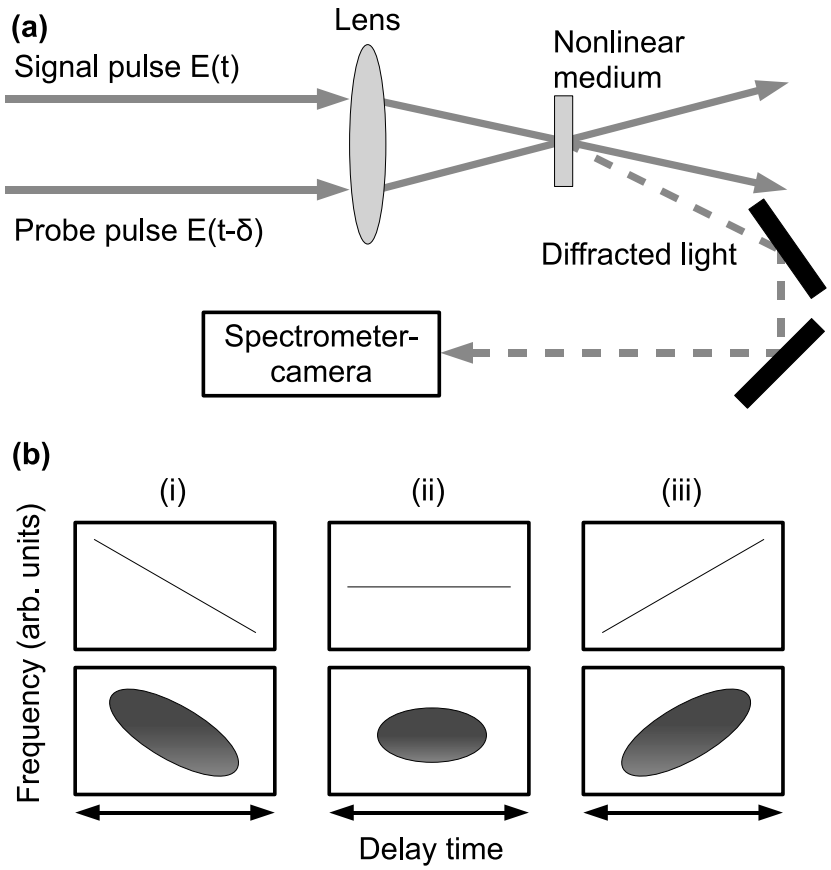

Figure 7.5: In part (a) the an example arrangement for third-order FROG is shown. In part (b) the FROG trace is shown for a (i) negatively chirped pulse, (ii) unchirped pulse and (iii) positively chirped pulse. Note in (ii) the pulse has no frequency dependence meaning pulse is approximately transform-limited whereas in (i) and (iii) the gradient of the image defines whether the pulse is positively or negatively chirped.

7.2.3 Spectral interferometry for direct electric field reconstruction (SPIDER)

Before the invention of spectral interferometry for direct electric field reconstruction (SPIDER), techniques for characterising the temporal profile of ultrashort pulses involved performing measurements in the time domain, that is, the ultrashort pulse characterisation involving some element of time delay between two pulse replicas. Whereas FROG

offered a spectral measurement in combination with a temporal measurement, SPIDER offered a frequency-domain only technique for characterising ultrashort pulses [175]. It is unimportant whether one characterises in the time or spectral domains as a measurement in one domain can simply be transferred to the other domain via the appropriate Fourier transform, which requires a small amount of computational power. Although conceptually a time-domain measurement is the preferred method, a frequency-domain measurement is a perfectly adequate method for ultrashort pulse characterisation if the method can reliably obtain the full spectral phase. The SPIDER method [175] is an interferometric technique that built upon a pre-existing technique involving spectral interference [176]. In SPIDER an interferometric arrangement is employed in which two pulse replicas are created with a constant time delay, both of which are mixed with a strongly chirped pulse within a nonlinear crystal. The resulting frequency-converted spectrum is then collected in a spectrometer. Fig. 7.6 summarises the SPIDER process. The spectral inteference

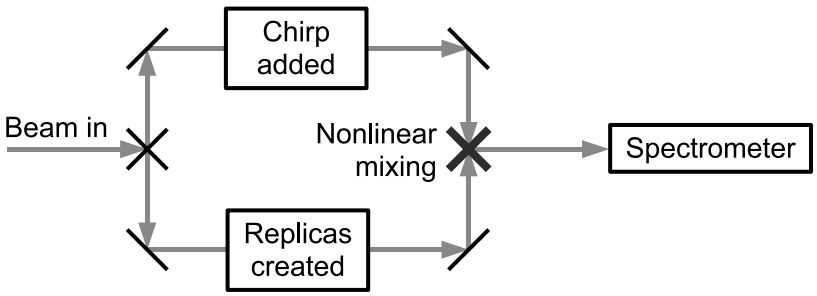

Figure 7.6: SPIDER is an interferometric technique that utilises nonlinear mixing between two pulse replicas with constant delay and a further chirped pulse. The two pulse replicas effectively create a spectral amplitude modulation of constant reference frequency (through the Fourier transform of a double-pulse), which when frequency mixed with the chirped pulse results in an up-converted sample whose intensity depends upon the relative phase between the replica pulse spectrum and chirped pulse spectrum.

pattern has an intensity given by [175]

$$S_{\mathrm{SPIDER}} = |E(\omega_c)|^2 + |E(\omega_c - \Omega)|^2 + 2|E(\omega_c)E(\omega_c + \Omega)|\cos[\phi(\omega_c + \Omega) - \phi(\omega_c) + \omega_c \tau], \quad (7.19)$$

where $E(\omega)$ is the rapidly-varying spectral electric field, ω_c is the centre frequency of the portion of spectrum under investigation, Ω defines the amount of spectral phase introduced by the chirping element. The spectral phase is obtained by calculating or measuring the fixed delay time, fundamental spectral intensity and dispersion introduced by the setup

and subsequently removing these terms from equation 7.19 through appropriate filtering after Fourier transforming the up-converted spectrum.

7.3 Finite element modeling using COMSOL

In this Appendix the derivations of the expressions used to describe the Maxwell Stress tensor and surface force are described.

7.3.1 Derivation of Maxwell stress tensor force for use in COMSOL

To compute the force acting on two dielectric particles in close location, the equations of motion for the system in an electromagnetic field are derived [122]. Starting with the time-averaged Lorentz force density expression we derive the generalised force on a dielectric particle by following the approach in [177]

$$\bar{f} = \frac{1}{2}\left(\rho\bar{E}^* + \bar{J} \times \bar{B}^*\right) \tag{7.20}$$

with the * representing the complex conjugate. Maxwell's equations for monochromatic waves are given by:

$$\rho = \nabla.\,\bar{D} \tag{7.21}$$

$$\bar{J} = \nabla \times \bar{H} + i\omega\bar{D} \tag{7.22}$$

$$\nabla.\,\bar{B} = 0 \tag{7.23}$$

$$i\omega\bar{B} = \nabla \times \bar{E} \tag{7.24}$$

Using equation 7.20 and the Maxwell equations and inserting equation 7.23 for completeness the force density is given by:

$$\bar{f} = \frac{1}{2}\Re\left((\nabla.\,\bar{D})\bar{E}^* + (\nabla \times \bar{E}^*) \times \bar{D} + (\nabla.\,\bar{B}^*)\bar{H} + (\nabla \times \bar{H}) \times \bar{B}^*\right) \tag{7.25}$$

Equation 7.25 can be reduced to:

$$\bar{f} = -\frac{1}{2}\Re\left(\nabla.\,\bar{\bar{T}}(\bar{r})\right) \tag{7.26}$$

where

$$\bar{\bar{T}}(\bar{r}) = \frac{1}{2}\left(\bar{D}.\,\bar{E}^* + \bar{B}^*.\,\bar{H}\right)\bar{\bar{I}} - \bar{D} \otimes \bar{E}^* - \bar{B}^* \otimes \bar{H} \tag{7.27}$$

is the Maxwell stress tensor. Integrating the force density expression over a volume enclosed by a surface S and by use of the divergence theorem we find the force is given by:

$$\bar{F} = -\frac{1}{2}\Re\left(\int_V \{\nabla.\bar{\bar{T}}(\bar{r})\}d^3\bar{r}\right) = -\frac{1}{2}\Re\left(\int_S \{\hat{n}.\bar{\bar{T}}(\bar{r})\}dS\right) \tag{7.28}$$

Each of the terms in equation 7.27 are now computed for reference purposes. Where the stress tensor is dotted with the normal in the x-direction (denoted by the term s_x to avoid confusion with the refractive index term, n) we find:

$$\hat{s_x}.\bar{D} \otimes \bar{E}^* = \epsilon_0 n_0^2 \left(oex.\hat{s_x} + oey.\hat{s_y} + oez.\hat{s_z}\right).oex^* \tag{7.29}$$

where oex, oey and oez represent the electric fields in the x, y and z directions, n_0 is the refractive index outside the surface of interest and $\bar{D} = \epsilon_0\epsilon_r\bar{E}$, with $\epsilon_r = n_0^2$.

$$\hat{s_x}.\bar{B}^* \otimes \bar{H} = \mu_0.ohx^*\left(ohx.\hat{s_x} + ohy.\hat{s_y} + ohz.\hat{s_z}\right) \tag{7.30}$$

where ohx, ohy and ohz represent the magnetic fields in the x, y and z directions and $\bar{B} = \mu_0\bar{H}$.

$$\bar{D}.\bar{E}^* = \epsilon_0 n_0^2\left(oex.oex^* + oey.oey^* + oez.oez^*\right).\hat{s_x} \tag{7.31}$$

$$\bar{B}^*.\bar{H} = \mu_0\left(ohx.ohx^* + ohy.ohy^* + ohz.ohz^*\right).\hat{s_x} \tag{7.32}$$

In the end we have the force given by:

$$\begin{aligned}\bar{F_x} = \Re\int_S dS\frac{1}{4}\{&-(n_0^2\epsilon_0.oey.oey^*.s_x)\\ &+ n_0^2\epsilon_0(oex.s_x + 2.oey.s_y + 2.oez.s_z).oex^*\\ &+ \mu_0(ohx.s_x + 2.ohy.s_y + 2.ohz.s_z).ohx^*\\ &- s_x.(n_0^2\epsilon_0.oez.oez^* + \mu_0.ohy.ohy^* + \mu_0.ohz.ohz^*)\}\end{aligned} \tag{7.33}$$

Similar terms exist for all cartesian directions, however only the $\hat{s_x}$ direction is shown as this sufficiently describes how to complete the computation generally.

7.3.2 Surface force for use in COMSOL

In the surface-force method we follow the principle that the force acts throughout the volume of the medium, but manifests itself via the boundary of the layer, whereby the force is directed towards the lower refractive index material [178]. Following the derivation for the surface force given in [112] but removing the magnetic current terms and assuming

the medium is non-absorbing; from equation 7.25 we get the surface force density term

$$\bar{f}_{surf} = -\frac{\epsilon_0}{4}(\bar{E} \cdot \bar{E}^*)\nabla(\epsilon_r') \tag{7.34}$$

where ϵ_r' is the real component of the local relative permittivity. This yields the form of the surface force in the x-direction, appropriate only for the system of two non-absorbing dielectrics

$$\bar{f}_x = -\frac{1}{4}\Re(\epsilon_0(n_0^2 - n_1^2)[iex \cdot oex^* + iey \cdot oey^* + iez \cdot oez^*]) \cdot \hat{s_x} \tag{7.35}$$

where n_0 and n_1 are the real refractive indices of the dielectric medium outside and inside the particle respectively. iex represents the inside electric field amplitude and oex represents the outside electric field amplitude, and so on for the y and z components. This equation is then used to compute the force by integration of the surface boundaries with respect to area. Note, in the case of both derivations for surface and stress tensor forces, the newer versions of COMSOL do not require any equation input.

7.4 Phototransfection methods

Detailed here are the phototransfection methods used in Chapter 4.

7.4.1 Chinese Hamster Ovary cells

Chinese Hamster Ovary (CHO) cells were cultured in a medium consisting of Minimum Essential Medium (Sigma), 10 % Fetal Calf Serum (Sera Laboratories International) and L-Glutamine, Penicillin and Streptomycin (Sigma). Cells were cultured in plastic flasks and incubated 37 degrees centigrade and with 5 % atmospheric Carbon Dioxide. In order to remove cells from the plastic flask the medium was removed and washed with Trypsin-EDTA (Sigma). 1 ml of Typsin was added and the cells were incubated for 4 minutes. During this time the Trypsin removed adherent cells from the bottom of the flask to allow the cells to float freely in the Trypsin mixture. Any remaining adherent cells were removed by tapping the flask several times. The vibration causes the cells to detach from the flask and float in the Trypsin solution. After 5 minutes 4 ml of medium is added and mixed with the Trypsin. An amount of the resulting mixture was used to create the next passage of cells. Typically 1 ml was used and placed in a clean flask. A further 4 ml was added to the new flask and the solution mixed such that an even coating of cells was ensured.

Glass bottomed petri dishes (World Precision Instruments) were populated with 2 ml of

the cell mixture. The required concentration of cell solution depends upon the confluency and growth rate of the cells in question. Typical amounts used were 50 to 100 /mul of cell solution per 2 ml of medium. 2 ml of diluted cell solution is added to each petri dish. The dishes were then incubated over a period of 24-48 hours.

A (DS-Red) DNA solution was prepared using 300 /mul of OPTIMEM and DNA plasmid solution was added to attain a DNA concentration of 10 /mug per ml. A prepared cell sample was taken and the medium removed. Each sample dish was washed with OPTIMEM twice before the DNA solution described above was gently added. The dish was covered and sealed with UNESCO film to limit loss due to evaporation; the dish was then incubated for 15 mins at 37 degrees centigrade with an atmospheric CO_2 concentration of 5.0 %. The cells were then transferred to the photoporation setup. Following the photoporation procedure the cells were washed twice with the cell culture medium described above and 2 ml of cell culture medium was added to the petri dish. The cells were then incubated as described above for 48 hours. In some experiments 15 μl of Nupherin (Enzo Life Sciences) was added to the DNA plasmid solution to potentially enhance transfection efficiency [179].

The cells which were transfected with DS-Red were identified using a fluorescence microscope (Nikon Eclipse Ti) utilising a Nikon TRITC filter cube, with a Nikon Plan Fluor 20x/0.50NA phase contrast objective for imaging. Fluorescent cells within the marked region of interest were counted. The number of fluorescent cells divided by the number of cells photoporated gives the uncorrected transfection efficiency.

7.4.2 Human Embryonic Kidney cells

Human Embryonic Kidney (HEK) cells were cultured and photoporated in the same manner as CHO cells apart from requiring a different procedure to maintain cell attachment to the surface substrate of the petri dishes. Glass bottomed petri dishes (World Precision Instruments) were prepared with a Laminin-OPTIMEM (Sigma) mixture with surface area concentration 5 μg/cm^2 and incubated at 37 degrees centigrade with an atmospheric CO_2 concentration of 5.0 % for 24 hours. The Laminin-OPTIMEM solution was removed and the dish washed with medium two times. Following this procedure cells were introduced in a manner identical to above. Further, transfection experiments were carried out in the same manner also.

7.5 Use of MATLAB and other programs for producing theoretical/computational images

The author independently wrote the MATLAB programs used to generate the theoretical images in all chapters except for in the optical binding chapter. Also provided is the MATHEMATICA program written by Michael Mazilu for calculating the optical binding forces between Rayleigh-sized particles, as used in the optical binding chapter. These are provided with the supplementary CD accompanying this thesis or can be emailed on request. Please contact Kishan Dholakia for the author's most up-to-date email address, if required.

Acknowledgements

I am exceptionally grateful to my supervisor, Prof. Kishan Dholakia for his guidance, understanding, and hard work throughout the course of my PhD. I am particularly appreciative to him for providing me with the opportunity to work in the Optical Manipulation Group with cutting-edge laser technology. I am very grateful to Prof. Frank Gunn-Moore for his guidance and encouragement in aspects relating to all aspects of science. I would also like to thank my mentors, Dr. Tom Brown and Prof. Wilson Sibbett for their unabated encouragement and enthusiasm for my work.

I am completely indebted to Dr. Michael Mazilu for the many hours he has spent talking to me about science, correcting my scientific understanding and the many models provided by him throughout my PhD, often at particularly short notice. I am also indebted to Dr. Maciej Antkowiak for the multitude of discussions about the light-biomatter interaction which took up so much of our time. I am further indebted to Dr. Joerg Baumgartl for all of his support in the lab, and most importantly, introducing me to coffee breaks, without which, my world would have been further darkened by the windowless depths of the optics laboratories!

To Christine Crombie, Darran Milne, Claire Mitchell, Niall Quinn, Christian Reimer, Helen Rendall, Sebastian Schulz and Richard Tatham, I thank you all for your friendship throughout the PhD and for making coffee break, lunchtimes, and sometimes evening-times all the more memorable and entertaining(!)

To Lani Torres-Mapa I thank you for the many wonderful conversations about literally anything. To Martin Ploschner, for the multitude of self-deprecating conversations regarding philosophy of science and life in addition to many discussions about theoretical and experimental aspects of science. I am certainly better informed as a result of these discussions! To, in no particular order, Tom Cižmár, Tom Vettenburg, David Stevenson, Heather Dalgarno, Yoshi Arita, Svetlana Zolotovskaya, Sebastian Kosmeier, Praveen Ashok, Bavishna Balagopal, Areti Mourka, Maria Dienerowitz, Dave Walsh, Klaus Metzger, Fiona Baumgartl, Alexander Lagatsky, Matthieu Robert de Saint Vincent, Jill Morris, Xanthi Tsampoula, Rob Marchington, Andrew McKinley and Craig McDougall, to name but a few. I thank you all for the scientific support and most excellent discussions we have had over the years.

To Dr. David Stothard I thank you for many hours of discussion about life and science and for taking the time to create stunning photographs of my wedding to Mrs. Rachel Rudhall.

I am also very grateful to all of my family down South for their kind understanding,

support in everything that I do and for teaching me to read, write, do maths and make music at the earliest stages of my life, all of which provided me with the foundation necessary for me to pursue my academic journey and enjoy life.

I reserve the most personal gratitude to my wonderful wife, Rachel Rudhall, without whom, I could not sustain myself in life. You have had to put up with evenings, weekends and holidays without me and I cannot thank you enough for your unending support. I also cannot thank you enough for bringing our wonderful daughter, Alice Eveleigh Rudhall into the world. She never ceases to brighten up my day with her brilliant smiles and giggles.

Finally, on a less emotional note, I finish with my favourite proverb: *If you drink, you die. If you don't drink, you die. So you may as well drink.*